Low Dimensional Polaritons: Waveguides, Zitterbewegung and Non-Linear Compact Localised States

Mr Seth Lovett

A thesis presented for the degree of
Doctor of Philosophy

Department of Physics and Astronomy
The University of Sheffield
United Kingdom
February, 2023

Abstract

Exciton-polaritons in GaAs based microcavities and waveguides are used to study different phenomena ranging from spin-orbit coupling effects to magnetic field response. Most of the work concerns polaritons in periodic potentials with the remainder using planar microcavity polaritons.

In Chapter 3 work involving the study of polaritons in GaAs based slab waveguides with a photonic crystal etched into the top surface is presented. The tuneability of a band gap in the polariton dispersion with and without an applied magnetic field is demonstrated.

In Chapter 4 the first direct observations of Zitterbewegung for highly photonic exciton-polaritons in planar and honeycomb lattice microcavities are presented. This work also demonstrates the dependency of the Zitterbewegung period and amplitude on the energy splitting between two orthogonally polarised modes in the dispersion.

In Chapter 5 the work presented concerns the direct excitation of compact localised states in a 2D Lieb lattice microcavity in both the linear and non-linear regimes. A linear and non-linear localised state is created for the lowest energy flat band. A non-linear response is observed in a single micropillar for the second lowest energy flat band.

List of Publications

“**Exciton–polaritons in GaAs-based slab waveguide photonic crystals**”, C. E. Whittaker, T. Isoniemi, S. Lovett, P. M. Walker, S. Kolodny, V. Kozin, I. V. Iorsh, I. Farrer, D. A. Ritchie, M. S. Skolnick and D. N. Krizhanovskii. Appl. Phys. Lett. 119, 181101 (2021) DOI: https://doi.org/10.1063/5.0071248

“**Observation of Zitterbewegung in photonic microcavities**”, S. Lovett, P. M. Walker, A. Osipov, A. Yulin, P. U. Naik, C. E. Whittaker, I. A. Shelykh, M. S. Skolnick, D. N. Krizhanovskii. (Submitted and currently under review at Light: Science and Applications.) (As of March 2023)

Presentations

“**Observation of Photonic Zitterbewegung Effect in a Hexagonal Lattice Microcavity.**”, EP2DS-24/MSS-20: 24th International Conference on Electronic Properties of Two-Dimensional Systems/ 20th International Conference on Modulated Semiconductor Structures ; Toyama, Japan; 31st October-5th November 2021. (Presented online)

“**Observation of Photonic Zitterbewegung Effect in a Hexagonal Lattice Microcavity.**”, ICPS 2022: International Conference on the Physics of Semiconductors 2022, Sydney, Australia; 27th-30th June 2022. (Presented in-person)

Acknowledgements

I would like to acknowledge what a great privilege it has been to study my PhD in the Low Dimensional Structures and Devices group at the University of Sheffield. I would like to express deep gratitude to my supervisor Prof. Dmitry Krizhanovskii who has supported and guided me throughout the past three and half years. I would like to extend this gratitude to Prof. Maurice Skolnick for overseeing such a fruitful research group and allowing me to be part of it all. I would also like to thank Dr. Paul Walker whose extensive knowledge and skill both inside and outside the lab has taught me so much and whom it has been an absolute pleasure to collaborate with. Thank you Dr Charles Whittaker who helped guide me early in my PhD and built the foundations for some of the work in this thesis and also Dr Tommi Isoniemi for providing most of the samples. I would like to thank everyone who has been part of the polariton group during the course of my PhD who have supported me in their own ways no matter how small and all of the staff at the University of Sheffield who keep the labs and building running behind the scenes.

I would like to acknowledge all my grandparents for imparting their wisdom and knowledge onto me and particularly my grandfather Michael Canham who has always inspired me to pursue all things scientific. Thank you to my Mum and Dad whose support, motivation and belief in me is a large reason I am able to present this thesis today. Thank you also to both of my brothers and the rest of my family for all of your support.

Finally, I would like to thank Ellie, as without your patience, wisdom and unconditional support this thesis would not be possible.

Contents

Chapter 1

Background

1.1 Introduction

The study of polaritons confined to low dimensional systems is an area of research with a long and bountiful history filled with profound breakthroughs in our understanding of novel quantum phenomena. Created via the strong coupling between light and quantum well excitons, these composite boson quasiparticles have also had a wide reaching influence across physics allowing analogous studies of areas such many-body physics[1–4], high energy systems [5, 6] and even cosmology [7, 8]. The relative ease of which polaritons grant researchers access to the optical information they possess has allowed us to directly peer into the fascinating worlds of phenomena such as Bose-Einstein condensates [9, 10], topologically protected states and superfluidity. Yet still, over two decades since the first experimental reports of their existence, low-dimensional polaritons continue to be the gift that keeps on giving, in part facilitated by the recent advancements in semiconductor device fabrication. With modern post-growth etching techniques, the tailoring of the polariton potential landscape is paving the way for the quantum simulation of complex solid-state systems along with advancing the steady progress toward achieving integrated polariton optoelectronic devices. This thesis explores several different phenomena surrounding polaritons confined to low dimensional structures, firstly in 2D slab waveguides and later in planar and lattice microcavities with the aim of further expanding the collective knowledge around these fascinating hybrid quasiparticles. The overarching goal of this thesis is to highlight just some of the various areas of physics for which polaritons continue to offer a boon of exciting experimental results on the forefront of our understanding of low dimensional physics.

1.2 Semiconductor materials

1.2.1 Semiconductor band structure

Semiconducting materials fill a unique niche in solid state physics as materials that are somewhere between conductor and insulator and most importantly, materials that have provided a wealth of research and breakthroughs. In this thesis, the devices used for the presented work utilise gallium arsenide (GaAs), as well as other compound semiconductors, such as aluminium gallium arsenide (AlGaAs) and indium gallium arsenide (InGaAs), as a platform for polariton research. The unit cell of GaAs is a zince-blende structure and, when considering its valence and conduction bands in momentum space, has a direct band gap of 1.42eV [11]. The relatively small and direct nature of this band gap along with a long history of well established research and device fabrication, makes it an extremely suitable platform for optical-condensed matter research. GaAs also holds the unique title of the platform for which the first observation of exciton-polaritons (referred from here onwards simply as polaritons) were made [12, 13]. Other similar zince-blende semiconducting materials are also suitable for polariton research such as cadmium telluride (CdTe)[14] which provided the first demonstrations of polariton condensation [9, 10]. Wide band gap semiconductors are also a popular option when studying polaritons in part due to their strong exciton binding energy allowing room temperature experiments, an example of this is gallium nitride (GaN)[15, 16]. The typical description of a semiconducting material is one of separate energy bands. More specifically, a valence and conduction bands separated by an energy gap, E_g, with the population of electrons occupying the former band when no external energy excitation is present.

This band gap, or forbidden region, is a consequence of the quantization of energy and explains why, without sufficient excitation, electrons cannot occupy the conduction band. In the case of electron occupation of the conduction band, whether due to a non-separation of valence and conduction bands or simply due

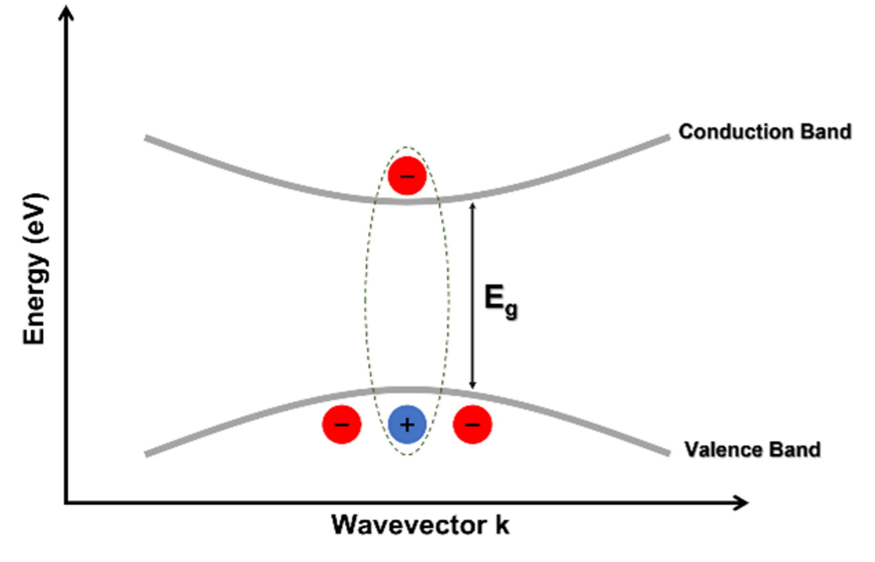

Figure 1.1: Simplified diagram showing the energy gapped valence and construction band in a typical direct-band gap semiconductor. The red particles represent electrons. The dotted oval represents the two-particle exciton system consisting of a positive hole and an excited electron.

to a lack of valence band completely, the material would be described as a conductor. Alternatively, in insulators it is extremely hard for an electron to be excited across this band gap due to it large size (5-10meV). Technically speaking, electrons could be excited into the conduction band using high energy photons such as those in the UV region of the electromagnetic spectrum. In the case of gapped semiconductors, whilst there is still separation of the valence and conduction band, if sufficient external energy input is present, an electron can be excited across the band gap to occupy the conduction band, providing this input energy is equal to or greater than E_g. The excitation of a valence electron (which absorbs light more efficiently than it emits it) leads to a net negative charge of the conduction band which conversely leaves a net positive charge within the valence band. This localised positive charge is what remains of the state once occupied by the excited electron and is commonly referred to as a “hole”.

1.2.2 Excitons

Even though the newly excited electron and hole are separated by an energy gap, they are still able to interact and form a bound state. When the coulomb interaction between the two oppositely charge particles is sufficiently large to overcome external forces (e.g. coulomb screening), the result is a neutral quasiparticle known as an exciton with an energy less than that of its unbound electron-hole constituents by the binding energy, E_B. The first confirmed observations these particles were of excitonic features in the spectrum of Cu2O reported in the 1950s[17, 18]. These excitons can be defined in two separate cases, depending on whether the Bohr radius is larger or smaller than the lattice constant of the material of which they occupy. If the Bohr radius is smaller than the lattice constant they are known as Frenkel excitons [19, 20], these are typically found in organic materials such as tetracene and have a binding energy of 0.1-1eV. If the Bohr radius is larger than the lattice constant, they are known as Wannier-Mott excitons. The larger Bohr radius in the latter case can be put down to the large screening of the coulomb interaction due to the lattice polarisation of the dielectric materials in which they are found[21] (i.e. semiconductors), this leads to a much larger binding energy of 10-30meV.

As shown in Figure 1.2 the type of excitons present in a system depends on the material in which they form and, since the work presented in this thesis utilises GaAs based systems, Frenkel Excitons will be of no concern going forward. For the sake of brevity, Wannier-Mott excitons will be referred to simply as excitons. Due to the attractive coulomb force between the hole and electron in an exciton, its Schrödinger equation is analogous to that of a hydrogen atom and takes the form of the Wannier equation in materials such as GaAs. Starting with the Wannier equation, the binding energy of excitons in GaAs,E_λ can be found using

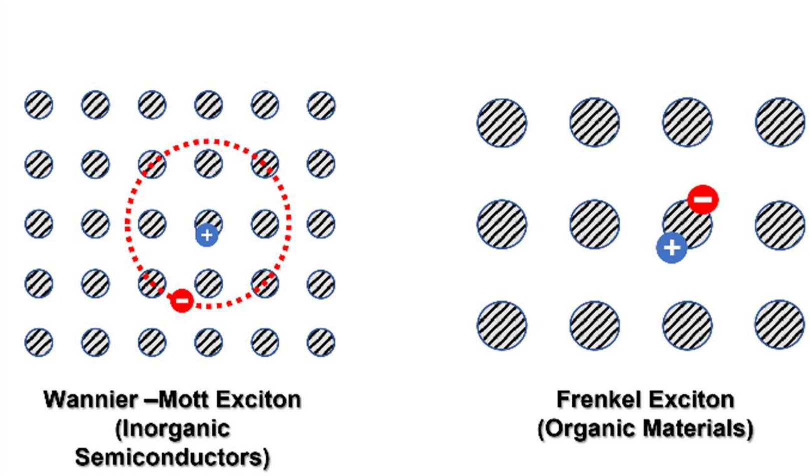

Figure 1.2: Simplified diagram showing two different types of excitons defined by their Bohr radius.

$$-\left[\frac{\hbar^2\nabla^2}{2\mu}+V(r)\right]\phi_\lambda(r)=E_\lambda\phi_\lambda(r), \tag{1.1}$$

where μ is the reduced mass of the bound electron and hole given by $\mu = m_e m_h/(m_e+m_h)$ with masses m_e and m_h respectively and separation r. Here the potential, $V(r)$, is

$$V(r)=\frac{e^2}{4\pi\epsilon_r\epsilon_0 r}. \tag{1.2}$$

From this, the 1s exciton wavefunction is given as

$$\Psi_{1s}(r)=\frac{e^{\frac{-r}{a_B}}}{\sqrt{\pi a_B^3}}, \tag{1.3}$$

where a_B is the Bohr radius given by $a_B = 4\pi\hbar^2\epsilon\epsilon_0/\mu e^2$. Finally, from this the binding energy can be defined as

$$E_B=\frac{\hbar^2}{2\mu a_B^2}. \tag{1.4}$$

When considering the low binding energy of excitons in GaAs, a fundamental and significant property becomes obvious, namely their complete instability at room temperature. To ensure stability of GaAs excitons, the environmental thermal energy, $k_b T$, must not exceed the binding energy as described in equation 1.4. This condition can be achieved by using cryogenic temperatures for any experiments concerning GaAs excitons. It is worth noting that exciton formation has been observed in other semiconductors at temperatures above cryogenic, and in some cases room temperature[15], in the latter case this was first achieved by specifically tailoring quantum well confinements to reduce exciton-phonon interactions [22]. It has also been shown that it is in fact possible to achieve strong coupling of excitons and photons in GaAs based devices by increasing the number of quantum wells [23].

1.3 Exciton confinement and polariton formation

1.3.1 Optical microcavities for the study of low dimensional polaritons

Before addressing strong light matter coupling, a platform for such hybridisation is first needed, with optical microcavities being the most obvious ideal choice. The huge volume of valuable polariton research that relies on optical microcavities as a platform is a testament to this fact. Microcavities were first born from the development of semiconducting laser diodes in 1962 [24, 25] and from there, the technology has been developed and utilised for a wide range laser based devices [26–28].

The work presented in this thesis concerns a specific type of microcavity, known as a Fabry–Pérot interferometer, also sometimes referred to as a microresonator. This device uses two highly reflective surfaces placed at a fixed distance from each other, this distance is known as the cavity length, L_c. Between the two mirrors a defect layer is placed to act as the cavity. Typically, during the growth phase, a gradient in the thickness of the cavity is created to allow variations in detuning (see section 1.3.3), this is often done using a rotation-stop.

The composition of the mirrors is fundamental to the working of the microcavity and a commonly used practice (also the one used for the samples concerned in this thesis) is to stack alternating layers of semiconducting materials with differing refractive indices to form a distributed Bragg reflector (DBR). As mentioned, the name interferometer is assigned to the device as the high levels of reflectivity for light incident on a DBR is due to the constructive interference that takes place at varying penetration depths for incident waves. Optimising the reflectivity via constructive interference of the DBR for a certain wavelength, λ_0, can be achieved by considering the Bragg condition, where optimal thickness is given by

$$T_{1(2)} = \frac{\lambda_0}{4n_{1(2)}}, \tag{1.5}$$

where $n_{1(2)}$ is the refractive index of whichever of the two materials is being considered. This condition creates a range of wavelengths in which near unity of reflection can be achieved, this range is known as the stop band and is centred around λ_0. The spectral width of the stopband is determined by the contrast in the refractive indices of the DBR layers and for wavelengths outside of this region, photonic modes will simply permeate the DBR stack and escape the cavity. To increase reflectivity in the stop band, the number of DBR stacks can also be increased, until, after optimisation of all three parameters, the cavity can achieve near total reflective confinement of a range of allowed photonic modes coupled into the cavity. Typical polariton microcavities contain 15-20 pairs of DBR layers in the top and bottom stacks and, as in this thesis, are made of alternating layers of GaAs and AlGaAs on a GaAs substrate[29].

With modern growth methods such as molecular beam epitaxy (MBE), highly optimised cavities can produced with high levels of reflectivity controls and relative ease of reproducibility[30]. The quality of these cavities can be determined by considering the Q factor associated with them. To determine the Q factor, the photonic dispersion within the cavity must first be considered

$$E_C(k_{||} \approx E_C(k_{||} = 0) + \frac{\hbar^2 k_{||}^2}{2m_c}, \tag{1.6}$$

where $k_{||}$ is the in-plane wave vector given by $k_{||} = \sqrt{k_x^2 + k_y^2}$ and m_c is the effective mass given by $m_c = hn_c/cL_c$. Using the above, and the linewidth of the cavity mode, γ_c, the Q factor is defined as

$$Q = \frac{E_c}{\gamma_c}. \tag{1.7}$$

It is worth noting that γ_c is determined by the full-width-half-maximum (FWHM) of the resonant energy of the cavity mode. For large values of Q (typical values associated with Fabry–Pérot microcavities are sufficiently large), this Q factor is equivalent to the ratio of energy stored to energy lost thus γ_c is sometimes referred to as the cavity loss rate. The samples in this thesis have high Q factors in the region of 15000 but recent experiments have shown DBR based microcavities with Q factors in excess of 250,000 [31] and when moving away from DBR based microcavities, Q factors can be in the region of 10^7, for example with silicon based toroid microcavities [32].

1.3.2 Quantum wells

First proposed in 1963[33, 34], a typical semiconductor quantum well (QW) acts to confine electrons and holes (and consequentially excitons) within a low dimensional region enclosed by potential barriers. This results in the quantisation of at least one dimension of motion for the confined particles and for a typical semiconductor heterostructure this will be the growth direction. Simply put, the confined particles are free to move in 2 directions (xy-plane for example) but confined in the z-direction thus in this case the particles are under 1-dimensional confinement. Note, the confinement of particles such as electrons or holes relies on the width of the quantum well being on the scale of the de Broglie wavelength of the confined particle.

A quantum well can be created by enclosing a thin semiconductor layer with a different semiconductor with a larger band gap. The lower band gap of the sandwiched layer leads to different, lower energy eigenstates compared to the

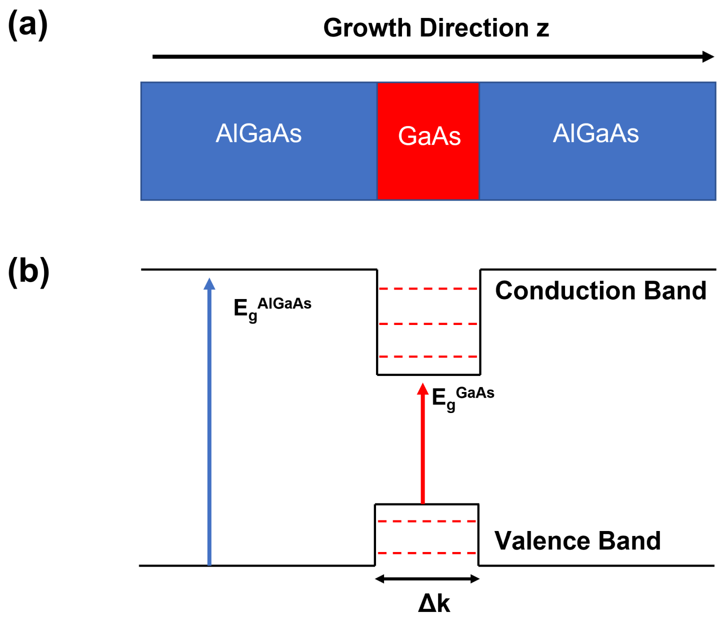

Figure 1.3: (a) Typical GaAs quantum well placed between AlGaAs layers (b) Band diagram showing how the decreased band gap of the quantum well in (a) acts as a potential barrier for confined particles. The red dashed line represent the discrete states within the well.

surrounding material and a thus a potential barrier is formed between the states of each materials. These newly formed eigenstates are discrete quantised energy levels, analogous to the energy levels of an atom. A commonly used quantum well consists of a GaAs layer sandwiched by AlGaAs on either side in the growth direction[35]. However, in this thesis, the quantum wells are made of InGaAs surrounded by a GaAs cavity and GaAS/AlGaAs DBR's. This is popular choice for the structure of polariton microcavities as afford narrow linewidth polariton states, relatively low disorder and the fabrication processes are well established [29].

1.3.3 Light matter coupling

By combining knowledge of excitons, microcavities and quantum wells, light matter hybridisation in the context of exciton-polaritons can now be understood. By introducing valence electrons confined to QWs to the defect layer of a Fabry–Pérot microcavity, all the ingredients are in place to allow the creating of microcavity-polaritons.

The basic principle begins with the coupling of a photonic mode into the microcavity, this mode is repeatedly reflected from the top and bottom DBR stacks. Upon encountering a confined valence electron in the QW, the photonic mode is absorbed and exciton formation occurs. Recombination then quickly follows thus allowing the photonic mode to continue its propagation until it is reflected back and encounters the electron again. The rapid repetition of this process constitutes the formation of a quasiparticle in the microcavity i.e. a polariton. The polariton shares the properties of both its constituents such as low effective mass ($10^{-4}m_0$) due to the photonic component and inter-particle interactions due to the excitonic component[36].

The process of observing polaritons and analysing their properties in microcav-

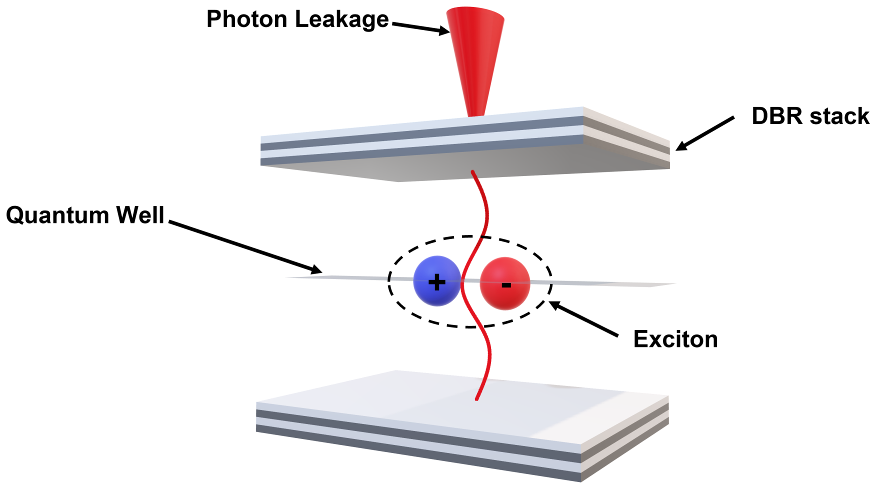

Figure 1.4: Simplified labelled schematic showing the light matter coupling in a microcavity with embedded quantum wells.

ities is possible due to the photon emission that occurs via tunnelling through the DBR stacks. This form of emission allows direct observation of the internal polariton wavefunction inside the microcavity. Such observations are possible as the emitted photons carry all the spatial, in-plane momentum and frequency information of the polariton states they occupied within the microcavity and is a consequence of conservation laws mediating exciton emission. This process of information retention by photons via exciton emission is known as photoluminescence (PL) and underpins the vast majority of polariton studies in microcavities. Collection of these emitted photons via optical spectroscopy and charge coupled device (CCD) imaging allows the creation of dispersion relations otherwise known as E-k relations.

The key signature of polariton formation in a microcavity is the two branch dispersion that is observed with analysing the momentum-energy dependency of emitted photons. The photonic mode alone has a parabolic dispersion typical of photons, whilst the exciton resonance, E_x, due to its large effective mass, is essentially flat. For the formation of a polaritons, two conditions must be met; the exciton oscillator strength must be sufficiently large and the Q factor of the cavity must also be sufficiently large. With both of these met, normal mode splitting between the exciton and the cavity photon can occur as the rate of energy transfer between exciton and cavity photon exceeds dissipation rate from the cavity. This will lead to an energy transfer at a rate known as the Rabi frequency (Ω), and the formation two new eigenstates of the system; the upper polariton branch (UPB) and lower polariton branch (LPB). For the case of strong coupling in a microcavity, the Rabi frequency can be described in terms of energy splitting between the lowest energies of the LPB and UPB using the vacuum Rabi splitting ,$\hbar\Omega$. This is assumes the QW is placed at the anti-node of the cavity electric field and that $E_c = E_x$. $\hbar\Omega$ is defined as

$$\hbar\Omega = \sqrt{\frac{N_{QW}(\hbar e)^2}{2\epsilon m_0 L_{eff}} f_{osc}}, \tag{1.8}$$

where N_{QW} is the number of QWs, L_{eff} is the effective length of the cavity (when mode penetration of cavity mirrors is considered) and f_{osc} is the exciton oscillator strength.

The energies of the UPB and LPB vary depending on values intrinsic to the microcavity, such as cavity-exciton detuning and exciton linewidth. These energies can be described with the following equation

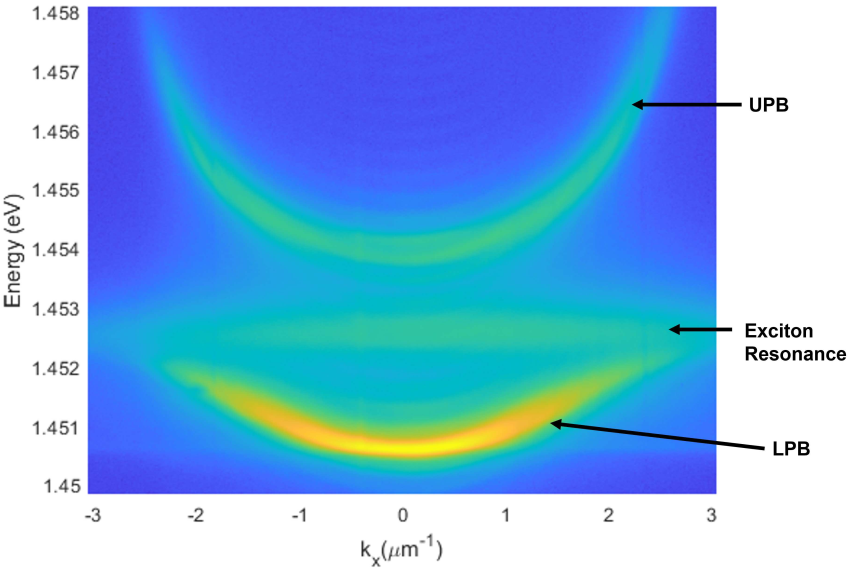

Figure 1.5: Far-field emission showing a typical polariton dispersion due to strong coupling. In this case detuning is approximately -2meV.

$$E_{UPB,LPB}(k_{||}) = \frac{1}{2}[E_x + E_c - i(\gamma_x + \gamma_c)] \pm \frac{1}{2}\sqrt{(\hbar\Omega)^2 + [\Delta - i(\gamma_c - \gamma_x)]^2}, \quad (1.9)$$

where γ_x is the exciton linewidth and Δ is the cavity-exciton detuning, $\Delta = E_c - E_x$. For the system to be in the strong coupling regime the condition, $\hbar\Omega > \gamma_c - \gamma_x$, must hold true. A key indicator that the cavity mode is strongly coupled to the exciton is the existence of anti-crossing between the UPB and LPB. This size of the anti-crossing varies with detuning but at the minimum, where $k_{||} = 0$, the splitting has a value of $\hbar\Omega$.

Due to the hybrid nature of polaritons, allowed states will vary in their excitonic or photonic content, with some polariton states being highly photonic or highly excitonic. When considering the dispersion, states that exist close to the exciton resonance are higher in exciton content, which increases the closer to resonance they are. For the LPB this means that for high values of $k_{||}$, polaritons are highly excitonic and for low $k_{||}$, polaritons are highly photonic. The opposite is the case for the UPB, meaning that exciton-photon coupling is most effective at small $k_{||}$ values. The content of polaritons states for the UPB and LPB can be quantified by using the Hopfield coefficients[37]. The Hopfield coefficients can be used to describe the respective exciton-photon fractions of UPB or LPB polaritons states as follows

$$X_{k_{||}}^2 = \frac{\delta_{k_{||}} + \sqrt{\delta_{k_{||}}^2 + (\hbar\Omega)^2}}{2\sqrt{\delta_{k_{||}}^2 + (\hbar\Omega)^2}}, \tag{1.10}$$

$$C_{k_{||}}^2 = -\frac{\delta_{k_{||}} - \sqrt{\delta_{k_{||}}^2 + (\hbar\Omega)^2}}{2\sqrt{\delta_{k_{||}}^2 + (\hbar\Omega)^2}}, \tag{1.11}$$

with the condition that $X_{k_{||}}^2 + C_{k_{||}}^2 = 1$. As can be seen in Eqns.(1.10-11) the fraction of exciton or photon content of polariton states also varies with the detuning, such that for one given detuning, the Hopfield coefficients of a polariton state at $k_{||} = 0$ will differ from that at a larger or smaller detuning. Figure 1.6 shows how the Hopfield coefficients, and thus the exciton-photon fraction, changes with $k_{||}$ at different detuning for polariton states in the LPB.

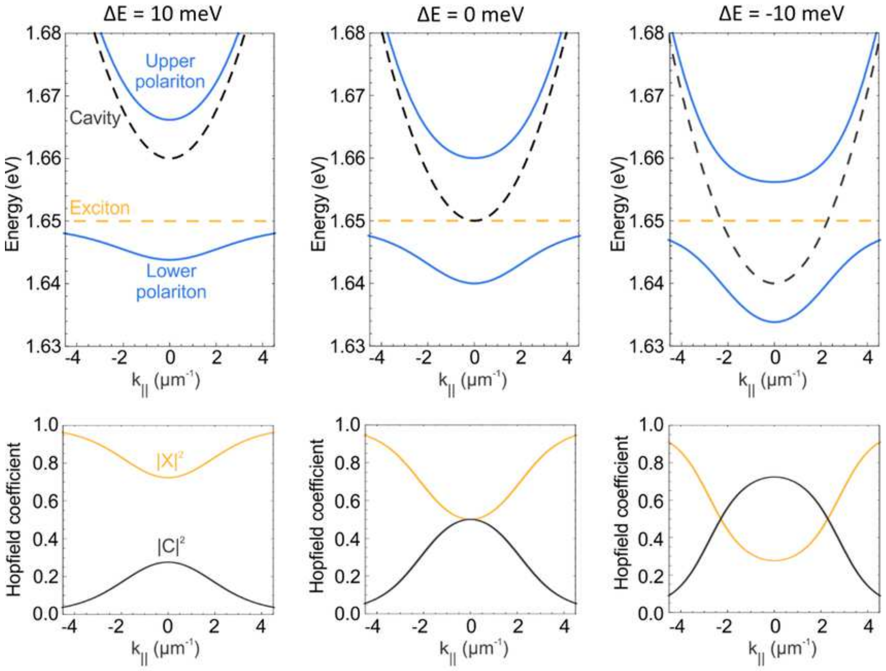

Figure 1.6: Top panels: Polariton dispersions for different detunings. Bottom panels: Hopfield coefficients as a function of $k_{||}$ corresponding to the panel directly above. Image taken from [38].

1.4 Polariton non-linearity

1.4.1 Inter-particle interactions and parametric scattering

The inter-particle (or polariton-polariton) interaction arises from the excitonic component of polaritons and is the source of many of the non-linear effects observed in polariton systems. For microcavity polaritons, these self-interactions originate from two main sources. The first is the spin dependant Coulomb interaction between the electrons and the holes of two interacting excitons, more commonly known as the exchange interaction. The second being the Pauli blockade mechanism, a direct manifestation of the exclusion principle, preventing the double occupancy of excitons and in turn reducing the exciton oscillator strength.

Both of these mechanisms act to renormalize the polariton states, something manifested as a blueshift in the polariton dispersion. Previous work has demonstrated the spin dependency of these polariton-polariton interactions such that, for polaritons with matching spins, a repulsive force acts whereas, for polaritons with differing spins, the interactions results in an attractive force[39]. More specifically, polaritons with opposite circular polarisations will weakly attract with strength, g, whilst polaritons with linear polarisation will weakly repel[40, 41]. Various experimental measurements for the polariton-polariton interaction strength have been reported with the majority shown in Figure 1.7. There is a lack of agreement on the exact values with ranges from the order of 10^0 to the order of 10^2. The outlier reported by Sun et al. [42] and shown in Figure 1.7 is now generally believed to be highly overestimated due to the continuous-wave nature of the experiments. To increase the level of self-interaction, the polariton density can be increased, often by increasing resonant laser power, this in turn will increase

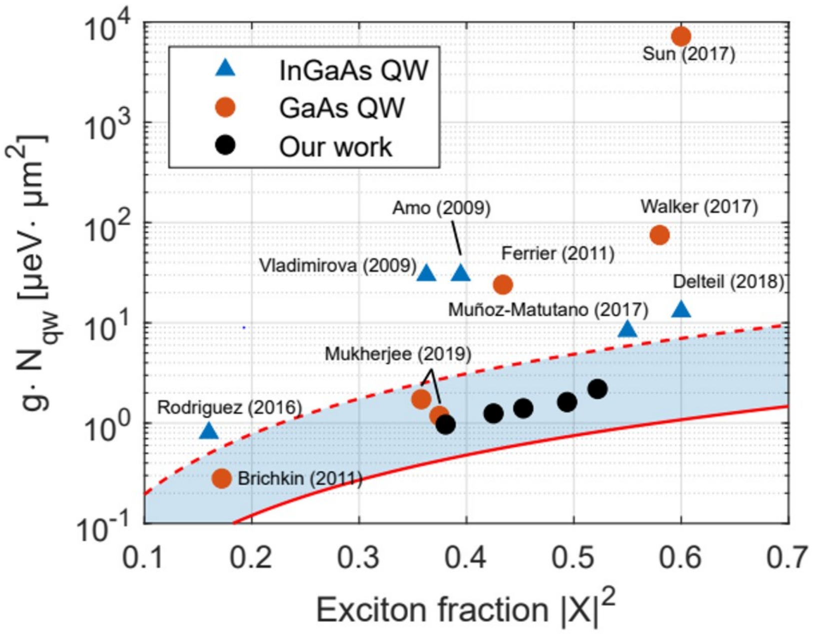

Figure 1.7: Different values of the polariton-polariton interaction strength reported in multiple publications including the results reported by [42]. Image taken from[43].

the number of scattering events and the overall blueshift. At low density the blueshift of polariton states is linearly dependant on the polariton density thus interaction strength can be calculated using[42]

$$\Delta E = gn, \tag{1.12}$$

where ΔE is the blue shift, n is the polariton density and g is the co-circularised polariton-polariton interaction strength. The level of interaction can often be observed indirectly by measuring the signal emission from the states the polaritons are scattered into and it is here that the non-linearity in emission is often observed when the polariton density of the original states crosses a threshold. Under resonant excitation these interactions can be observed in the blueshift of the dispersion towards to the laser excitation energy. A prime example of this blue shift is observed in experiments concerning the parametric scattering of polaritons. This parametric scattering is an angle dependant momentum exchange scattering process which leads to the formation of a higher momentum idler state and a lower momentum signal state in the following exchange

$$2k_{pump} = k_{idler} + k_{signal}. \tag{1.13}$$

A pump laser directly injects photons into the polariton dispersion at a specific angle and energy to increase inter-particle interactions. A non-linear increase in emission is observed in the $k_{||} = 0$ states over some threshold power, with the system said to be above threshold when emission increases linearly again. Over this threshold , the LPB will blueshift as the polariton states renormalize due to self interaction. The coupling between the signal, idler and pump states can be described as an optical parametric oscillator. The first reports of optical parametric oscillation of polariton states arose over 20 years ago by Stevenson et al.[44] and A. I. Tartakovskii et al. [45], and later the properties of the newly formed blue shifted condensate at $k_{||}$ were explored by D.N. Krizhanovskii et al.[46].

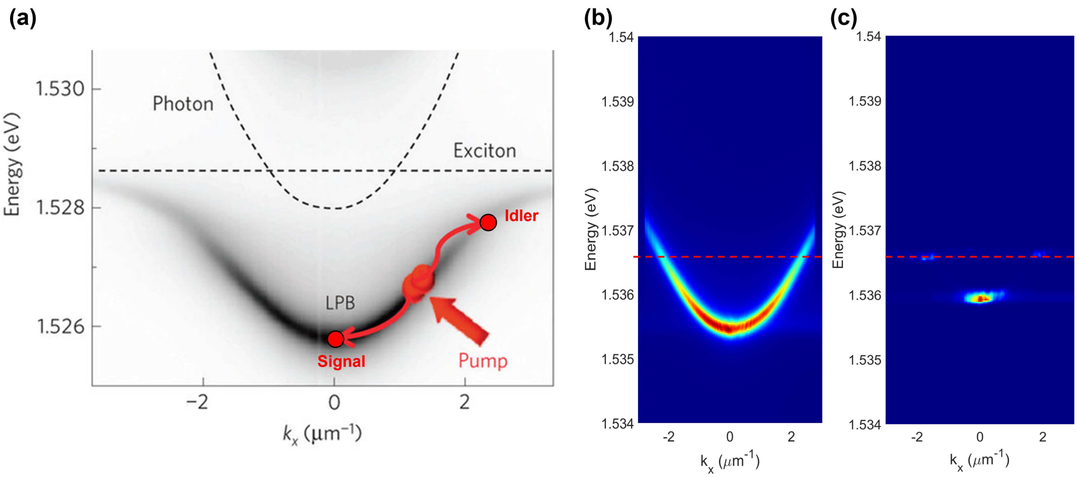

Figure 1.8: (a) Typical process of parametric scattering with the momentum exchange taking place at the pump spot and polaritons scattering into the idler and signal states. Taken from[47]. (b) Experimentally obtained LPB dispersion at low power (density) with the laser energy indicated with the red dashed line. (c) The same dispersion as in (b) but now with increased power (density) above threshold showing significantly increased blueshifted emission from the signal states at $k_x = 0$.

1.4.2 Polariton condensation

The bosonic nature of polaritons means they are expected to undergo a phase transition similar to that of Bose-Einstein Condensates (BEC'S)[10, 48]. This phase transition leads to macroscopic occupation of the ground state in the polariton dispersion with strong non-linear increases in signal from the $k = 0$ state. The nature of polariton condensates in microcavities is inherently one of non-equilibrium owing to the fact microcavities are driven-dissipative systems. Photon leakage via tunnelling through the Bragg mirrors acts to limit polariton lifetimes and because of this, the high energy exciton reservoir must be constantly replenished by a pumping source. Two classifications of polariton condensations can arise depending on how near the system is to equilibrium, the first being Kinetic condensation, where insufficient polariton lifetime prevents thermalization[49]. In this case the condensate will occupy the state that optimally balances polariton lifetime with the replenishment of relaxed excitons. The second case is known as thermodynamic condensation and occurs when polariton lifetime allows thermalization, thus polaritons may occupy the minimised energy state of the system [49]. In the case of thermodynamic condensation, the polariton condensate will display many of the experimental characteristics synonymous with BEC's such as long-range spatial coherence and increase in the temporal coherence of the emission[10, 46].

The threshold for the phase transition is indicated by a sharp non-linear increase in emission intensity with a continued coherent beam of light being emitted past the threshold. A microcavity polariton system in this state is commonly referred to as a "polariton laser"[48]. Unlike conventional lasing, this process of optical gain requires no population inversion. Experimental observations of polariton condensation and lasing has been made in GaAs[51, 52] and CdTe[49] based systems at cryogenic temperatures and room temperature lasing has even been observed using a GaN based system[15, 16].

Since the conception and first observations of polariton condensates, research in the field has led to consideration of condensates within a wide array of materials. For example, condensation was achieved using microcavities with embedded transition-metal dichalcogenide (TMDC) monolayers via the hybridisation of GaAs QWs with $MoSe_2$ monolayers[53]. Condensation at cryogenic temperatures has also been confirmed in bare $MoSe_2$ monolayers[54]. The concepts of topological photonics has also been applied to polariton condensates with polariton laser being observed from topologically protected edge modes giving rise to the idea of topological polariton lasing[55].

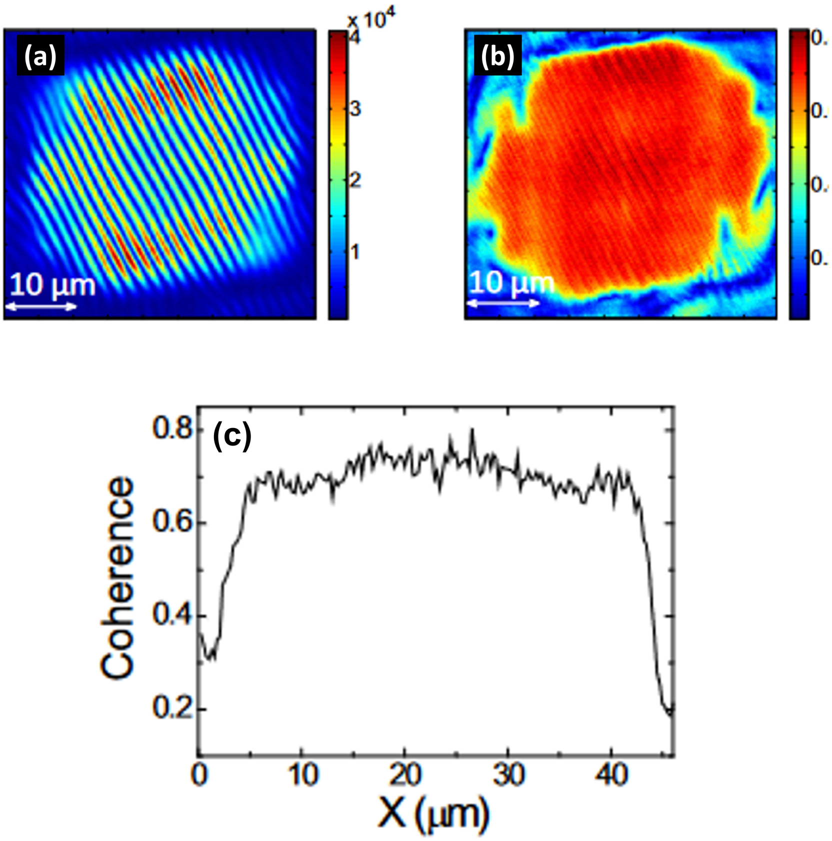

Figure 1.9: (a) Interferogram of a polariton condensate created by OPO at the parametric threshold in real space showing a clearly defined interference patten. (b) Resulting coherence map for the condensate shown in (a) showing the spontaneous long range spatial coherence indicative of polariton condensates. (c) Horizontal profile of the coherence map shown in (b) showing constant coherence across the condensate region. All images taken from [50].

1.4.3 Superfluidity

An effect closely linked to polariton condensation is that of superfluidity. First discovered in LHe experiments[56, 57], a superfluid behave wholly differently to typical fluids owing to its zero viscosity giving the superfluid an irrotational nature. The link between superfluidity and atomic BEC's was suggested very soon after the discovery of superfluidity itself[58, 59] however it wasn't experimentally confirmed in polariton condensates until much later[60] and even more recently at room temperature[61].

Perhaps the most intriguing property of a superfluid, arising from its ability to flow without friction, is the quantisation of angular momentum throughout it. More specifically, when the superfluid is given some non-zero orbital angular momentum, rather than rotate as a whole body, small pockets of fluid will rotate around a hole in the superfluid in the form of vortices. These vortices are of great interest in the field of polariton physics and were first observed in the form of forked dislocations in interferograms of polariton condensates[62]. These vortices are considered topological defects with a total phase winding of 2π where n is an integer.

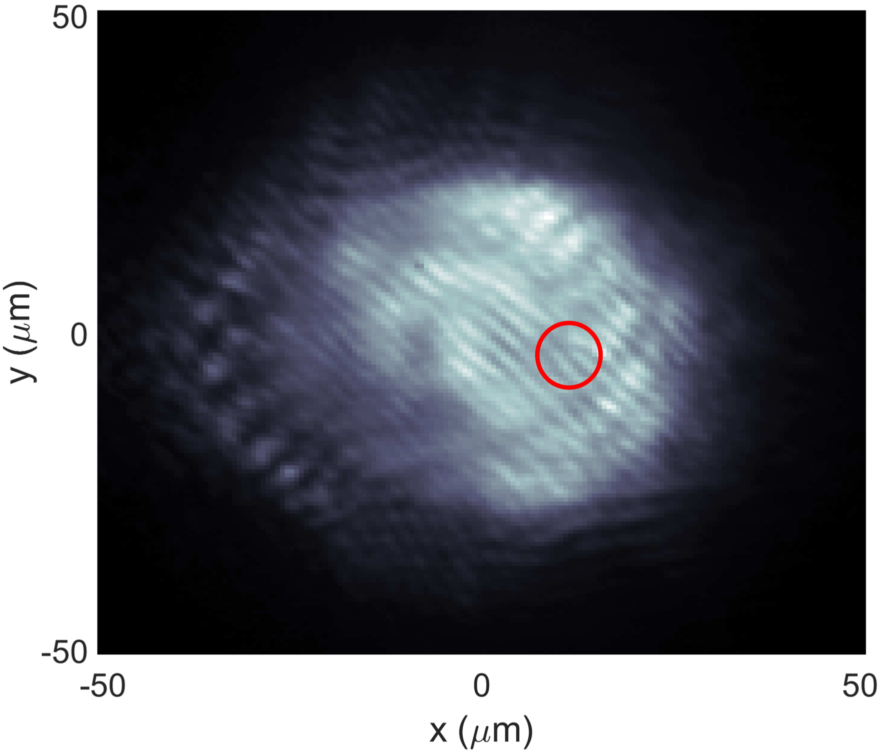

Figure 1.10: Experimentally obtained interferogram showing a polariton condensate formed via parametric scattering past the OPO threshold. The red circle denotes the location of a forked dislocation in the interference pattering indicating the presence of a quantised vortex.

It was later shown that the phase transition during 2D driven non-equilibrium systems such as that of polariton condensation is a Berezinskii–Kosterlitz–Thouless transition, mediated by the annihilation and spontaneous formation of vortex pairs throughout the polariton superfluid[63]. Since the first observation of the nucleation of these vortex pairs in polariton superfluids[64] recent interest has been focussed on using polariton superfluids for analogue gravity experiments in the emerging field of quantum cosmology[7, 8]. Acoustic horizons are used to simulate black holes allowing the study of analogues such Hawking radiation[65, 66] and Penrose effects[67].

Polariton superfluidity has also allowed the observation and study of oblique solitons. These solitons are localised non-diffracting wavepackets within the fluid and arise due to non-linear excitation within a perturbed polariton superfluid. Since the first observation in polariton superfluids[68], solitons in polariton superfluids have been extensively studied on a wide range of platforms such as planar microcavities[69, 70], topological lattices[71] and semiconductor microwires[72] . The nature of these studies has been wide ranging, from reports of Cherenkov radiation in microwire solitons[73] to their implementation in logic gates[74].

1.5 Polariton pseudospin

1.5.1 Spin and polarization

Along with the aforementioned spatial degrees of freedom associated with microcavity polaritons and their constituents, the angular momentum of said particles must be considered. For electrons and holes this takes the form of spin, a property that is closely linked with the polarization of the light involved in the excitation and reabsorption of these carriers. Simply put, spin must be conserved during photoabsorption, thus certain polarisations of light will only excite electrons with certain spin. This effect, known as optical orientation[75] was first discovered in 1968 for bulk semiconductors[76].

For excitons in semiconductor microcavities, the spin of the constituent particles determines the spin of the overall quasiparticle and the case is simple for the electron components which have a spin of $j = \pm\frac{1}{2}$. However, for zinc-blende based semiconductor QWs, there is a splitting of the valence band into two separate bands, leading to the existence of two distinctly different types of holes For the upper band, holes have a spin of $j = \pm\frac{3}{2}$ and are known as heavy holes, whereas in the lower band, holes have a spin of $j = \pm\frac{1}{2}$ and are know as light holes. Since the heavy holes exist in a band closer to the conduction band, excitons are typically formed of electron and heavy hole coupling. This again leads to two distinct cases, excitons with a total spin of $j = \pm 1$, and excitons with a total spin of $j = \pm 2$. This lifting of the degeneracy in the valence band around $k = 0$ arises due to quantum confinement and the elastic strain introduced by the lattice mismatch between the materials making up the quantum well (e.g. InGaAs) [77, 78]. For bulk semiconductors this splitting is not present and the valence band is degenerate around $k = 0$ [79, 80].

Since photon spin is either $j = \pm 1$ or 0 and said spin must be conserved in photoabsorption, polariton formation can only occur in the case of photon coupling with excitons that have spin $j = \pm 1$. The non-optically-active exciton states with total spin $j = \pm 2$ are known as dark excitons whereas the optically active $j = \pm 1$ excitons are known as bright excitons. This leads to polaritons having two possible spin projections in the growth axis of the microcavity, either $j = +1$ when excitons couple with right hand circular polarised light or $j = -1$ when excitons couple with left hand circular polarised light. For the case of coupling with linearly polarised light, the spin projection is a linear combination of the two.

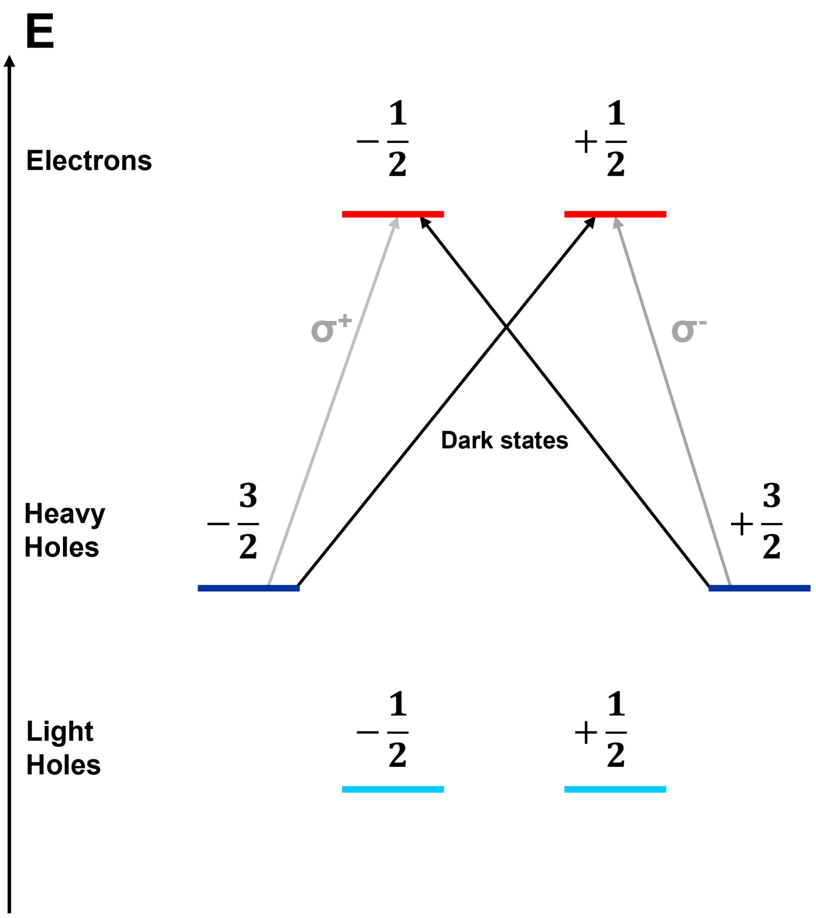

Figure 1.11: Polarised optical transitions with valence splitting in typical zince-blende semiconductor quantum well.

Due to the quasiparticle nature of polaritons, it would be incorrect to call this degree of freedom spin, therefore, whilst it is still analogous to spin in typical particles, it is commonly called pseudospin [81]. The application of the pseudospin formalism is also granted to polaritons, since, due to the neglection of the dark states, excitons can be considered a two level system in zince-blende based semiconductor microcavities[82]. The pseudospin of a polariton takes the form of a 3D vector and encapsulates the constituent exciton spin and along with its dipole moment orientation. Pseudospin can be measured by considering the direction of the Stokes vector of the emitted light from a microcavity. The Stokes vector is made up of four separate parameters as follows

$$S = \begin{bmatrix} S_0 \\ S_1 \\ S_2 \\ S_3 \end{bmatrix}. \tag{1.14}$$

Here S_0 is the total intensity of emitted light. The first Stokes parameter, S_1 is the polarisation measured in the horizontal and vertical basis

$$S_1 = \frac{I_H - I_V}{I_H + I_V}, \tag{1.15}$$

where I_H is the intensity of horizontally polarised light and I_V is the intensity of vertically polarised light. The second Stokes parameter, S_2, is the polarisation measured in the diagonal and anti-diagonal basis

$$S_2 = \frac{I_D - I_{AD}}{I_D + I_{AD}}, \tag{1.16}$$

where I_D is the intensity of diagonally polarised light and I_{AD} is the intensity of anti-diagonally polarised light. The third Stokes parameter, S_3, is the polarisation measured in circular basis

$$S_2 = \frac{I_{\sigma+} - I_{\sigma-}}{I_{\sigma+} + I_{\sigma-}}, \tag{1.17}$$

where $I_{\sigma+}$ is the intensity of right circularly polarised light and $I_{\sigma-}$ is the intensity of left circular polarised light. The superposition of these parameters for polaritons gives the Stokes vector which can be visualised in three dimensional space using the Poincaré sphere (Figure 1.12). Here the direction of arrow determines the polarisation of the light whilst the length of the arrow determines the degree of this polarisation.

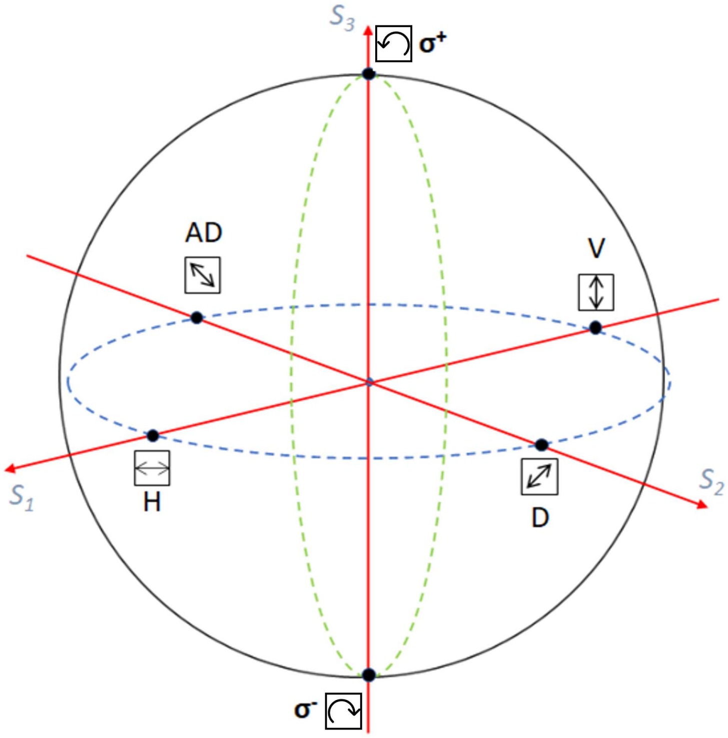

Figure 1.12: Poincaré sphere used to visualise the polarisation of light.

1.5.2 TE-TM splitting

Upon reflection from the dielectric mirrors in a Fabry–Pérot microcavity, a photonic mode will experience a phase delay dependent on the angle [83] and polarisation of the mode[84]. The phase delay is a result of a mismatch between the centre of the cavity stopband and the bare Fabry–Pérot frequency [84], this mismatch is determined by the variation in the refractive indices of the DBR materials. In experimental terms this can be interpreted as a difference in reflectivity (i.e. penetration depth of photonic mode) of the DBR's depending on polarisation and angle of incidence, leading to polaritons with different pseudospins having different values of $k_{||}$ and a splitting observed in the dispersion when resolving in linear polarisation.

This polarisation-angle dependency of reflectivity is known as TE-TM splitting, or sometimes longitudinal-transverse splitting, and leads to two distinct branches in the LPB and UPB. These two branches have a slightly different curvature and hence lead to different polariton effective masses. There is no energy splitting at $k_{||} = 0$ but it increases with angle until it reaches a maximum at the inflection point of the LPB. After this inflection point, the splitting decreases as the polaritons become more excitonic. The source of exciton TE-TM splitting is different to that of photonic TE-TM splitting and is usually much smaller, hence the decrease in the splitting. Exciton TE-TM splitting is caused by a wavevector dependence of the exciton dipole moment orientation in the context of the long-range exciton exchange interaction [85]. However, as mentioned, this splitting is negligible relative to the photonic case so is only relevant when dealing with highly excitonic polaritons. The photonic TE-TM splitting can be modelled as a magnetic field acting on the pseudospin of polaritons in a microcavity[86] and is analogous to the spin splitting seen in electrons in atomic orbitals. This effectively couples the propagation of polaritons (determined by the wave vector) to the pseudospin leading to TE-TM splitting sometimes being called photonic spin-orbit coupling[87]. This effective magnetic field acting on polaritons in the circular polarization basis is given as[86]

$$\Omega(k) = \left(\frac{\Delta(k)_{TE-TM}}{\hbar} cos2\theta, \frac{\Delta(k)_{TE-TM}}{\hbar} sin2\theta, 0 \right), \tag{1.18}$$

where θ is the in-plane polariton propagation angle within the cavity ($\theta = arctan(k_y/k_x)$) and $\Delta(k)_{TE-TM}$ is the value of splitting in the linear polarization basis for a given value of k. Note that the value for the field in the z-direction is zero meaning the field only acts in-plane in the microcavity. To visualise this TE-TM splitting induced magnetic field, it can be plotted in k-space to show the direction and distribution as a function of k_x and k_y.

For polaritons within the same plane shown in Figure 1.13, the field causes a precession of pseudospin orientation dependant on the direction of the field, and, since the direction of the field is dependant on k, polariton polarisation textures are visible in both reciprocal and real space. This effect is best observed in the optical spin Hall effect (OSHE).

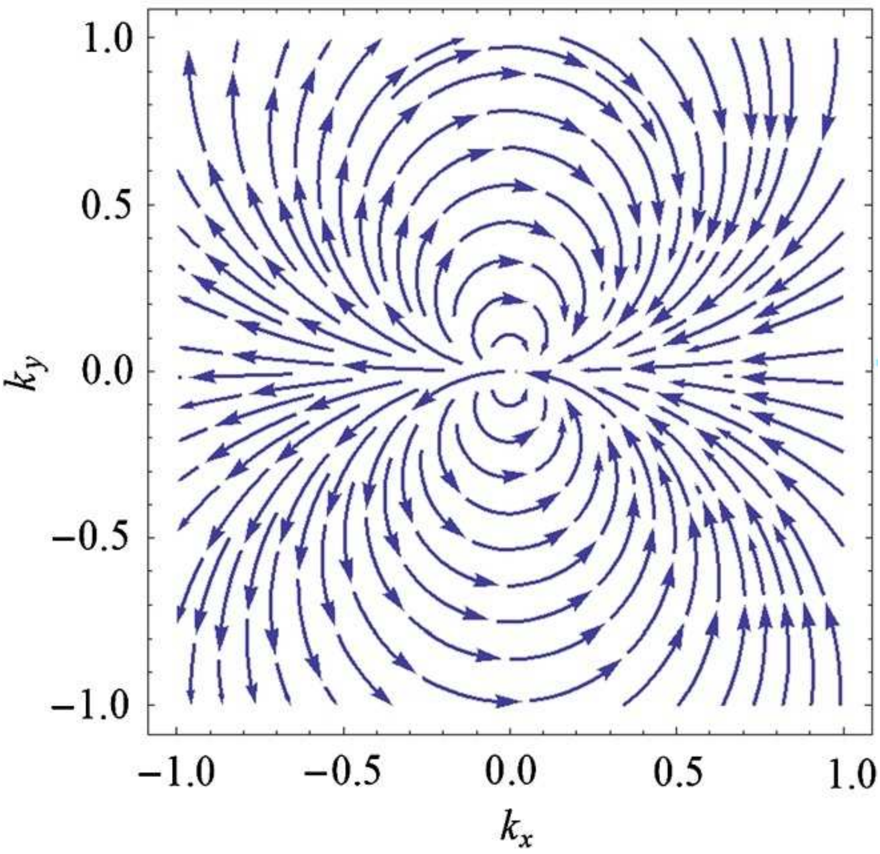

Figure 1.13: Direction and distribution of magnetic field due to TE-TM splitting shown in reciprocal space around a degenerate k=0 point. Taken and adapted from [88].

1.5.3 Optical spin Hall effect

First predicted and later observed by Kavokin et al.[89, 90], the OSHE concerns the formation of polarisation textures in reciprocal and real space due to pseudospin precession around a TE-TM induced magnetic field. In reciprocal space this takes the form of quadrants of polarisation forming around the Rayleigh scattering ring. This isoenergetic ring is formed when polaritons initially scatter away from the excitation spot on a microcavity due to anisotropy in the microcavity structure. To conserve overall value of $k_{||}$, the values of k_x and k_y may individually change but $k_{||}$ and initial polarisation state (either TE or TM) must remain the same. The result is a ring distribution of states in reciprocal space when observing far field emission. However, due to the varying direction of the TE-TM induced magnetic field in k-space (see Figure 1.13) an anisotropy in polarisation states around the Rayleigh ring is formed leading to distinct areas of polarisation states around the elastic circle, otherwise known as quadrants. Owing to the fact the magnetic field direction winds once over an angle of 2π, opposing quadrants will have states of the same polarisation, either σ^+ or σ^-. This evolution of pseudospin around the elastic circle can be described using the following precession equation [90]

$$\frac{\partial \boldsymbol{S}}{\partial t} = \boldsymbol{S} \times \boldsymbol{\Omega}(\boldsymbol{k}) + \frac{\boldsymbol{S_0}}{\tau_1} - \frac{\boldsymbol{S}}{\tau}, \tag{1.19}$$

Where τ_1 is the Rayleigh scattering time constant and τ is the polariton lifetime. Eqn.(1.19) can be split into three terms, the first term described the precession of the pseudospin, the second terms describes the scattering from the initial site and the third term describes the radiative relaxation.

Figure 1.14 shows a visualisation of the precession of polariton pseudospin on the Poincaré sphere. For example, when the initial pseudospin is in the S_1 direction (horizontally polarised)and the magnetic field is in the S_2 direction, the pseudospin will precess until it is orientated in the S_3 direction (σ^+ polarised). The opposite holds true if the magnetic field direction is switched to the -y-direction. When observing the real space equivalent of this, spin currents become visible due to the polarisation dependant ballistic propagation of polaritons away from the centre of excitation. These spin currents are best viewed when plotting the polarisation textures using the Stokes parameters.

Many recent publications have capitalised on the non-linear interactions of polaritons in the context of the OSHE. A key one shows that the spin anisotropy of polariton interactions leads to the quadrants in real space to be spatially compressed[91]. In this configuration, rather than exciting at well defined value of k_x and k_y on the elastic circle, the laser is focused to a small spot and perpendicular to the microcavity. This small laser spot on the sample leads to a large spot in reciprocal space, more specifically a spot that is sufficiently large enough to

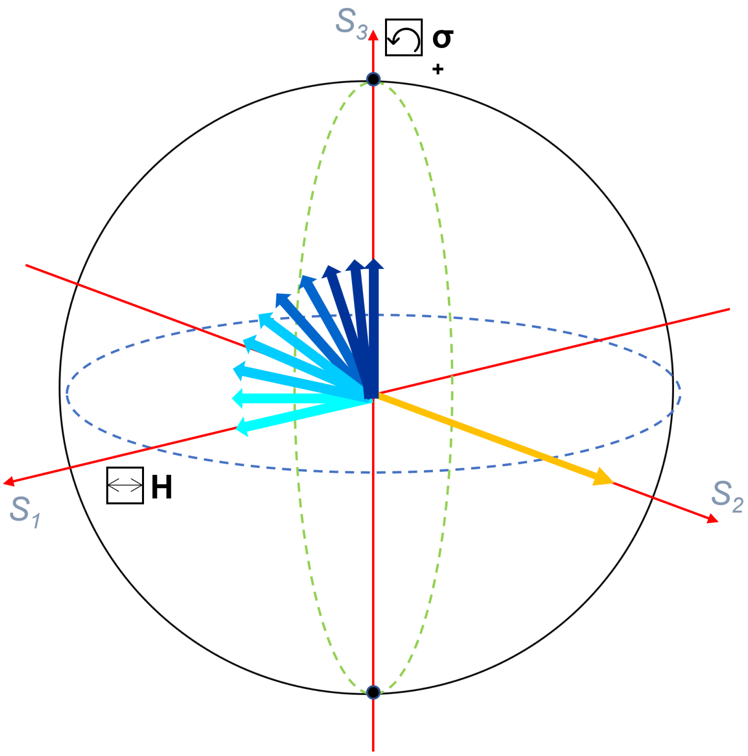

Figure 1.14: Precession shown on the Poincaré with the pseudospin initially with polarisation H (light blue arrow) and then rotating through to σ^+ (dark blue arrow) when the magnetic field is orientated in the S_2 direction (yellow arrow).

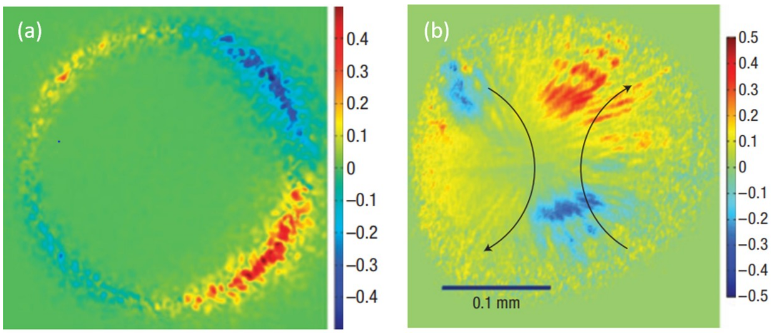

Figure 1.15: (a) OSHE in k-space collection represented by the S_3 parameter. (b) OSHE in real space collection represented by the S_3 parameter, with arrows denoting the direction of the spin currents. Both (a) and (b) taken from [90].

directly excite the elastic circle over all values of k_x and k_y for which there are viable polariton states.

1.6 Polaritons periodic potentials

1.6.1 Etched micropillars

The engineering of potential landscapes has been a notable trend in polaritons studies in more recent times[92, 93], with their popularity for such research owed to the freedom of trapping methods. Due to the hybrid nature of polaritons, they can be trapped using either their excitonic component [94, 95] or photonic component. The latter case involves the creation of periodic potentials in the form of lattices to modulate the potential energy landscape experienced by polaritons. Methods to create these lattices include the metal mask technique[96], replacing the top DBR with a high contrast grating[97] and creating shallow lateral confinement with mesa traps created by in-growth etching of the cavity layer[98, 99]. However, perhaps the simplest yet most effective method for polariton confinement involves the deep etching of the top DBR of a planar microcavity to create micropillars. A single micropillar etched into the top DBR of a GaAs microcavity will act as small standalone microcavity itself, allowing optical lateral confinement via the GaAs-air interface[100]. This strong confinement arises due to the large differences in the refractive index of GaAs ($n \approx 3.5$) and air ($n \approx 1$) and essentially acts to confine the photonic mode in all spatial dimensions[101]. This then leads to the formation of discrete energy modes, analogous to atomic orbitals, due to the quantisation of the photonic mode in all directions (0D dimensional confinement)[101, 102]. 1D potentials can be introduced by spatially overlapping micropillars to form microwires, with the overlap now allowing the hopping of photonic modes between sites[103]. Hopping is facilitated by the tunnelling of modes through the potential barrier arising from the overlapping of pillars, the amplitude of this potential barrier, J, can be controlled by varying the degree said overlap.

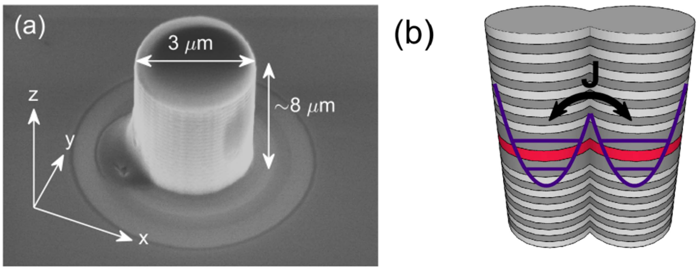

Figure 1.16: (a) A scanning electron microscope image of a single micropillar (b) A diagram showing how the overlap of single micropillars creates a potential barrier with amplitude J which facilitates hopping via tunnelling. The discrete s and p energy states are also visible.

1.6.2 Micropillar lattices

Polariton periodic potential confinement can be taken a step further by introducing a second dimension to the lattices, something first reported in 2011 using a square lattice [104]. For micropillars, 2D lattices can be created by simply extending the overlapping pillars into ordered arrays with desired configurations. The array acts as a photonic analogue to atomic crystal structures where photons now play the role of electrons and the potential landscape is created by air-semiconductor interfaces and the DBR stacks rather than atoms. Many types of lattices exist to confine polaritons, often leading to distinct unique state distributions such as the non-dispersive flatbands in 2D Lieb lattices[105] and 1D stub lattices[106] and the Dirac cones and edge states of honeycomb lattices[107, 108] (see subsection 1.9.3). These lattice structures act to heavily modify the polariton dispersion, creating fine band structures with varying dispersive and photon mobility properties along with forbidden energy gaps.

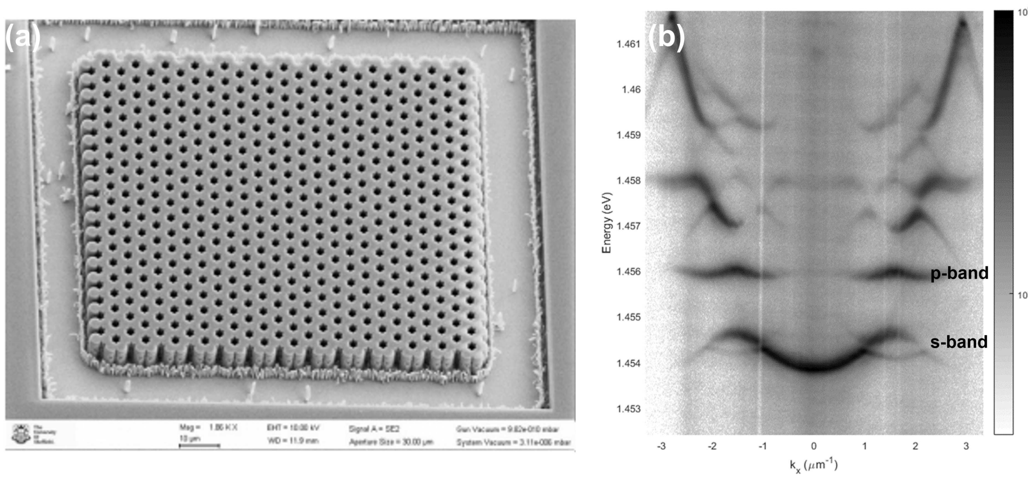

Figure 1.17: (a) A scanning electron microscope image showing an etched micropillar array in the form of a honeycomb lattice. (b) Experimentally obtained PL image from the device in (a) showing the heavily modified LPB dispersion. The *s* and *p* bands are labelled and arise due to the ground and first excited discrete states of the micropillars. The non-labelled bands above these are the higher order discrete states of the micropillars.

1.6.3 Band structure formation

Periodic potential modulation for laterally confined polaritons leads to heavy modification of the allowed $k_{||}$ states within a microcavity. This takes the form of bandstructure formation in the polariton dispersion at varying energy and wave vectors (see Figure 1.17). The source of this bandstructure formation can be understood when considering the Bloch theorem, assuming that the periodic potential (due to the periodic structure of the micropillars) is applied only to the photonic fraction of the polariton. For a wavefunction, Ψ at position, r, under the an imposed periodic lattice potential described by the periodic function, u_r, the Bloch theorem states

$$\boldsymbol{\Psi}_{\boldsymbol{k}}(\boldsymbol{r}) = u_r(\boldsymbol{r})e^{(\boldsymbol{i}\boldsymbol{k}\cdot\boldsymbol{r})}. \tag{1.20}$$

From this, the energy of photonic Bloch bands can be calculated and introduced to the equation for the energy of the LPB given in Eqn.(1.9) to find the energy of the n^{th} lower polariton band, $E_{LP,n}$

$$E_{LPB,n}(k_{||}) = \frac{1}{2}[E_x + E_{cn} - \sqrt{\hbar^2\Omega^2 + (E_{cn} - E_x)^2}, \tag{1.21}$$

where E_{cn} is the energy of the photonic Bloch bands. Alternatively, the band structure for the LPB can be directly calculated by considering eigenvalue solutions for polariton Bloch states $u_k(\boldsymbol{r}) = u_k(\boldsymbol{r} + \boldsymbol{a})$ in the effective potential $V(\boldsymbol{r}) = V(\boldsymbol{r} + \boldsymbol{a})$ acting in plane on the polaritons. The eigenvalue problem is given as

$$\left[\frac{\hbar^2}{2m_{LPB}}(-i\nabla + \boldsymbol{k}_{||})^2 + V(\boldsymbol{r})\right]u_{n,k}(\boldsymbol{r}) = E_n(\boldsymbol{k})u_{n,k}(\boldsymbol{r}), \tag{1.22}$$

where m_{LPB} is the effective mass for polariton in the planar region and n is the band index.

1.7 Waveguide polaritons

1.7.1 Waveguides

There is keen interest in photonics around the use of optical waveguides owing to their inherent horizontal configuration, something that makes them particularly suited to potential integration with on chip circuits. A typical optical waveguide will use the principles of total internal reflection (TIR) for confinement, this TIR takes place on the boundary between the waveguide material and another, similar dielectric material with a significantly different refractive index. For the simplest case of a planar waveguide, the high index core layer is sandwiched between two low index cladding layers. The mode is confined only in the direction normal to propagation (1D confinement). Alternatively the top layer of dielectric material may be removed and the TIR is provided by the material-air interface, provided that $n_{material}$ is significantly higher than n_{air}. The work in this thesis concerns waveguides that confine coupled modes in 1-dimension, these are typically known as slab waveguides, an example of which can be seen in Figure 1.18.

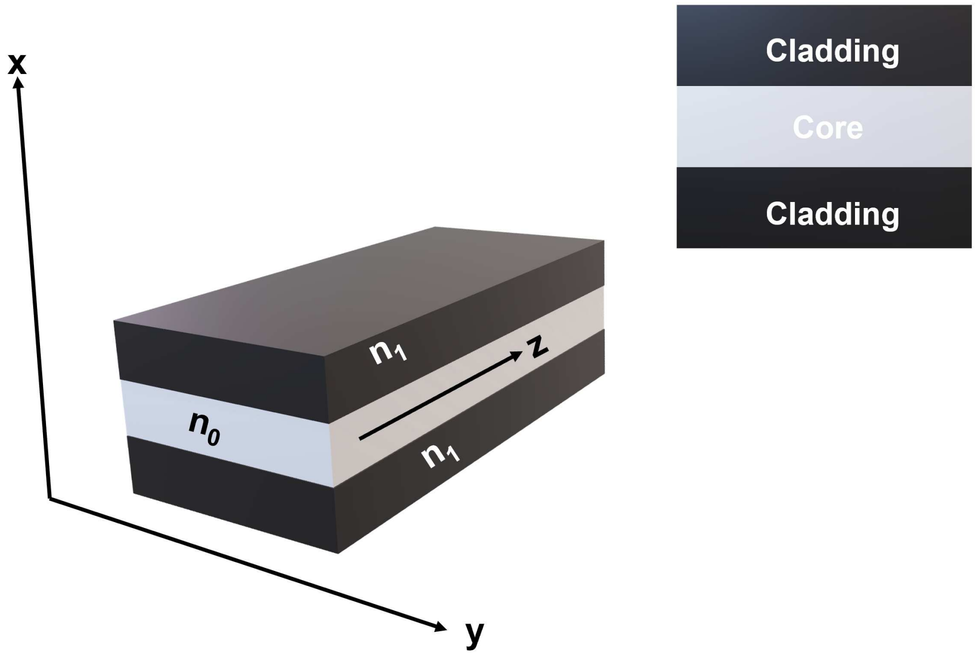

Figure 1.18: Schematic of typical slab waveguide with propagation in the z direction.

A waveguide will only allow the propagation of modes with specific wavelengths, these modes are known as guided modes and are in-part determined by the structure of the waveguide. More specifically, they satisfy the homogeneous wave equation for the waveguide materials and the boundary conditions imposed by the interfaces of the cladding and core. To calculate the guided modes of a waveguide, the conditions of TIR must first be considered

$$\theta_{crit} \leq sin^{-1}\sqrt{n_0^2 - n_1^2}, \tag{1.23}$$

where θ_{crit} is the critical angle of incidence i.e. the minimum angle of incidence of a mode at the core-cladding interface for TIR to occur, n_0 is the refractive index of the core and n_1 is the refractive index of the cladding. Now, considering a plane wave confined in the x-direction with propagation in the z-direction, the wavelength and z-direction wavevector in the core are $\lambda = \frac{\lambda_0}{n_0}$ and $\beta = k_0 n_0$

respectively, where λ_0 is the wavelength in vacuum and k_0 is the wavevector in vacuum ($k_0 = \frac{2\pi}{\lambda_0}$). Now considering the wavevector defined for a mode in the cladding material, $\kappa = kn_1$, guided modes can be defined as modes that meet the condition $\beta > \kappa$. For these modes, propagation is allowed and they will eventually escape the finite waveguide at the end opposite to where they were coupled into the waveguide to be collected during experiments. Guided modes are also limited by the restriction of the speed of light for a propagating mode, i.e. β. Due to the fact that guided modes must constructively interfere, the phase change of a total trip must be a multiple of 2π, thus allowed modes are only able to have discrete values between β and κ. The lowest order of these discrete modes is the fundamental mode and is defined by the mode with the lowest allowed in-plane wave vector.

1.8 Coupling techniques

An obstacle in the use of optical waveguides is achieving a high coupling efficiency when transmitting optical modes into the guide. A common method, known as fibre edge coupling, is to directly match the output of an optical fibre to that of the desired mode and to then shine it to the cleaved edge of the waveguide. However, this often requires an awkward set-up, especially when using a cryostat as in experiments using GaAs based devices. It also often requires the tapering of the waveguide width to match the width of the fibre [109, 110]. A more suitable approach to mode coupling into waveguides, and one used in this thesis, involves the use of grating coupling. A grating coupler is simply a diffraction grating etched at either propagation direction end of the waveguide and is used to couple the mode into and out of the device[111].

When considering the coupling into the device, to achieve mode matching, the grating period, Λ, is chosen such that the spatial harmonics created by the grating, defined by multiples of $\pm\frac{2\pi}{\Lambda}$, match the desired mode. The input angle, θ, of the

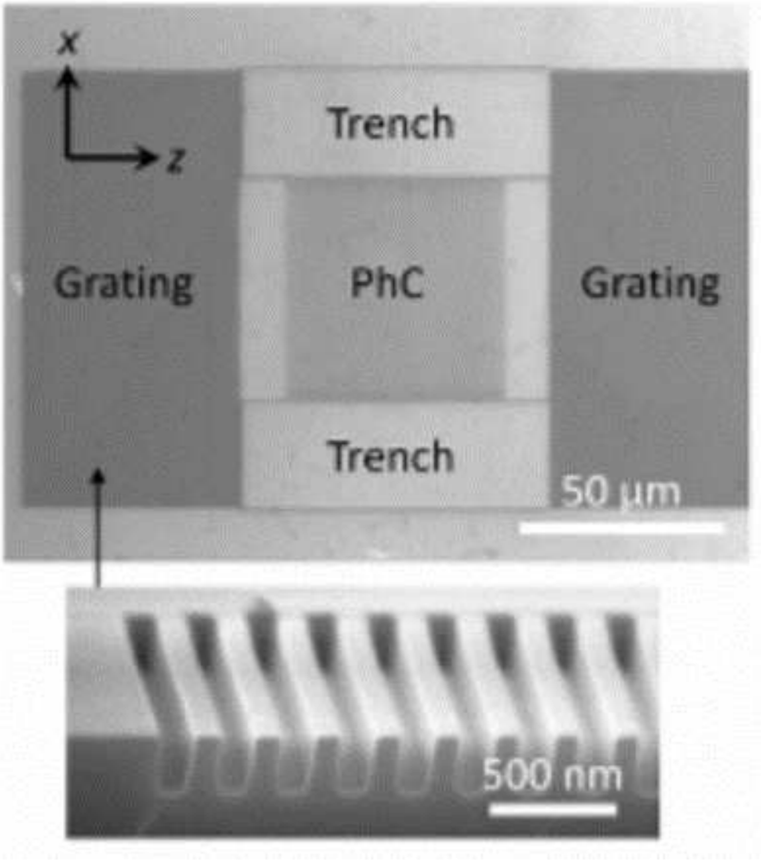

Figure 1.19: Magnified image of a semiconductor slab waveguide showing the grating either end in the z-direction. Also included is a scanning electron microscope image showing a close up of the coupling grating. For PhC label see Section 1.73. Image taken by Dr Charles Whittaker.

light being coupled into the device is then defined as

$$ksin(\theta) = \beta \pm \frac{2\pi}{\Lambda}, \tag{1.24}$$

where Λ is the grating period. This can be reversed to consider emission angle and is one of the key benefits of diffraction gratings, since by simply considering the angle of emission, optical information about the mode inside the waveguide via β can be found with relative ease.

1.8.1 Polaritons in waveguides

Whilst traditional polariton experiments use Fabry-Perot microcavities to facilitate light-matter hybridisation, alternative platforms have emerged in more recent years. A prime example of such an alternative is that of semiconductor waveguides, the implementation of which for polariton studies was first theoretically predicted nearly 20 years ago[112]. The basic principle for polariton formation in waveguides remains the same, with the two key ingredients being and excitonic material layer with embedded quantum wells surrounded by layers with means of strongly confining optical modes. In the case of waveguides, said optical modes are confined using the aforementioned principles of TIR exhibited in optical waveguides rather than the optical confinement via DBR stacks as in microcavities. The same anti-nodal placement of the quantum wells is used in waveguides to optimise the efficiency of strong coupling between the exciton and photonic modes.

Whilst earlier work showed strong coupling in organic waveguides[113], the first demonstration of polaritons using inorganic materials was 2013 by P.M. Walker et al.[114] whereby a semiconductor waveguide was used to facilitate the strong coupling between QW excitons and a guided mode. In this work it was observed that strong spatial confinement of the optical mode led to large splitting between LPB and UPB of between 5-6meV. The use of grating couplers allowed direct access the polariton dispersion and unambiguous confirmation of the characteristic anti-crossing behaviours synonymous with strong coupling. This work also demonstrated a polariton decay length of 280μm along with a group velocity of 26μm ps^{-1}.

The motivation for the development of waveguide polariton systems arose due the growing interest in the properties of propagating polaritons, which required many of the characteristics provided by waveguides such as large propagation distances, large Rabi-splitting and relative ease of patterning[114]. The former two of these characteristics arise from the inherent lower losses afforded by the use of total internal reflection along with the reduced mode volume increasing coupling to QW excitons when compared to microcavities[115]. A long running motivation for the study and use of waveguides in polariton physics is their horizontal configuration, something that naturally lends waveguide polaritons to suitability and more straightforward implementation in polariton based integrated circuits. Since the first demonstration of polaritons in GaAs based waveguides, they have been reported in many experiments using an array of different materials such as ZnO[116], GaN[117] and TMD[118] along with further experiments using GaAs[119] and organic materials[120]. More recently, non-linear polariton-polariton interactions have been observed for waveguide polaritons including the observations of both bright[121] and dark solitons[122], spatiotemporal continuum generation[123] and polariton lasing[124]. Edge-emitting polariton lasers have also been observed for waveguide polaritons, with suggestions such states could eventually offer topological protection for waveguide based polariton integrated circuits[116].

1.9 Topological polaritons

1.9.1 Topology

Topology is a field of mathematics that concerns the classification of objects based on their invariant properties under continuous deformation. An example of such classification is the genus of a 3D object, equivalent to the number of holes in the object. In this context, the number of holes is the topological invariant and will remain unchanged under constant deformation. Topologically identical shapes are those that can be deformed into one another (without tearing), and the number of holes remains the same. If the number of holes were to change, or more generally the topological invariant of any system changes, a topological phase transition takes place. This notion of geometric classification and invariant properties can be applied to electronic and photonic systems as discussed in the next two subsections.

1.9.2 Quantum Hall effect and topological insulators

The original experimental application of topology to solid states physics arose during quantum Hall effect experiments, where the emergence of topological edge states were observed[125]. The application of a magnetic field to a conducting slab material pinned conduction band electrons to the Landau levels and opened up a band gap between the conduction and valence bands. This consequentially turned a conducting material into and insulating one. This also gave rise to quantised Hall currents around the edge of the material which were unidirectional and protected against disorder in the system. This phenomenon was named the integer quantum Hall effect with the edge currents that arose being classified as topologically protected. That is, the currents are protected against perturbations and disorder by the local geometry of the system. To quantify these topological properties of a material or system using a topological invariant, the calculation of the Chern number is used. For an electronic system, this Chern number is calculated by integrating the so called Berry curvature across the whole of the first Brillouin Zone of the material. Qualitatively, this describes the total phase picked up by an electron's wavefunction over a closed path across the overall torus shape of Brillouin zone (the Brillouin zone is considered a torus in the context of topology). For any material with a non-zero Chern number, it can be described as being topological and for electronic conducting materials is expected to have some number of topologically protected edge states.

1.9.3 Topological photonics

As with a large proportion of solid state physics, photonic analogues can be applied with similar results. The same goes for the application of topology to photonic band structures[126, 127], a revelation that has led to the emergence of topological photonics at the forefront of the fields surrounding photonic systems over the past decade[55, 128, 129]. More recently, proposals for the existence of topological polaritons were made by T. Karzig et al. [130] and separately by A.V. Nalitov et al. [131] with these new states given the name ”Topolaritons” by the former. These proposals suggested the existence of topological insulators for periodically arranged polaritonic systems, with unidirectional edge states for propagating polaritons protected against back scattering. To create these topological polariton states the proposals required the breaking of time reversal symmetry in the underlying semiconductor via a magnetic field (such as a Zeeman field) and the ability to open topological gaps in the bandstructure of the system with said magnetic field. It was suggested that these band gaps could be opened using periodic lattice potentials or by applying strain to the embedded quantum wells in a microcavity system. The proposals then suggested that within these gaps, the topologically protected edge states are expected to arise with the system having a Chern number, C=±2

. These proposals were experimentally realised shortly after by S. Klembt et al. [132] using polaritons in a honeycomb lattice semiconductor microcavity. As in the proposals, an external magnetic field is used to break time reversal symmetry and is also used to open topological gaps at the Dirac points in the lattice polariton band structure via Zeeman splitting and spin-orbit coupling interactions. Photons were then resonantly injected via a pump laser into these newly opened topological gaps with the resulting states being the aforementioned topologically protected edge states. This work then goes to directly observe this topological protection as the propagating edge state polaritons pass a point like defect and round a 90° corner without scattering in both cases. It was also observed that the direction of propagation of the edge states is revered when the applied magnetic field is reversed. Other observations of edge states on honeycomb lattice systems have also been made[107, 108]. It is hoped that research into topological photonics such as those mentioned will lead to integration of on-chip topologically protected photon transport with protection against scattering losses.

Chapter 2

Experimental methods

2.1 Experimental set-ups

2.1.1 Real space imaging

The real space image of emission carries all of the information regarding spatial distribution of the polaritons in the sample. To obtain said information, a real space image must be formed on the CCD, this is done by collecting emission with an objective lens and guiding the outputted collimated image to the spectrometer slit. A telescope can be introduced consisting of intermediate lenses to magnify or demagnify the real space image formed on the CCD.

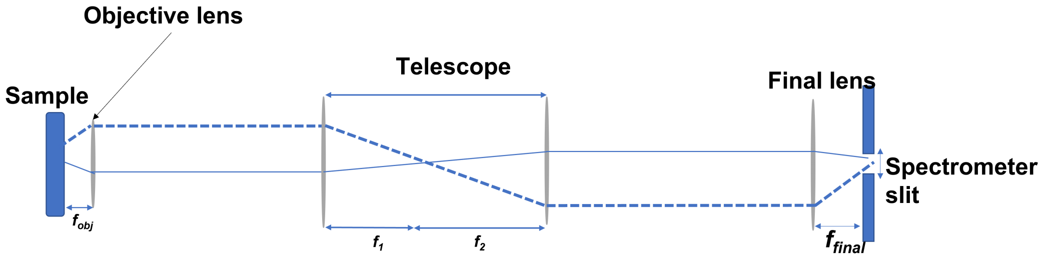

Figure 2.1: Simplified schematic showing the simplest real imaging set-up. The PL emission from different spatial coordinates on the sample is carried over to different spatial coordinates in the image formed on the CCD. The telescope magnifies or demagnifies this image.

2.1.2 Fourier imaging

Fourier imaging allows the visualisation of the angular properties of the photoluminescent emission from the sample. From this angular information, the in-plane momentum properties of the polaritons can be deduced allowing the plotting of the E-k dispersion. Fourier imaging works by taking advantage of the image formed in the Fourier plane of the collection objective. By placing a lens confocal with this Fourier plane, the far-field Fourier emission can be imaged onto the CCD with careful guiding of the image to the spectrometer via intermediate lenses. In its simplest configuration, the Fourier imaging set-up consists of a single intermediate lens that acts as the k-space lens to image to Fourier plane and a final lens to focus the image to the spectrometer slit and towards CCD. Since anything emitted at the same angle crosses the Fourier plane at the same point, the spatial position of emission in the image formed on the CCD translates to angular information. When imaging far-field Fourier images, all spatial information is lost. The addition of a telescope after the k-space lens or before the final lens can be used to magnify or demagnify the image formed on the CCD.

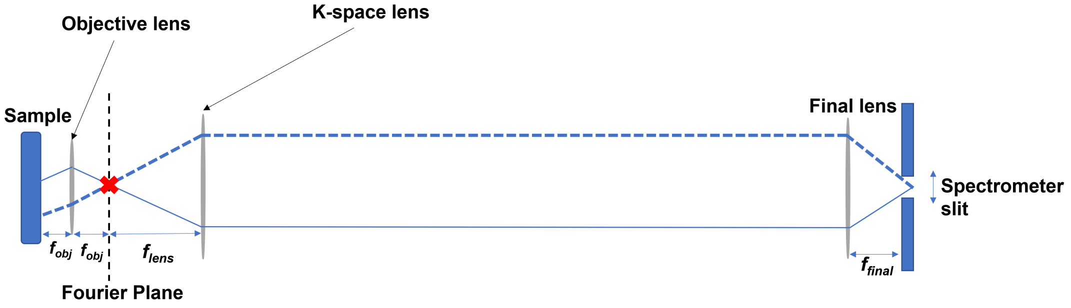

Figure 2.2: Simplified schematic showing the simplest k-space imaging set-up. PL emission at the same angle is focused to the same point in the Fourier plane (red cross). Since the Fourier plane is being imaged, the spatial coordinates of the image directly correlate to emission angle.

2.1.3 Reflection configuration

In the reflection configuration, the lens used to excite the sample is the same lens used to collect emission i.e. the sample is excited on the same side emission is collected from. This configuration is particularly useful for non-resonant excitation methods such as taking dispersions and sample characterisation as it only requires the focusing of one objective lens and the alignment of one optical path.

The spot was also visible on the sample for wavelengths that wouldn't typically be visible when transmitted through the sample.

For the reflection configuration, a Power Technology Ltd A743 637nm red diode laser is used with the LDCU5 control box. The laser is guided to a beam splitter (BS) placed in front the f = 10mm microscope objective lens (N.A.=0.42), the BS transmits 50% of the beam into the objective which then focuses it onto the sample. The other 50% is collected in a beam dump. The resulting emission is then collected by the objective and passes straight through the BS towards the spectrometer. The path between the BS and the spectrometer contains several intermediate lenses. The configuration for these lenses varies slightly between experiments but typically provides an overall magnification of between m=15-20x and an effective focal length in k-space of f=4.5-6mm. The typical reflection lens configurations is as follows: The first intermediate lens (L2) is placed confocal with the back focal plane of the objective, the second intermediate lens (L3) is then placed confocal with L2. Whilst L2 and L3 act as a telescope, they do not magnify the image, rather they shift the it (both real and Fourier) closer to the spectrometer. This is done to allow space for another lens (L4) that acts as the k-space lens in this set-up. The telescope created by L2 and L3 sends a non-magnified collimated real space image towards the spectrometer but when a k-space image is needed, L4 is flipped into the path and placed confocal with L3 to image the Fourier plane of L3 (which in turn is just the shifted image formed in the Fourier plane of L1). This allows the far-field Fourier space emission from the sample to be imaged onto the CCD attached to the spectrometer. Finally, regardless of the type of image, it is sent to a final lens that focuses it to the slit of the spectrometer to allow spectral analysis. A white light is also integrated into this set-up to allow visible observation of the sample surface, this white light uses the same optical path as the laser.

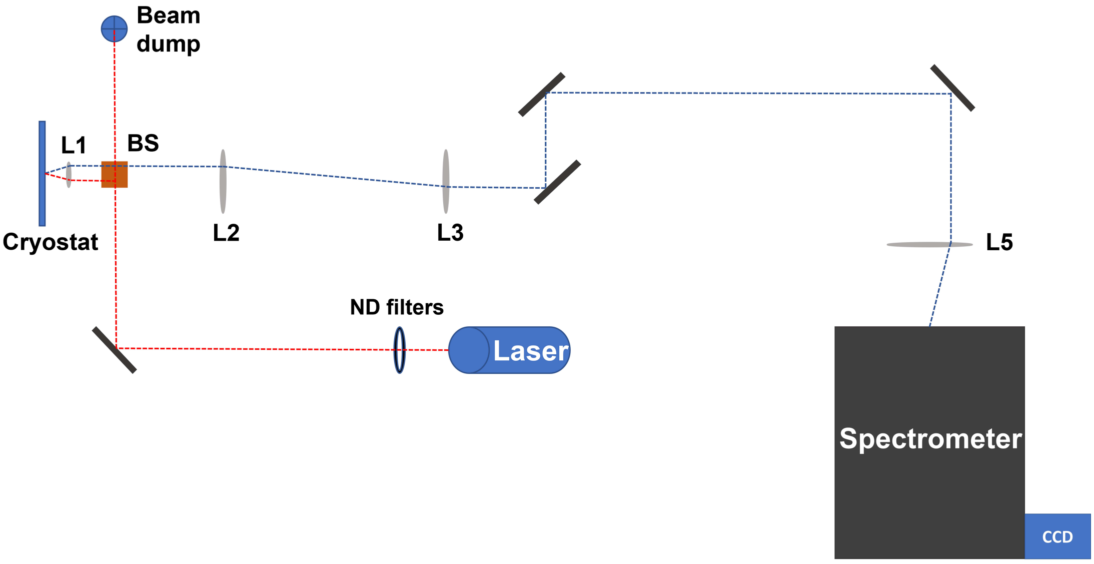

Figure 2.3: Simplified schematic showing the real space imaging set-up in reflection configuration. The excitation beam is shown in red and the collected emission is shown in blue.

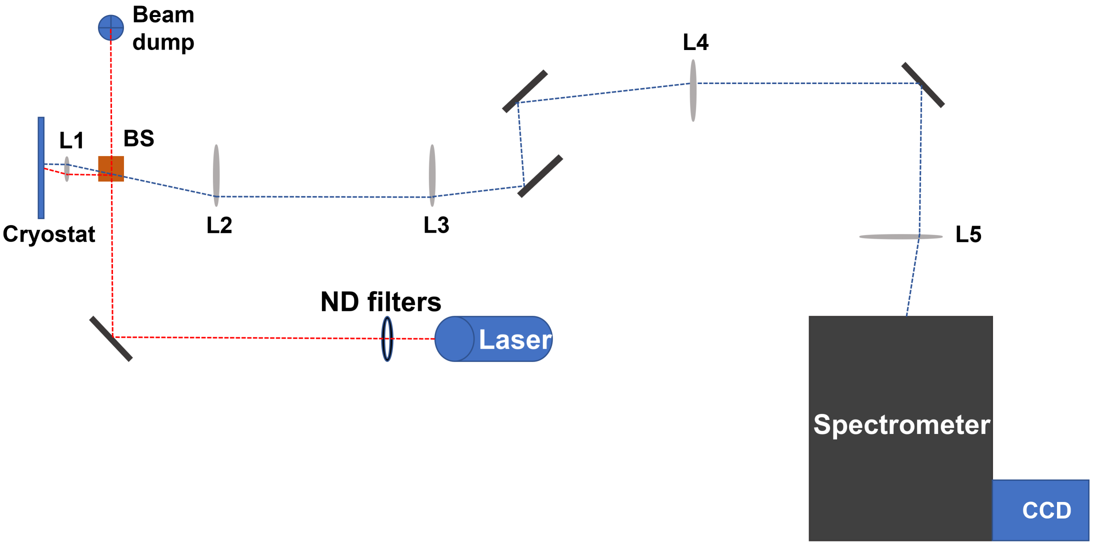

Figure 2.4: Simplified schematic showing the k-space imaging set-up in reflection configuration. The excitation beam is shown in red and the collected emission is shown in blue. The addition of L4 allows the imaging of the k-space image formed in the back focal plane of L1.

2.1.4 Transmission configuration

The transmission configuration involves two separate optical paths, the excitation path and the collection path. The basic principle of this configuration is to excite the sample from the opposite side to that from which emission is collected. This is particularly useful for experiments that required angle excitation of the sample or the modulation of the spot (see subsections 2.1.6 and 2.3.2). Different experiments in this thesis use different set-ups for the transmission configuration but the main underlying principles remains the same. In the simplest configuration the laser outputs a beam that is then collimated using a non-magnifying telescope. To alter spot size on the sample, the ratio of the focal lengths in this telescope is changed to expand or shrink the beam width. The beam is then guided to a translation stage directly behind the cryostat to allow for angled excitation. From here it is guided to an objective (L0) where it is focused to the back of the sample in the cryostat. In Chapter 4 this objective is a f=50 mm camera objective. In Chapter 5 an f=10 mm microscope objective is used. The resulting emission is then collected in the same optical path as seen in the reflection configuration without the integration of the red diode laser (i.e. all blue lines in Figures 2.3-4).Fourier space imaging can also be achieved in the same way as is the reflection configuration by using L4. A white light source is also used to illuminate the front of the sample to assist in the positioning.

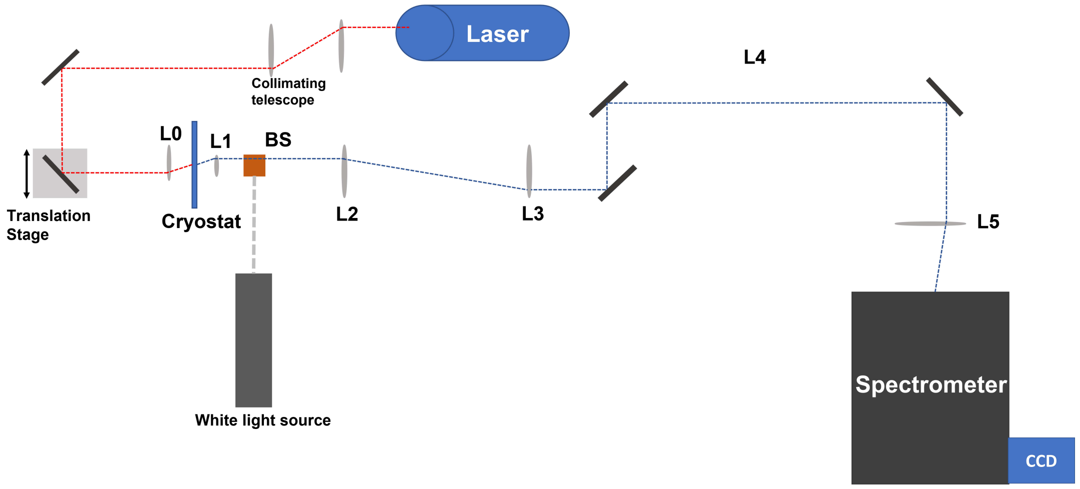

Figure 2.5: Simplified schematic showing the real space imaging set-up in transmission configuration. The excitation beam is shown in red and the collected emission is shown in blue.

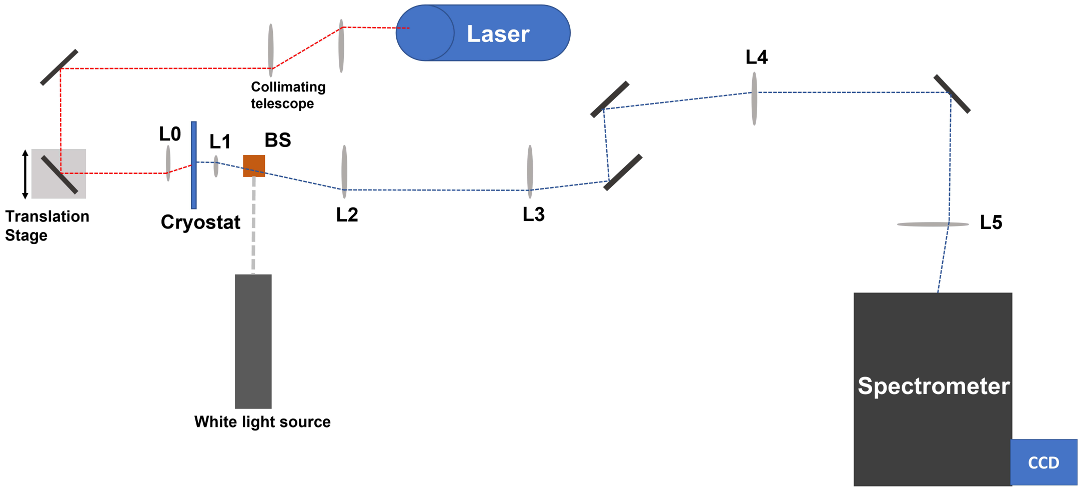

Figure 2.6: Simplified schematic showing the k-space imaging set-up in transmission configuration. The excitation beam is shown in red and the collected emission is shown in blue. The addition of L4 allows the imaging of the k-space image formed in the back focal plane of L1.

2.1.5 Bath cryostat and magnet configuration

An alternative reflection configuration is used in Chapter 3 and allows the integration of the bath cryostat and superconducting magnet. This set-up uses the

637nm diode laser from subsection 2.1.3 but instead this is now fibre coupled to a breadboard atop the cryostat. The following lens notations now concern the lenses in Figure 2.7. L1 is used to focus the beam into the fibre coupler and an optical fibre carries the beam to the output coupler on the breadboard. The outputted beam is collimated by L2 and guided down the optical tube into the cryostat. A telescope is placed along the tube to magnify or demagnify (or just recollimate) the beam depending on the ratio of the telescope lenses focal lengths. The beam is then focused on to the sample by an objective lens (L5) above it. The sample is surrounded by a superconducting magnet inside the cryostat that is able to apply a magnetic field of up to $\pm 9T$. The magnet can be controlled by a separate control box elsewhere in the lab. The emission is then collected by L5 and guided back up through the same path as the excitation beam to the top of the cryostat. A beam splitter is then used to rotate the emission by 90° and guide it towards a periscope. The periscope is used to translate the emission back down to the height of the optical bench where after passing through another telescope consisting of L7 and L8 it is focused to the spectrometer slit by L9 towards the CCD. For Fourier imaging, L6 is flipped into the collection path near the top of the telescope to image the Fourier plane of L3. The sample is mounted on top of a stack of three piezo stages. This allows the fine adjustment of the sample position in three dimensions and is particularly useful in optimising the focus of the image. These stages are controlled externally from the cryostat.

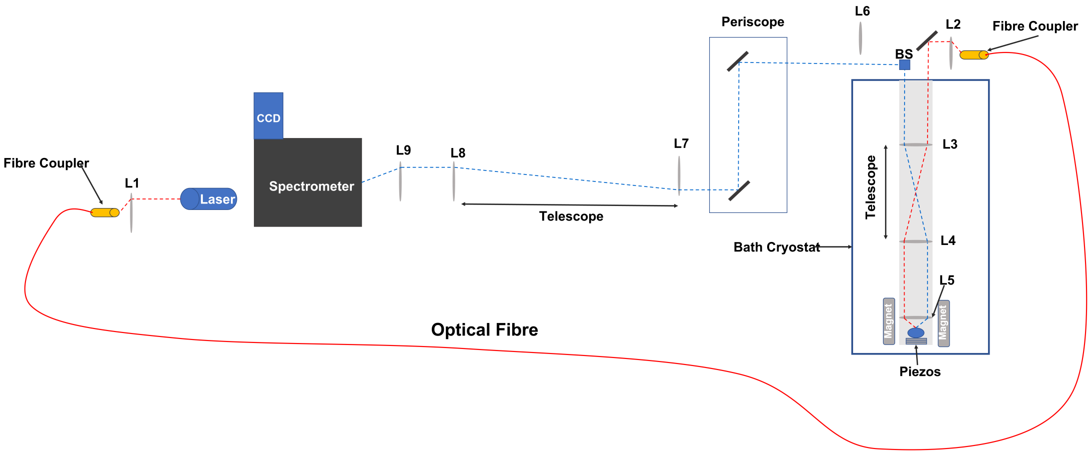

Figure 2.7: Simplified schematic showing the reflection configuration with the integration of the superconducting magnet and bath cryostat. L6 acts as the Fourier lens in the set-up. The excitation beam is shown in red and the collected emission is shown in blue.

2.1.6 Angled excitation

To inject photons at different wavevectors on the polariton dispersion, control over the angle of incidence of the laser on the sample is required. This is done by introducing a translation stage to the last mirror before the excitation objective in the transmission configuration. This stage translates the beam in the x-direction (parallel to the optical bench) across the objective thus changing the angle of incidence. The position of the translation stage relative to normal incidence is related to the excitation angle as follows

$$T = f_{L0} tan(\theta), \tag{2.1}$$

where T is the horizontal offset of the translation stage relative to the position corresponding to normal incidence, f_{L0} is the focal length of the excitation objective and θ is angle of incidence. A visualisation of this is shown in Figure 2.8.

The in-plane wavevector of injected photons can be calculate in terms of the angle of incidence as

$$k_{||} = \frac{2\pi}{\lambda} sin(\theta), \tag{2.2}$$

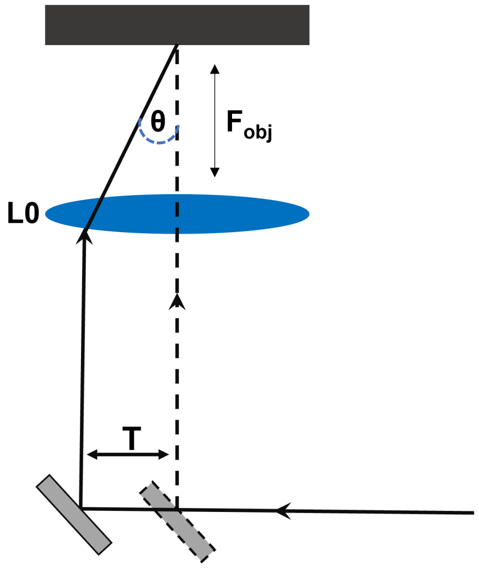

Figure 2.8: Diagram showing how the translated position of the beam on the objective determines the incident angle of the beam on the sample.

where λ is the wavelength of the photons. From this it is clear that to resonantly excite a specific spot on the dispersion, all that is required is tunability of the angle of excitation and the energy of the laser.

2.1.7 Sample cooling

Two methods of sample cooling are used for the work in this thesis. For Chapters 4 and 5, a continuous flow system is used in which the sample is mounted to one end of a copper finger in a cryostat and held in vacuum of 10^{-6} mbar using a turbo vacuum pump to prevent ice crystal formation during cooling. The other end of the copper finger is exposed to a flow of liquid helium (LHe) originating from a dewar and pulled through a transfer tube by a different vacuum pump. The helium leaves the lab towards a liquefier elsewhere in the building for recycling . The cold finger is a long piece of copper that provides excellent thermal conductivity and allows cooling of the sample to 4.5K (however 7-9K is more regularly used) with the temperature monitored via sensors attached to the cold finger. The cold finger also contains a hole that sits parallel to the windows of the cryostat to allow excitation of the sample from both sides.

In Chapter 3 the sample is cooled using a bath cryostat, this method involves mounting the sample in a vacuum sealed tube and immersing it into a tank of LHe. This tank is initially pre-cooled with liquid nitrogen which is then pumped out and the dewar is subsequently filled with LHe. Bath cryostat cooling has the benefit of little maintenance and stable temperatures for samples as, unlike continuous flow, the system is not brought up to room temperature at the end of the day. The cryostat is refilled weekly, this involves pumping compressed helium gas into a dewar attached to the cryostat, which in turn forces LHe into the cryostat. Excitation of the sample can be achieved by guiding the laser down through the top of the sealed tube to the sample at the bottom and then guiding the emission back up again (see subsection 2.1.5).

2.2 Sample characterisation

2.2.1 Dispersion fitting

At times it is useful to characterise new samples to be used in experiments. This involves finding several parameters such as γ, Q-factor and Δ for a given sample. In the latter case, due to variations in cavity length created during growth, detuning can vary across the sample so it is often useful to measure dispersions at different positions on the sample and create a detuning map.

The dispersions are obtained by aligning the centre of the k-space PL image with the spectrometer slit using low power non-resonant excitation. With this CCD data, the peak positions of intensity at each pixel along the x-axis (and thus at each value of $k_{||}$) for the UPB and LPB can be extracted in MATLAB. Using these newly extracted values of $E_{UPB}(k_{||})$ and $E_{LPB}(k_{||})$, whilst also ignoring loss, Eqn.(1.9) can be rearranged to give the Rabi splitting and Exciton resonance as

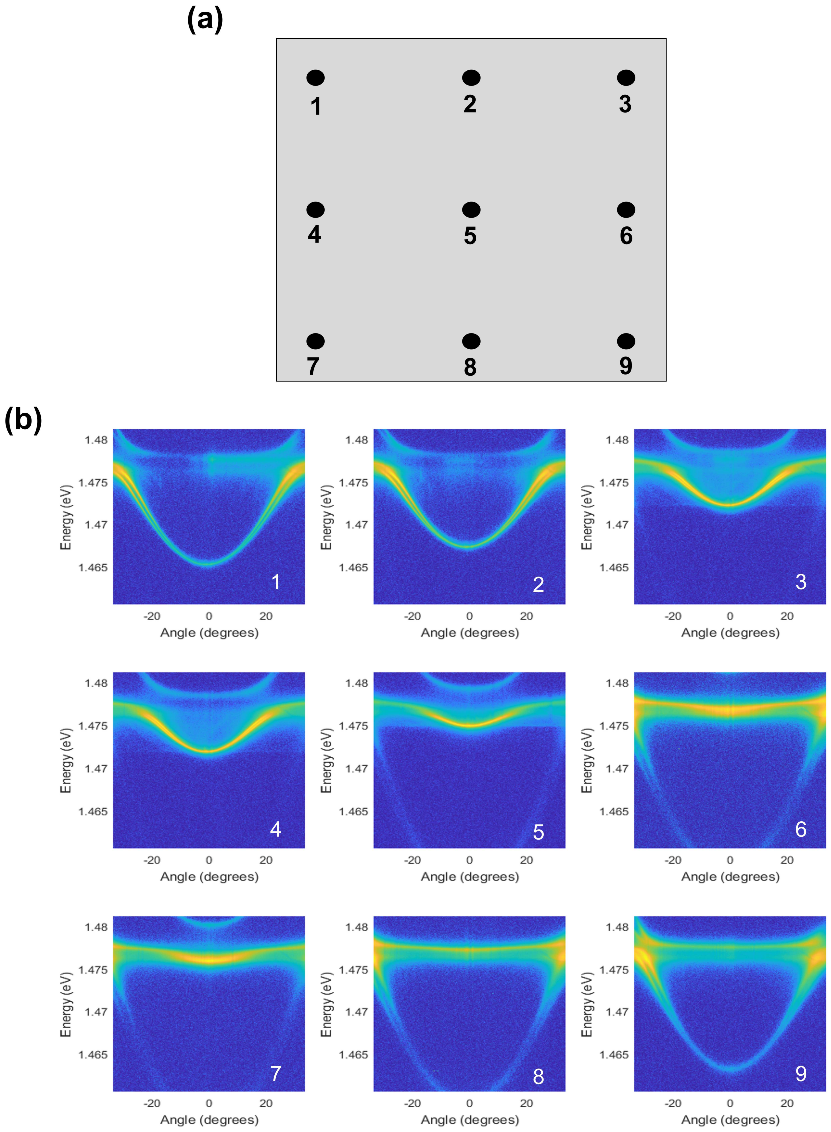

Figure 2.9: (a) Layout of sample showing numbered positions where dispersions are taken.(b) Dispersions taken at different positions corresponding to the sample map in (a), showing how detuning varies across the sample.

$$E_{LPB}(k_{||})E_{UPB}(k_{||}) = E_x(E_{LPB}(k_{||}) + E_{UPB}(k_{||}) - \left[E_x^2] + \frac{1}{2}(\hbar\omega)^2\right]. \tag{2.3}$$

This can then be solved to find E_x and $\hbar\Omega$ using least squares fitting. With extracted curves for the UPB, LPB and exciton resonance, the cavity photon resonance can also be determined thus allowing the calculation of Δ.

As shown in Figure 2.10, the linewidth can also be calculated by finding the full width at half maximum (FWHM) of a fitted Lorentzian peak at $k_{||} = 0$ and from here the Q factor can be found using Eqn.(1.7). This method allows a full

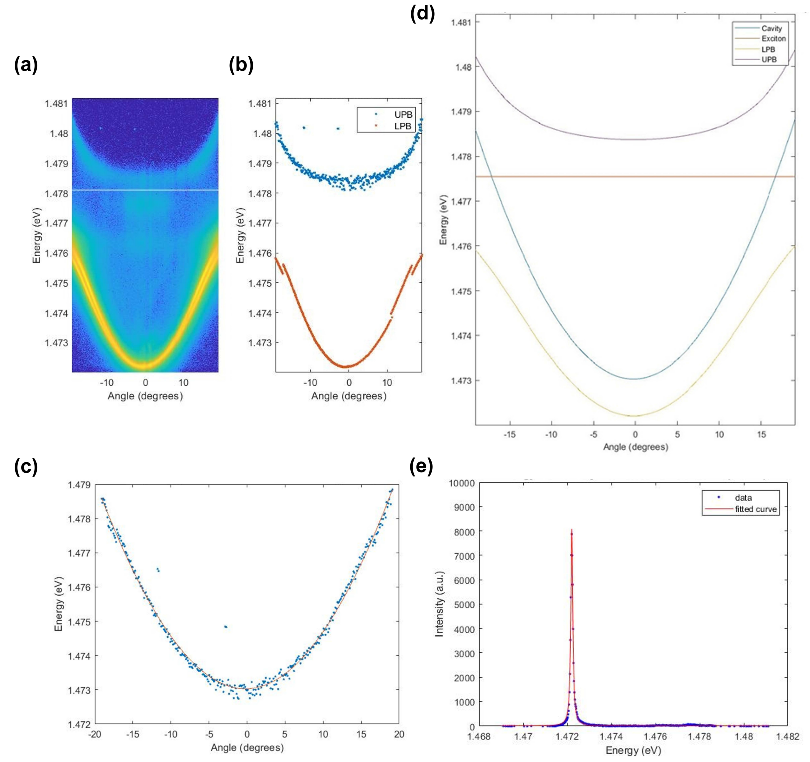

Figure 2.10: (a) Raw CCD data taken at position 3 on the sample map in Figure 2.9 showing the UPB and LPB. (b) Extracted peak positions for the LPB and LPB energies at different angles for same position as in (a).(c) Calculated points for the cavity photon resonance with a fitted curve. This, along with the extracted exciton resonance value of 1.4476eV, gave a value for detuning at position 3 as Δ=-4.7 meV and a Rabi splitting of $\hbar\Omega$= 4.1 meV.(d) Fitted Lorentzian curve for the values of intensity at $k_{||} = 0$ for the LPB. The linewidth is given by the FWHM and has a value of γ=110 μeV thus the Q-factor for this position is Q=13000.

picture of the different parameters for polariton states on a given sample and also allows further characterisation such as determining the Hopfield coefficients and effective mass.

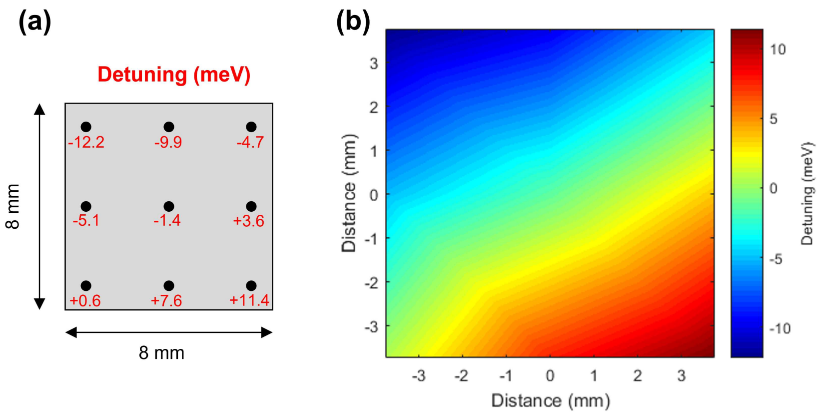

Figure 2.11: (a) Values for detuning (red) shown for each position measured as outlined in the sample map in Figure 2.9. (b) Heat map plotted using the detuning values in (a) to show how the detuning varies across the sample.

2.2.2 Optical tomography

The Fourier image formed in the back focal plane of the objective lens is actually a two-dimensional image with components in k_x and k_y (ignoring intensity). A typical dispersion as displayed in this thesis (such as in Figure 1.5) is taken over a range of values of k_x but is fixed at a single value of k_y (or vice versa). The k_y component that is being imaged can be varied by incrementally scanning the final lens (L5 in Figure 2.3-6) sideways to align a different slice of the 2D far-field emission image with the spectrometer slit. This procedure can also be performed for the real space image and is known as optical tomography.

By using optical tomography it is possible to stack successive CCD dispersive data together to form a 3-dimensional image showing the full energy distribution of polariton states in momentum or real space. Optical tomography can be particularly useful in visualising the bandstructure in polariton lattices and aid in the identification of key points such as the Dirac points or first and second Brillouin zones in a honeycomb lattice. Alternatively, the energy component can be ignored and, using the slices taken from a tomographic scan, a 2D image can be constructed showing purely the momentum distribution of polariton states. For a planar polariton dispersion this will show a isoenergetic circle, akin to looking down from above at the true 3D polariton dispersive cone.

A tomographic scan is relatively simple to undertake in the lab and can be greatly aided by automatic translation stages for the final lens. To do so, the final lens is fixed at an initial position, x_1. If considering momentum space in the lab frame, the first image taken will show a dispersion over k_x and E at a fixed value of k_y. The translation stage is then moved in the x-direction in increments of a set size and at each position, corresponding to a different value of k_y, a dispersion is taken. The result will be a series of separate CCD measurements showing how the dispersion changes with k_y.

In Chapter 4, tomographic scans are used to identify $k_{||}$=0 by finding k_x=0 and using the lowest point in energy on the LPB (k_y=0). Optical tomography is also used to find the Dirac points in a honeycomb lattice in the first Brillouin Zone.

In Chapter 5, tomographic scans are used to identify the P and S flatbands for a 2D Lieb lattice.

2.2.3 Polarisation optics

It is sometimes useful to isolate specific polarisations of light, whether it is for collection of polarised emission or exciting with a specific polarisation. Waveplates are the main equipment used in experiments concerning polarisation, and typically come as $\frac{\lambda}{4}$ or $\frac{\lambda}{2}$ waveplates. $\frac{\lambda}{4}$ waveplates can be used to convert linearly polarised light into circularly polarised light and vice versa. For the former case, the orientation of the polarisation of the incoming linearly polarised light must be ±45° relative to the fast (or slow) axis of the waveplate. If the polarisation direction is either ±90° or 0° then the polarisation of the outputted light will remain unchanged. At any other angle, the outputted polarisation will have some degree of ellipticity. For the case of $\frac{\lambda}{2}$ waveplates, these can be used to change the orientation of linearly polarised light i.e. if the incoming light has a polarisation orientated ±45° relative to the fast axis, the polarisation of the light will be rotated by ±90°. Diagonal light can be created by ensuring a relative angle between the incoming polarisation and the fast-axis of ±22.5°. $\frac{\lambda}{2}$ waveplates can also be used to change the handedness of circularly polarised light.

Creation of polarised light is useful when wanting to excite in a specific polarisation. This can be achieved by ensuring the light is initially purely polarised in a single orientation, either using a linear polariser (LP) or, for higher power excitation, a polarising beam splitter (PBS). Now, when passing through the waveplate, assuming the fast axis is orientated correctly, the outputted light will have a known polarisation of the desired orientation.

Isolation of polarised light is useful when wanting to measure emission in separate polarisations (e.g. H and V) such as when measuring the Stokes parameters. To isolate a particular polarisation from emission, which is typically light of mixed polarisation, a LP can be used after the waveplate. With the LP fixed in a specific orientation, it will block all polarisations from passing through (either through absorption, destructive interference or reflection) except the polarisation aligned with its transmission axis, essentially acting as a polarising filter. The fast axis of the waveplate can now be orientated such that it converts the light of the desired polarisation to the orientation of the LP. For example, if measuring the horizontal component of emission, the LP can be set to vertical transmission and a $\frac{\lambda}{2}$ waveplate can be used with its fast axis orientated $-45°$ from the horizontal. This ensures that all horizontally polarised emission is rotated to vertical polarisation by the waveplate and passes through the LP towards to CCD. Whereas all other polarisations in the emission, including vertical polarisation, are converted to polarisations incompatible with the LP. To isolate circularly polarised light the $\frac{\lambda}{2}$ is replaced with a $\frac{\lambda}{4}$ waveplate which will convert the circularly polarised emission to vertical to then pass through the LP. The orientation of the fast-axis of the $\frac{\lambda}{4}$ waveplate will depended on the desired handedness of the light being measured.

With the knowledge of the isolation of polarised light for measurements described in the last paragraph, the Stokes measurements of emission can be calculated. This can be done using the equations for the Stokes parameters described in subsection 1.5.1 and allows the visualisation of the spatial and momentum distribution of polarised polariton states. Isolating polarisation in emission collection is also useful in separating the TE-TM (or birefringent) split branches of polariton dispersions into separate dispersions and also for measuring the degrees of linear or circular polarisation of polariton states.

In Chapter 4 polarisation creation is used to excite single TE or TM modes on the polariton dispersion or to excite both with circular polarisation. Isolation of polarised emission is also used to calculate the Stokes parameters for propagating polaritons with Zitterbewegung in their trajectories.

2.3 Light modulation

2.3.1 Electro-optic modulator

In Chapter 5, an electro-optic modulator (EOM) is used to lessen the effects of sample heating. An EOM is a device that allows fine control over the output polarisation of light and the ability to change said polarisation at a high frequency rate. It uses two lithium niobate crystals that have an electric field dependant birefringence, or more simply, they change refractive index when they experience an electric field. This change in refractive index causes a phase shift in the light transmitting through the crystals which consequentially rotates the polarisation by ±90°. Under a constant electric field, an EOM acts the same as a $\frac{\lambda}{2}$ waveplate but when combined with a signal generator and bias controller, the electric field applied to the EOM can be pulsed over short time intervals. The leads to the outputted light having a pulsed shift in polarisation e.g. the light may be vertically polarised every 20ms for 5ms and horizontally polarised for the rest. Combining this with a PBS allows for rapid pulsed light of single polarisation from a continuous wave laser. This essentially acts to modulate the power of the laser at a high frequency rate. The beam, as experienced by the sample, will be 'on' for a given time and 'off' for the rest, thus giving it time to cool before being heated again by laser. A typical signal sent to the EOM in Chapter 5 has a pulse width of 10μs and a frequency of 10kHz, creating a beam that is horizontally polarised for 900ms for every second and vertically polarised for 100ms.

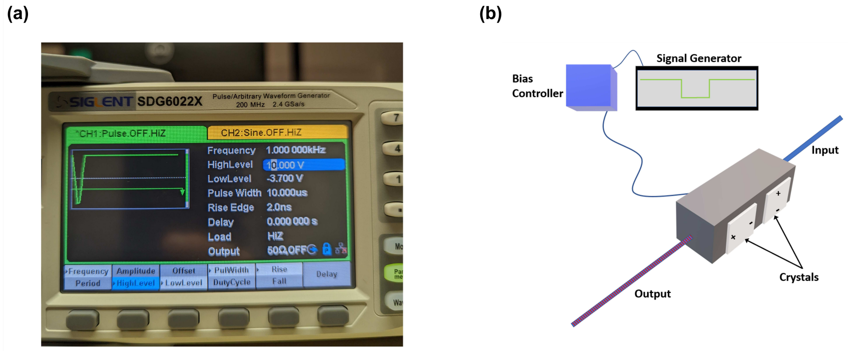

*CH1:Pulse.OFF.HiZ
CH2:Sine.OFF.HiZ
Frequency 1.000 000kHz
HighLevel 10.000 V
LowLevel -3.700 V
Pulse Width 10.000us
Rise Edge 2.0ns
Delay 0.000 000 s
Load HiZ
Output 50Ω,OFF

Figure 2.12: (a) Photograph showing the screen of the signal generator used to generate a typical pulse for experiments in Chapter 5. This is sent to the bias controller which converts the signal into a varying electric field and applies it to the EOM. (b) Labelled schematic showing the EOM set-up. Red lines denote vertical polarisation and blue denotes horizontal. This image is not to scale.

2.3.2 Spatial Light Modulation

In Chapter 5 the use of a spatial light modulator (SLM) is required to modulate the phase (and thus intensity via destructive interference) of light incident on the sample. An SLM can be used to create patterns in the spot on the sample of varying intensity, for instance, this is useful when trying to spatially match the spot to specific micropillars in a lattice array. The model used for the work in this thesis is a Holoeye PLUTO-NIR-015 phase only liquid crystal SLM. This particular SLM can be used to modulate incoming light by displaying a hologram of varying grey levels on its 1920x1080 pixel display. The hologram is generated in Matlab using the parameters provided in the SLM manual and acts as a reflective diffraction grating. The varying grey levels of the hologram correspond the different orientation of the liquid crystals in the display, the orientation being determined by the voltage applied by the SLM driver unit to each pixel. The first order diffraction beam is then guided to the excitation objective, separated from other orders by a lens and pinhole. A simple diffraction grating will create a beam with the same phase, however, a more complex hologram can contain multiple different gratings on the display with varying shapes at different positions. This will create a patterned spot or several smaller spots with individual control over the shape, intensity and phase of each spot via Matlab. Complex holograms such as those described are used in Chapter 5 to match the spot on the sample to the real space emission profile of the S and P flat bands in a 2D Lieb lattice.

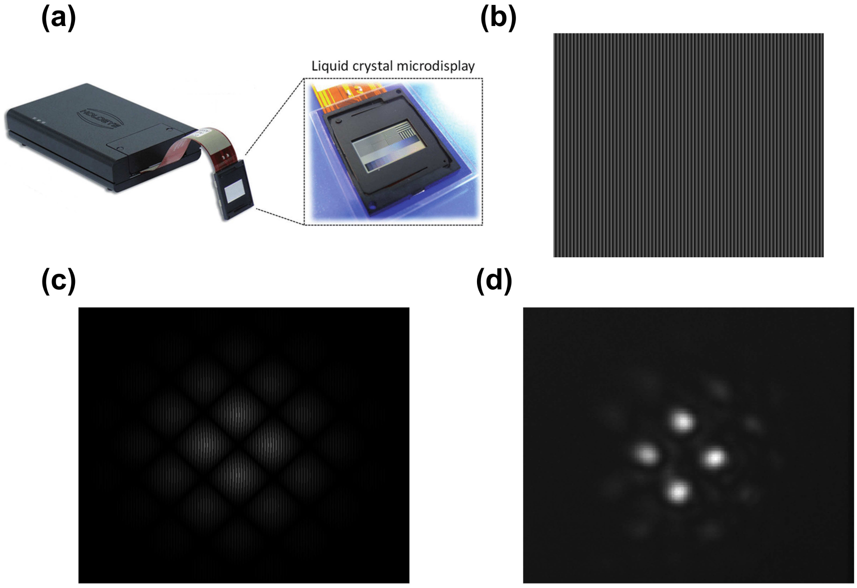

Figure 2.13: (a) Image showing the model of SLM used in the experiments in Chapter 5 (b) Diffraction grating hologram generated by Matlab and displayed on the liquid crystal display shown in (a). (c) Complex diffraction grating hologram used to generate a pattered spot on the sample. (d) Patterned spot generated by the hologram shown in (c). This spot is in free space.

Chapter 3

Exciton–polaritons in GaAs-based slab waveguide photonic crystals

3.1 Introduction

As with microcavities, the potential landscape experienced by polaritons within a waveguide can be engineered via lattice potentials. To achieve this, a photonic crystal (PhC) can be created by etching holes in to the top cladding layer of the waveguide. As with micropillar lattices, the air-semiconductor interface acts to confine the photonic modes laterally (in-plane) and results in modification of the dispersion. Since the propagation of the mode over the PhC does not require hopping as in micropillar lattices, the modification of the dispersion manifests itself differently. In the case of the waveguide dispersion, forbidden energy gaps will appear along the dispersion, tuned by the depth and size of the etching. These band-gaps represent modes that destructively interfere upon reflection from the air-semiconductor interface.

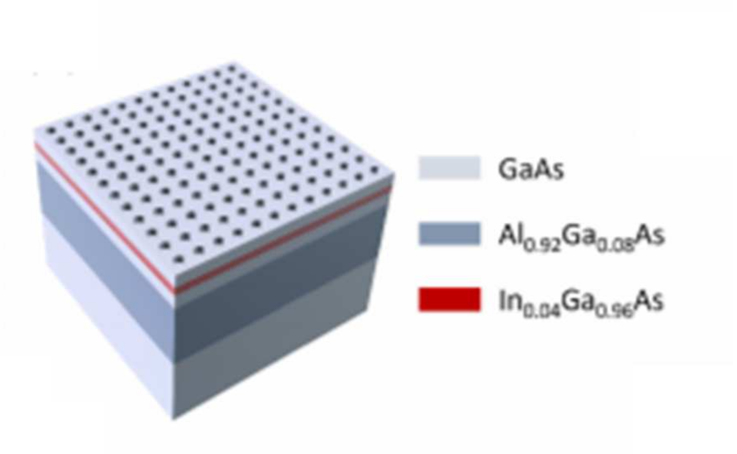

Figure 3.1: Schematic showing the structure of a slab waveguide with a PhC etched into the top GaAs cladding layer.

The work presented in the following chapter demonstrates the implementation of 2D square lattice photonic crystals in GaAs based waveguides with the presence of strong coupling between embedded QW excitons and guided photonic modes. It also demonstrates the opening of band gaps in the polariton dispersion and capitalises on the long lifetimes and large group velocity afforded to polaritons by waveguides (due to lower losses compared to microcavities) to achieve a high level of attenuation of the emission inside these band gaps. A demonstration of the tunability of the size and position of these band gaps is made along with a demonstration of the relation of these parameters to the crystal length and proximity to the exciton resonance. This work also uses an external magnetic field to induce a Zeeman splitting in the excitonic component of the polaritons and demonstrates that the subsequent blue shift of the exciton resonance can be used to tune the size of the band gaps.

The work presented in this chapter is motivated by recent proposals for the formation of topologically protected states within polaritronic systems[130, 131]. These proposals suggest that such states can be created in systems that exhibit a strong Zeeman splitting under an applied external magnetic field. The application of this magnetic field acts to break time reversal symmetry and open a non-trivial gap in the polariton dispersion inside which topologically protected states have been shown to exist[132]. A requirement for the creation of such states is that the magnitude of the Zeeman splitting is larger than the size of non-trivial band gap. Whilst this work demonstrates a level of Zeeman splitting, it is not sufficiently large to fulfil this requirement. However, this work does demonstrate the feasibility of using waveguide polaritons in PhC's as an alternative to microcavities for the opening of non-trivial band gaps. The results provide a foundation for future studies that could create topologically protected states in a similar system, potentially leading to the implementation of polariton integrated circuits.

The following work presented in this chapter was carried out by myself alongside Dr Charles Whittaker and the samples were fabricated by Dr Tommi Isoniemi. The measurements were taken by myself and Charles and the data processing was done mainly Dr Charles Whittaker.

The work presented in this chapter is done so in a paper format. Refer to Ref.[133] and its supplementary material for the version presented in this thesis.

3.2 Exciton-polaritons in GaAs-based slab waveguide photonic crystals

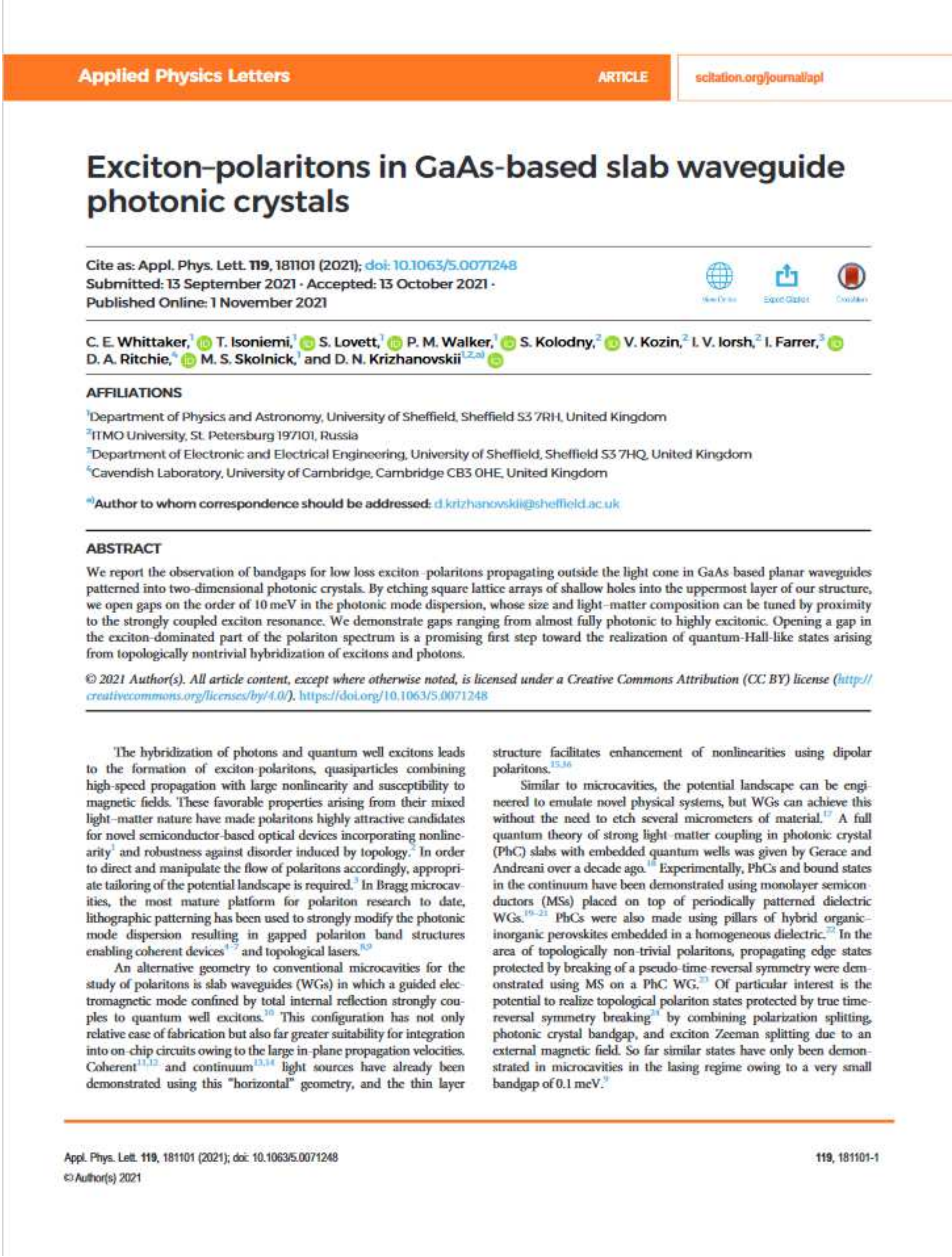

Applied Physics Letters ARTICLE scitation.org/journal/apl

Exciton-polaritons in GaAs-based slab waveguide photonic crystals

Cite as: Appl. Phys. Lett. **119**, 181101 (2021); doi: 10.1063/5.0071248
Submitted: 13 September 2021 · Accepted: 13 October 2021 ·
Published Online: 1 November 2021

C. E. Whittaker,[1] T. Isoniemi,[1] S. Lovett,[1] P. M. Walker,[1] S. Kolodny,[2] V. Kozin,[2] I. V. Iorsh,[2] I. Farrer,[3] D. A. Ritchie,[4] M. S. Skolnick,[1] and D. N. Krizhanovskii[1,2,a)]

AFFILIATIONS

[1]Department of Physics and Astronomy, University of Sheffield, Sheffield S3 7RH, United Kingdom
[2]ITMO University, St. Petersburg 197101, Russia
[3]Department of Electronic and Electrical Engineering, University of Sheffield, Sheffield S3 7HQ, United Kingdom
[4]Cavendish Laboratory, University of Cambridge, Cambridge CB3 0HE, United Kingdom

[a)]**Author to whom correspondence should be addressed:** d.krizhanovskii@sheffield.ac.uk

ABSTRACT

We report the observation of bandgaps for low loss exciton-polaritons propagating outside the light cone in GaAs based planar waveguides patterned into two-dimensional photonic crystals. By etching square lattice arrays of shallow holes into the uppermost layer of our structure, we open gaps on the order of 10 meV in the photonic mode dispersion, whose size and light–matter composition can be tuned by proximity to the strongly coupled exciton resonance. We demonstrate gaps ranging from almost fully photonic to highly excitonic. Opening a gap in the exciton-dominated part of the polariton spectrum is a promising first step toward the realization of quantum-Hall-like states arising from topologically nontrivial hybridization of excitons and photons.

The hybridization of photons and quantum well excitons leads to the formation of exciton-polaritons, quasiparticles combining high-speed propagation with large nonlinearity and susceptibility to magnetic fields. These favorable properties arising from their mixed light–matter nature have made polaritons highly attractive candidates for novel semiconductor-based optical devices incorporating nonlinearity[1] and robustness against disorder induced by topology.[2] In order to direct and manipulate the flow of polaritons accordingly, appropriate tailoring of the potential landscape is required.[3] In Bragg microcavities, the most mature platform for polariton research to date, lithographic patterning has been used to strongly modify the photonic mode dispersion resulting in gapped polariton band structures enabling coherent devices[4–7] and topological lasers.[8,9]

An alternative geometry to conventional microcavities for the study of polaritons is slab waveguides (WGs) in which a guided electromagnetic mode confined by total internal reflection strongly couples to quantum well excitons.[10] This configuration has not only relative ease of fabrication but also far greater suitability for integration into on-chip circuits owing to the large in-plane propagation velocities. Coherent[11,12] and continuum[13,14] light sources have already been demonstrated using this "horizontal" geometry, and the thin layer structure facilitates enhancement of nonlinearities using dipolar polaritons.[15,16]

Similar to microcavities, the potential landscape can be engineered to emulate novel physical systems, but WGs can achieve this without the need to etch several micrometers of material.[17] A full quantum theory of strong light-matter coupling in photonic crystal (PhC) slabs with embedded quantum wells was given by Gerace and Andreani over a decade ago.[18] Experimentally, PhCs and bound states in the continuum have been demonstrated using monolayer semiconductors (MSs) placed on top of periodically patterned dielectric WGs.[19–21] PhCs were also made using pillars of hybrid organic–inorganic perovskites embedded in a homogeneous dielectric.[22] In the area of topologically non-trivial polaritons, propagating edge states protected by breaking of a pseudo-time-reversal symmetry were demonstrated using MS on a PhC WG.[23] Of particular interest is the potential to realize topological polariton states protected by true time-reversal symmetry breaking[24] by combining polarization splitting, photonic crystal bandgap, and exciton Zeeman splitting due to an external magnetic field. So far similar states have only been demonstrated in microcavities in the lasing regime owing to a very small bandgap of 0.1 meV.[9]

While modulated band structure is one key ingredient for future applications, it is equally important to achieve long polariton lifetimes and propagation distances. In MS and organics, the lifetimes are short, which may occur due to inhomogeneous broadening of the exciton linewidth up to ~10 meV. The longest reported polariton lifetimes are achieved in GaAs-based structures[25] where, owing to the high quality quantum wells, polariton linewidths can be 10–100 times smaller. Furthermore, a crucial feature of previous works is that the studied states are near zero in-plane momentum where coupling to freely propagating waves in the surroundings inevitably leads to high photonic losses. For example, in Dang *et al.*[22] even the simulated linewidth for passive materials is of order 16 meV suggesting only a 40 fs photon lifetime. To achieve long polariton lifetime, it is critical that states are produced at high wavenumbers where total internal reflection (TIR) prevents radiative loss. For GaAs-based WGs, lifetimes (propagation lengths) on the order of 10 ps (500 μm) can be expected.[10,13] Until now, however, strong band structure modulation was not demonstrated in GaAs-based polariton WGs, and polariton PhC states protected by TIR have not so far been demonstrated in any material system. Achieving the former is challenging since it relies on etching through a significant fraction of the core. However, etching through or too near the quantum wells leads to high losses associated with surface recombination effects. While previous works[17] have demonstrated the persistence of strong coupling in patterned GaAs-based WGs, the modulated region was spatially separated from the WG core leading to only a weak perturbation and no opening of a gap.

In this work, we implement two-dimensional square lattice PhCs in GaAs-based WGs in the strong coupling regime. We achieve PhC bandgaps near the Brillouin zone (BZ) edge where the states are protected by TIR and show low loss propagation over the ~50 μm wide PhC for states outside the gap. The bandgap, with a width of ~10 meV (roughly an order of magnitude larger than in microcavity lattices[2,3]) is the signature of the polariton band structure being strongly modulated by the periodic lattice. Finally, we demonstrate one of the useful features of polariton-based platforms by exploiting the excitonic content of the states to tune the gap width using an external magnetic field.

The sample, illustrated in Fig. 1(a), is a planar WG into which holes are etched to form a square lattice PhC. The GaAs WG core layer has a total thickness of 295 nm and contains three 10 nm wide $In_{0.06}Ga_{0.94}As$ quantum wells (QWs) separated by 10 nm GaAs barriers and placed at the peak of the transverse-electric (TE) polarized field in order to maximize the Rabi coupling. The upper quantum well is 137 nm below the surface, which allows etch depths up to 87 nm (~30% of the core thickness) while still leaving 50 nm GaAs cap to protect the wells. The core is separated from the GaAs substrate by a 750 nm thick AlGaAs cladding layer with 90% average Al composition. An extended discussion of the design of the layer structure is given in the supplementary material.

The samples were grown by MBE and then patterned with a soft mask using electron beam lithography to form PhCs with a square lattice geometry, as shown in Figs. 1(a) and 1(b). The patterns were etched down into the planar structure using inductively coupled plasma etching with a chlorine/argon chemistry. Several samples were fabricated, with lattice constants *a* between 120 and 130 nm, hole etch depths *h* between 55 and 64 nm and hole diameters *d* between 47 and 66 nm. The ranges for fabrication were selected by calculating the PhC band structure using Lumerical® FDTD solutions finite difference time domain software (see the supplementary material for further details). Figure 1(c) shows an example of the simulated band structure for photons (without coupling to the exciton) across the whole Brillouin zone (BZ). The polarization of states in slab photonic crystals may be classified as TE-like or TM-like, with an electric field mostly in or out of the WG plane, respectively.[26] Only the TE-like modes couple strongly to the excitons in our QWs. The bands for both polarizations are shown in Fig. 1(c). No narrow linewidth states could be identified above the light cone (in the shaded region) or above the GaAs bandgap (1.519 eV) since such states are either not guided or strongly

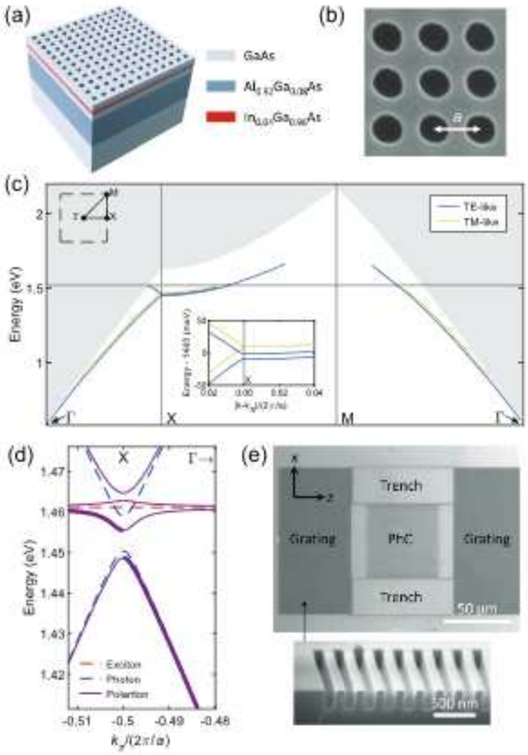

FIG. 1. (a) Schematic of the photonic crystal (PhC) structure in a slab waveguide. (b) Scanning electron microscope (SEM) image of holes etched into the surface of the waveguide showing the center-to-center distance a. (c) Bandstructure of the photon modes of a PhC with $a = 126$ nm, $d = 47$ nm, $h = 64$ nm. The horizontal axis follows the triangular path Γ-X-M-Γ indicated on the inset schematic of the first BZ (top left). Vertical lines indicate the X and M points. Horizontal line indicates the GaAs bandgap. Central inset is a zoom of the region around the X point. (d) Calculated polariton dispersion relation in the vicinity of the X point ($k_y/(2\pi/a) = -0.5$) for the PhC in (c). The thick lines correspond to the states, which are visible in Fig. 2. (e) Optical microscope image of a PhC with grating couplers allowing light to be coupled in and out along the *z* direction and with etched trenches. The inset shows an angled SEM image of a cleaved etched grating.

absorbed, respectively. In Fig. 1(c), the modes get broader with increasing energy above the bandgap and we choose to plot the dispersion of the modes, which have linewidth < 100 meV. There is a ~10 meV gap in the TE like states around the X point, which we will examine in more detail momentarily. From X toward M, the bands increase in frequency so that the bandgap does not span all momentum states but exists only for modes propagating near X. A larger gap could be engineered by using a different lattice geometry, such as honeycomb,[24] but even this small gap serves to illustrate that polariton band structure can be modulated by many times the linewidth and could support edge states where the bulk 2D lattice provides other desirable properties, such as topological protection.[24]

The band structure was calculated for a range of a, d, and h, and close-to-optimal values were selected for fabrication such that the gap in the TE like modes at the X point is near the exciton energy and so that the gap width was maximized without etching too close to the QWs. In experiment, we will observe polariton rather than pure photon bands. Figure 1(d) shows an example of the calculated polariton dispersion resulting from strong coupling between the TE like mode and QW excitons, focusing on the region around the X point. The polariton bandgap can be seen clearly. To enable us to experimentally study gap formation within the PhCs, grating couplers were fabricated on either side of the PhC in the z direction [Fig. 1(c)]. These fold the waveguide modes into the radiative region allowing light to be coupled in and out. On the other two sides of the PhC, trenches were etched (through the active region) for prospective studies of edge states, although we note that this is an entirely optional design feature. The side length of the PhCs corresponds to ~400 periods.

For optical measurements, the sample was held at low temperatures (<8 K) and excited by a cw laser at 637 nm focused to a ~3 μm spot on the PhC surface. This nonresonant excitation incoherently populates the polariton modes of the PhC WGs (which lie below the light cone) by multiple relaxation processes. The polaritons may then propagate out of the PhC to the grating where they are scattered out and recorded using a spectrometer. Spatial filtering optics were used to collect the emission from selected regions on the sample.

In Fig. 2(a), we show typical examples of the emission collected from gratings adjacent to the PhCs, measured for a single set of devices and corresponding to a cut through the X point, along the Γ-X-Γ direction in momentum space. The heavy attenuation of PL intensity within particular energy windows directly results from the presence of bandgaps in the PhC slabs. Polaritons at energies in the gaps cannot propagate out of the PhC to be detected at the grating. We stress that these gaps arise from the periodic potential created by the PhCs and are qualitatively very different to the resonances induced by backreflection of guided modes between pairs of gratings in Ref. 12. We see that as the PhC period a is made successively smaller, the gap (shown by the double-sided vertical arrow) moves upward in energy, becoming smaller as it approaches the exciton resonance (dashed white line). The reduction in the gap size arises from reduction in the photonic fraction as the gap approaches the exciton resonance, confirming that the strong coupling is retained in the PhC region. This can also be seen from the anticrossing behavior of the bandgap edges in Fig. 2(b), which also includes results from devices with different hole profiles. This is in contrast to our simulations of the purely photonic structure (without strong coupling to an exciton) in which the gap size varies little across this range of periods. Since the normal mode (Rabi) splitting between the photonic and excitonic resonances is known, we can calculate the exciton fraction of each gap using

$$|X|^2 = \frac{1}{2}\left[1 + \frac{E_G^{ph} - E_X}{\sqrt{(E_G^{ph} - E_X)^2 + \hbar\Omega^2}}\right], \tag{1}$$

where E_G^{ph} is the central gap energy of the bare photonic gap, calculated using $E_G^{ph} = \Omega^2/4(E_X - E_G^{pol}) + E_G^{pol}$, where E_G^{pol} is the central gap energy of the lower polariton branch. In the data shown in Fig. 2, the gap passes from almost fully photonic ($|X|^2 = 1\%$) to predominantly excitonic ($|X|^2 = 61\%$), as can be seen from Fig. 2(c). In other devices, we have measured gaps with exciton fractions as high as 73%. We note that emission from states within ~1.5 meV below the exciton line is heavily attenuated due to absorption, which, along with the

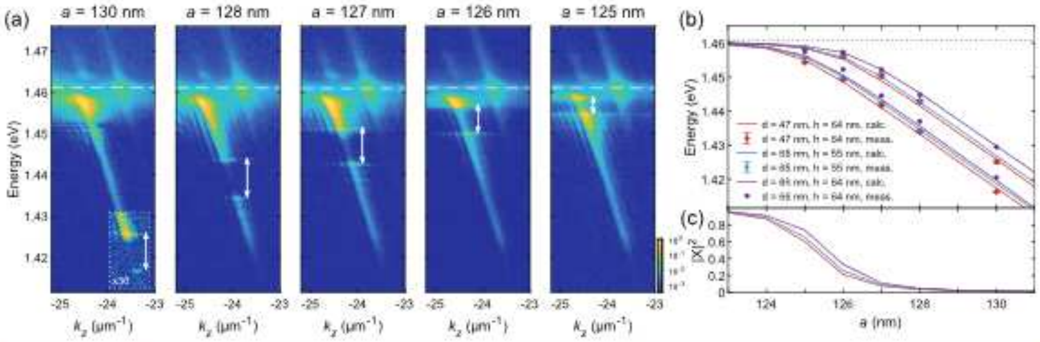

FIG. 2. (a) Angle-resolved photoluminescence spectra corresponding to PhCs with different periodicities. The devices have holes with diameter d = 47 nm and etch depth h = 64 nm. (b) Measured and calculated positions of gaps (upper and lower band edges) against PhC period for devices with different hole profiles (different diameters d and etch depths h). The calculated positions are given by taking the gaps from photonic simulations and assuming a Rabi splitting of 9 meV with the exciton resonance. The error bars on the measured data points represent the standard deviation from measurements of different devices with the same hole profiles. (c) Exciton fraction at the center of the gap vs periodicity for hole profiles corresponding to the solid curves in panel (b).

broadened polariton linewidths, places an upper bound on the exciton fraction of gaps, which can be observed in our current samples. This may be improved somewhat by reducing the exciton inhomogeneous linewidth and/or increasing the Rabi splitting to increase $|X|^2$ for polariton states further from the highly absorbing part of the exciton tail. We also note that within the gaps some weak emission is visible, implying that the reflectivity is below unity, which arises from the finite extent of the PhCs. As we show in Fig. 3, the extinction within the gap depends strongly on the length of photonic crystal (i.e., number of lattice periods) between the excitation spot and the edge of the PhC. Increasing the number of periods strongly increases the attenuation for energies in the gap. This is clear evidence that the observed gaps are due to reflection of propagating polaritons from the periodic PhC structure. We further note that outside the bandgap, there is little observable dependence on excitation spot distance. This demonstrates that the decay length of freely propagating polaritons in the photonic crystal (but outside the gap) is much larger than the 35 μm length over which the spot was moved. This is consistent with the $\sim$500 μm lengths in unpatterned polariton waveguides.[10,13]

In contrast to our system, the primary gaps studied in periodic potentials in Bragg microcavities are typically formed in the photonic part of the spectrum and, thus, have far smaller exciton fractions, which severely limits the ability to tune the gap position using external fields. If the exciton content is large, however, one may employ diverse methods to tune the energy of the gap, including temperature, optical excitation, and electric and magnetic fields.[27] In order to demonstrate the feasibility of tuning gaps in our devices, and also to show unambiguously that they are polaritonic in nature, we placed our sample in a magnetic field in Faraday geometry. The results are summarized in Fig. 4. The predominant effect is the diamagnetic (blue)shift of the exciton resonance, which reduces the exciton fraction of the gaps and, hence, increases their size. For the PhC with $a = 125$ nm, the gap size can be increased from 4.0 meV at B = 0 T to 5.4 meV at B = +9 T [Figs. 4(a)–4(c)]. In the case of the PhC with $a = 124$ nm, the full gap is not visible at B = 0 T, since the upper gap energy lies in the heavily attenuated region below the exciton resonance. At higher magnetic fields, however, the gap becomes visible, reaching a size of 2.4 meV at B = +9 T [Figs. 4(d)–4(f)]. We, thus, demonstrate that the polariton band structure can be tuned by varying the exciton content using a magnetic field. It should be noted that to obtain the larger gap sizes requires reducing the exciton content [see Fig. 2(c)], which will also reduce the polariton nonlinear interaction strength. The tuning can be used as a lever to strike an optimal balance between these properties.

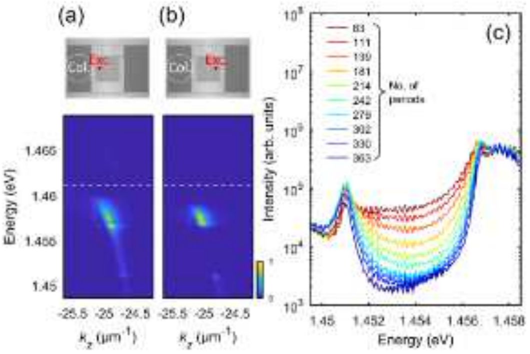

FIG. 3. Measured angle-resolved PL spectra when the excitation spot (Exc.) is at the near (a) and far (b) edges of the PhC ($a = 126$ nm) with respect to the grating from which light is collected (Col.). (c) PL spectra measured for different excitation positions (i.e., number of PhC periods between the excitation and detection spots).

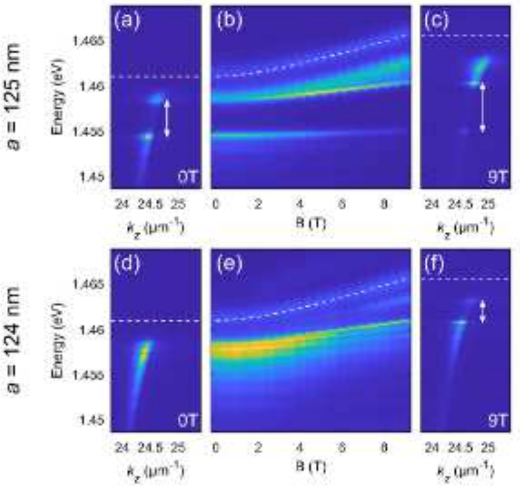

FIG. 4. (a)–(c) Magnetic field dependence of spectra for PhC with $a = 125$ nm. The angle-resolved spectra measured at 0 and 9 T are shown in (a) and (c), respectively, and contour plots of the angle-integrated spectrum are shown in (b). (d)–(f) Same as (a)–(c) for PhC with $a = 124$ nm. The color scale is the same as that of Fig. 3.

For finite magnetic fields, there is also a Zeeman splitting of the exciton, which reaches values exceeding 0.5 meV at the highest fields. Thus, the basic ingredients we have presented, namely, gaps in the excitonic part of the spectrum and an exciton Zeeman splitting are those described in Ref. 24 as the criteria for quantum Hall type (chiral) edge states at the boundaries of the system. However, for true topological protection, one needs the Zeeman splitting to exceed the size of the gap; this will require an enhancement of the exciton g factor, which in our system could be achieved by varying the In composition or width of the quantum wells.[28] Alternatively one may think about employing semimagnetic quantum wells in a Te-based system[29] or using transition metal dichalcogenides where spin dependent strong coupling to a photonic mode can create a giant effective Zeeman splitting exceeding 10 meV.[30] We note that even without a global bandgap, the system may support topological edge states with well defined momentum close to the X point. Losses due to scattering into bulk modes can be minimized by maximizing the gap size using other lattice geometries, such as hexagonal.[24]

In summary, we have presented a platform to study strongly modulated exciton polariton band structures using patterned slab waveguides in the strong coupling regime. We observe low loss propagating states outside the light cone and bandgaps of order 10 meV.

We have demonstrated that the gaps can be controlled both through the photonic component (varying the period of the crystal) or the excitonic component (external magnetic field). For future studies, we envisage the patterning of photonic crystals with different lattice geometries featuring exotic dispersion relations,[31,32] as well as interfacing waveguides with other excitonic materials, such as atomically thin semiconductors[21] and organic polymers.[33] Our system could, thus, offer a flexible and promising alternative to microcavity-based polariton lattices for the study of topological states and implementation of optoelectronic devices.

See the supplementary material for further details of the PhC structure and simulations used in the design process.

This work was supported by UK EPSRC under Grant Nos. EP/N031776/1 and EP/R04385X/1 and by the Russian Science Foundation (Project No. 19-72-20120).

AUTHOR DECLARATIONS

Conflict of Interest

The authors declare that there are no conflicts of interest.

DATA AVAILABILITY

The data that support the findings of this study are available from the corresponding author upon reasonable request.

REFERENCES

[1] D. Sanvitto and S. Kéna-Cohen, "The road towards polaritonic devices," Nat. Mater. **15**, 1061–1073 (2016).
[2] A. Amo and J. Bloch, "Exciton-polaritons in lattices: A non-linear photonic simulator," C. R. Phys. **17**, 934–945 (2016).
[3] C. Schneider, K. Winkler, M. D. Fraser, M. Kamp, Y. Yamamoto, E. A. Ostrovskaya, and S. Höfling, "Exciton polariton trapping and potential landscape engineering," Rep. Prog. Phys. **80**, 016503 (2017).
[4] E. Wertz, A. Amo, D. D. Solnyshkov, L. Ferrier, T. C. H. Liew, D. Sanvitto, P. Senellart, I. Sagnes, A. Lemaitre, A. V. Kavokin, G. Malpuech, and J. Bloch, "Propagation and amplification dynamics of 1D polariton condensates," Phys. Rev. Lett. **109**, 216404 (2012).
[5] H. S. Nguyen, D. Vishnevsky, C. Sturm, D. Tanese, D. Solnyshkov, E. Galopin, A. Lemaître, I. Sagnes, A. Amo, G. Malpuech, and J. Bloch, "Realization of a double-barrier resonant tunneling diode for cavity polaritons," Phys. Rev. Lett. **110**, 236601 (2013).
[6] C. Sturm, D. Tanese, H. S. Nguyen, H. Flayac, E. Galopin, A. Lemaître, I. Sagnes, D. Solnyshkov, A. Amo, G. Malpuech, and J. Bloch, "All optical phase modulation in a cavity-polariton mach–zehnder interferometer," Nat. Commun. **5**, 3278 (2014).
[7] F. Marsault, H. S. Nguyen, D. Tanese, A. Lemaitre, E. Galopin, I. Sagnes, A. Amo, and J. Bloch, "Realization of an all optical exciton-polariton router," Appl. Phys. Lett. **107**, 201115 (2015).
[8] P. St-Jean, V. Goblot, E. Galopin, A. Lemaître, T. Ozawa, L. L. Gratiet, I. Sagnes, J. Bloch, and A. Amo, "Lasing in topological edge states of a one-dimensional lattice," Nat. Photonics **11**, 651–656 (2017).
[9] S. Klembt, T. H. Harder, O. A. Egorov, K. Winkler, R. Ge, M. A. Bandres, M. Emmerling, L. Worschech, T. C. H. Liew, M. Segev, C. Schneider, and S. Höfling, "Exciton polariton topological insulator," Nature **562**, 552–556 (2018).
[10] P. M. Walker, L. Tinkler, M. Durska, D. M. Whittaker, I. J. Luxmoore, B. Royall, D. N. Krizhanovskii, M. S. Skolnick, I. Farrer, and D. A. Ritchie, "Exciton polaritons in semiconductor waveguides," Appl. Phys. Lett. **102**, 012109 (2013).
[11] O. Jamadi, F. Reveret, P. Disseix, F. Medard, J. Leymarie, A. Moreau, D. Solnyshkov, C. Deparis, M. Leroux, E. Cambril, S. Bouchoule, J. Zuniga-Perez, and G. Malpuech, "Edge-emitting polariton laser and amplifier based on a zno waveguide," Light: Sci. Appl. **7**, 82 (2018).
[12] D. G. Suárez-Forero, F. Riminucci, V. Ardizzone, M. D. Giorgi, L. Dominici, F. Todisco, G. Lerario, L. N. Pfeiffer, G. Gigli, D. Ballarini, and D. Sanvitto, "Electrically controlled waveguide polariton laser," Optica **7**, 1579–1586 (2020).
[13] P. M. Walker, C. E. Whittaker, D. V. Skryabin, E. Cancellieri, B. Royall, M. Sich, I. Farrer, D. A. Ritchie, M. S. Skolnick, and D. N. Krizhanovskii, "Spatiotemporal continuum generation in polariton waveguides," Light: Sci. Appl. **8**, 6 (2019).
[14] D. M. D. Paola, P. M. Walker, R. P. A. Emmanuele, A. V. Yulin, J. Ciers, Z. Zaidi, J. F. Carlin, N. Grandjean, I. Shelykh, M. S. Skolnick, R. Butté, and D. N. Krizhanovskii, "Ultrafast nonlinear ultraviolet pulse modulation in an AlInGaN polariton waveguide operating up to room temperature," Nat. Commun. **12**, 3504 (2021).
[15] I. Rosenberg, D. Liran, Y. Mazuz-Harpaz, K. West, L. Pfeiffer, and R. Rapaport, "Strongly interacting dipolar-polaritons," Sci. Adv. **4**, eaat8880 (2018).
[16] D. Suárez-Forero, F. Riminucci, V. Ardizzone, N. Karpowicz, E. Maggiolini, G. Macorini, G. Lerario, F. Todisco, M. D. Giorgi, L. Dominici, D. Ballarini, G. Gigli, A. Lanotte, K. West, K. Baldwin, L. Pfeiffer, and D. Sanvitto, "Enhancement of parametric effects in polariton waveguides induced by dipolar interactions," Phys. Rev. Lett. **126**, 137401 (2021).
[17] D. Bajoni, D. Gerace, M. Galli, J. Bloch, R. Braive, I. Sagnes, A. Miard, A. Lemaître, M. Patrini, and L. C. Andreani, "Exciton polaritons in two-dimensional photonic crystals," Phys. Rev. B **80**, 201308 (2009).
[18] D. Gerace and L. C. Andreani, "Quantum theory of exciton-photon coupling in photonic crystal slabs with embedded quantum wells," Phys. Rev. B **75**, 235325 (2007).
[19] L. Zhang, R. Gogna, W. Burg, E. Tutuc, and H. Deng, "Photonic-crystal exciton-polaritons in monolayer semiconductors," Nat. Commun. **9**, 713 (2018).
[20] Y. Chen, S. Miao, T. Wang, D. Zhong, A. Saxena, C. Chow, J. Whitehead, D. Gerace, X. Xu, S.-F. Shi, and A. Majumdar, "Metasurface integrated monolayer exciton polariton," Nano Lett. **20**, 5292–5300 (2020).
[21] V. Kravtsov, E. Khestanova, F. A. Benimetskiy, T. Ivanova, A. K. Samusev, I. S. Sinev, D. Pidgayko, A. M. Mozharov, I. S. Mukhin, M. S. Lozhkin, Y. V. Kapitonov, A. S. Brichkin, V. D. Kulakovskii, I. A. Shelykh, A. I. Tartakovskii, P. M. Walker, M. S. Skolnick, D. N. Krizhanovskii, and I. V. Iorsh, "Nonlinear polaritons in a monolayer semiconductor coupled to optical bound states in the continuum," Light: Sci. Appl. **9**, 56 (2020).
[22] N. H. M. Dang, D. Gerace, E. Drouard, G. Trippé-Allard, F. Lédée, R. Mazurczyk, E. Deleporte, C. Seassal, and H. S. Nguyen, "Tailoring dispersion of room-temperature exciton-polaritons with perovskite-based subwavelength metasurfaces," Nano Lett. **20**, 2113–2119 (2020).
[23] W. Liu, Z. Ji, Y. Wang, G. Modi, M. Hwang, B. Zheng, V. J. Sorger, A. Pan, and R. Agarwal, "Generation of helical topological exciton-polaritons," Science **370**, 600–604 (2020).
[24] T. Karzig, C.-E. Bardyn, N. H. Lindner, and G. Refael, "Topological polaritons," Phys. Rev. X **5**, 031001 (2015).
[25] Y. Sun, P. Wen, Y. Yoon, G. Liu, M. Steger, L. N. Pfeiffer, K. West, D. W. Snoke, and K. A. Nelson, "Bose-Einstein condensation of long-lifetime polaritons in thermal equilibrium," Phys. Rev. Lett. **118**, 016602 (2017).
[26] J. D. Joannopoulos, S. G. Johnson, J. N. Winn, and R. D. Meade, *Photonic Crystals: Molding the Flow of Light*, 2nd ed. (Princeton University Press, Princeton, NJ, 2008).
[27] A. Rahimi-Iman, "Polaritons in external fields," in *Polariton Physics: From Dynamic Bose–Einstein Condensates in Strongly-Coupled Light–Matter Systems to Polariton Lasers* (Springer International Publishing, Cham, 2020), pp. 241–262.
[28] N. J. Traynor, R. T. Harley, and R. J. Warburton, "Zeeman splitting and g factor of heavy-hole excitons in In$_x$Ga$_{1-x}$As/GaAs quantum wells," Phys. Rev. B **51**, 7361–7364 (1995).
[29] R. Mirek, M. Król, K. Lekenta, J.-G. Rousset, M. Nawrocki, M. Kulczykowski, M. Matuszewski, J. Szczytko, W. Pacuski, and B. Piętka, "Angular dependence of giant Zeeman effect for semimagnetic cavity polaritons," Phys. Rev. B **95**, 085429 (2017).

[50] T. P. Lyons, D. J. Gillard, C. Leblanc, J. Puebla, D. D. Solnyshkov, L. Klompmaker, I. A. Akimov, C. Louca, P. Muduli, A. Genco, M. Bayer, Y. Otani, G. Malpuech, and A. I. Tartakovskii, "Giant effective Zeeman splitting in a monolayer semiconductor realized by spin-selective strong light-matter coupling," arXiv:2109.05859 (2021).

[51] T. Jacqmin, I. Carusotto, I. Sagnes, M. Abbarchi, D. D. Solnyshkov, G. Malpuech, E. Galopin, A. Lemaître, J. Bloch, and A. Amo, "Direct observation of Dirac cones and a flatband in a honeycomb lattice for polaritons," Phys. Rev. Lett. **112**, 116402 (2014).

[52] C. E. Whittaker, E. Cancellieri, P. M. Walker, D. R. Gulevich, H. Schomerus, D. Vaitiekus, B. Royall, D. M. Whittaker, E. Clarke, I. V. Iorsh, I. A. Shelykh, M. S. Skolnick, and D. N. Krizhanovskii, "Exciton polaritons in a two-dimensional Lieb lattice with spin-orbit coupling," Phys. Rev. Lett. **120**, 097401 (2018).

[53] R. Jayaprakash, C. E. Whittaker, K. Georgiou, O. S. Game, K. E. McGhee, D. M. Coles, and D. G. Lidzey, "Two-dimensional organic-exciton polariton lattice fabricated using laser patterning," ACS Photonics **7**, 2273–2281 (2020).

Supplementary Material : Exciton-polaritons in GaAs-based slab waveguide photonic crystals

C. E. Whittaker,[1] T. Isoniemi,[1] S. Lovett,[1] P. M. Walker,[1] S. Kolodny,[2] V. Kozin,[2] I. V. Iorsh,[2] I. Farrer,[3] D. A. Ritchie,[4] M. S. Skolnick,[1] and D. N. Krizhanovskii[1, 2]
[1]*Department of Physics and Astronomy, University of Sheffield, Sheffield S3 7RH, United Kingdom*
[2]*ITMO University, St. Petersburg 197101, Russia*
[3]*Department of Electronic and Electrical Engineering, University of Sheffield, S3 7HQ United Kingdom*
[4]*Cavendish Laboratory, University of Cambridge, CB3 0HE Cambridge, UK*

(Dated: 11 October 2021)

I. DETAILS OF SAMPLE OPTIMISATION BY NUMERICAL SIMULATIONS

Calculation of slab photonic crystal states requires a computationally intensive three-dimensional solution of Maxwell's equations, which becomes impractical when structures must be optimised over many degrees of freedom. For this reason the structure was designed in two stages. The layer thicknesses of the planar (unpatterned) structure were first designed using a high speed planar waveguide solver (CAMFR[1]). Then the photonic crystal hole diameter and etch depth were optimised using a full 3D FDTD calculation (using the commerical Lumerical FDTD package). The two step procedure works well since the first step provides coarse tuning of the energy-wavenumber dispersion while, as will be shown later, the photonic crystal period can be chosen to place the band gap center at any desired frequency along that dispersion, and the hole diameter and etch depth allow fine-tuning of the gap size.

A. Design of planar layer structure

The planar layer structure was designed to balance several competing requirements. The most important parameter is the thickness of the waveguide core. We refer the reader to ref.[3] for general design principles. For a waveguide with a thick core compared to the wavelength the effective refractive index $n_{\rm eff}$ of the fundamental mode is close to the refractive index of the core material $n_{\rm core}$. As the thickness is reduced $n_{\rm eff}$ approaches the cladding index $n_{\rm clad}$ at which point total internal reflection is lost - a situation known as cutoff. This places a lower bound on the core thickness for a desired operating wavelength and cladding material. Furthermore, in polariton structures the etch for the photonic crystal holes must stop sufficiently far above the QWs to avoid plasma-induced damage or surface states which lead to high non-radiative recombination. The holes must be deep enough to sufficiently perturb $n_{\rm eff}$ to produce a photonic band gap. This necessitates a relatively thick core to accommodate both the holes and quantum wells. On the other hand, for very thick core layers the Rabi coupling is decreased since the optical mode has less overlap with the quantum wells. In addition, a large thickness can be detrimental to the band gap width[4] since higher order waveguide modes with a similar $n_{\rm eff}$ (and hence a similar energy for a given wavevector) become allowed.

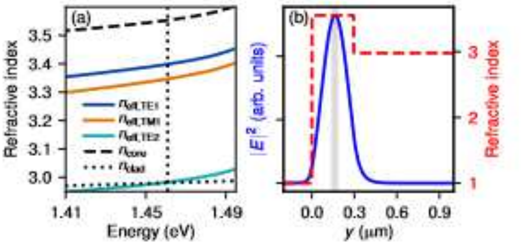

FIG. S1. (a) Calculated effective refractive indexes of the uncoupled photon modes of the unpatterned planar waveguide. Core and cladding material indexes $n_{\rm core}$ and $n_{\rm clad}$ were obtained from ref.[2] for a temperature of 4 Kelvin. Vertical dotted line indicates the exciton energy. (b) Refractive index profile (dashed curve, right hand axis) and electric field intensity of the fundamental mode versus distance from sample surface. The profiles were calculated for photons at the same frequency as the exciton, indicated by the vertical dotted line in panel (a). At this frequency the in-plane wavenumber is $25.17\,\mu\text{m}^{-1} = 1.010 \times \pi/126$ nm.
Grey shaded region indicates the region occupied by quantum wells.

The layer structure comprises a GaAs core containing three 10 nm wide $\text{In}_{0.06}\text{Ga}_{0.94}\text{As}$ quantum wells (QWs) separated by 10 nm GaAs barriers. The core is separated from the GaAs substrate by an AlGaAs cladding layer. We chose a core thickness of 295 nm, just thin enough to minimize multi-mode effects. Fig. S1(a) shows the calculated $n_{\rm eff}$ for the first few modes of the planar waveguide. The first order modes TE1 and TM1 (polarized with electric and magnetic fields parallel to the plane respectively) are well above the cutoff at $n_{\rm clad}$ while the second order modes TE2 and TM2 (not shown) are close to or below cutoff. Fig. S1(b) shows the fundamental (TE1) field profile in the growth direction alongside the refractive index profile (note that TM1 does not couple strongly to the heavy-hole excitons[5] in our QWs). The field is well localized in the core region. The quantum wells (grey shaded region) were placed at the peak of the field in order to maximize the Rabi coupling. This puts the upper quantum well 137 nm below the surface, which is sufficient to allow etch depths up to 87 nm (~30% of the core thickness) while still leaving 50 nm GaAs cap to protect the wells. The cladding consists of 10 x 75 nm $\text{Al}_{0.92}\text{Ga}_{0.08}\text{As}$ layers each separated by 0.5 monolayers of GaAs to reduce buildup of interface roughness. The alloy composition was chosen to maximize the contrast $n_{\rm clad}$ to

n_{core} while avoiding high oxidation rates associated with pure AlAs. The cladding thickness of 750 nm was chosen to minimize losses into the substrate via evanescent coupling. The simulations show that the field decays by a factor of $\sim 10^{-4}$ over this distance.

B. Optimisation of the PhC period and hole size

To avoid the need to fabricate too large a number of different structures an initial estimate of the optimal PhC period, hole diameter and etch depth was obtained using numerical simulations. Fabricating devices with a small range of parameters around this point allowed us to experimentally find PhCs with the desired properties, as presented in the main text.

The photonic band structure was simulated by the three-dimensional finite-difference time-domain (FDTD) method using the commercial Lumerical FDTD package. Frequency dependence of the material refractive indexes was included using the Lumerical multi-coefficient model fit. For the purposes of optimising the photonic gap the quantum well exciton resonance was not included in the model since only the uncoupled photon modes were required. In the y direction, perpendicular to the PhC plane (please refer to Fig. 1(c) in the main text for coordinate axes), perfectly matched layer (PML) boundary conditions were used to simulate an infinitely extended vacuum above the sample and an infinitely extended GaAs substrate. The latter is a good approximation since in the real device the unpolished back side of the substrate prevents any reflections. In the x-z plane a single unit cell of the PhC was defined and Bloch periodic boundary conditions were specified. This simulates and infinitely periodic structure in the plane. Simulations were run for each Bloch wavevector of interest to build up the bandstructure.

The system was excited by 10 randomly positioned point dipole sources with temporal duration 2.5 femtoseconds corresponding to a spectrum between 827 meV and 2481 meV. To excite TE-like modes magnetic dipole sources oriented in the y direction were employed. These excite modes with in-plane electric field components. To excite TM-like modes y-oriented electric dipole sources were used.

The simulation was time-stepped up to 3 picoseconds or until the total electromagnetic energy in the system had decayed to 10^{-5} of its peak value, whichever was sooner. The full electric and magnetic fields were recorded as a function of time at 10 random locations in the simulation domain. The Fourier transforms of the three electric field components for the 10 locations were calculated and the spectral intensities added to produce a frequency spectrum. This was repeated for each Bloch wavevector and the locations of the spectral peaks vs. wavevector were extracted.

The peak positions vs. wavevector reveal the locations of the bands. The procedure detailed above was repeated for a range of hole etch depth, PhC periodicities (corresponding to different unit cell sizes) and hole diameters. A typical result for the hole diameter is shown in Fig. S2(a), where the maximum gap width is found when the diameter is close to half of the period. Fig. S2(b) shows the hole depth dependence.

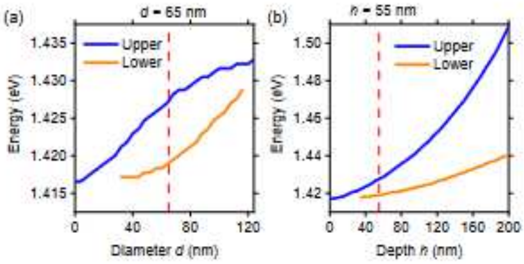

FIG. S2. Calculated TE-like photonic bands at the X point in the patterned planar waveguide using a period of $a = 130$ nm for the square photonic crystal. (a) Dependence on the radius of the holes using a depth of 55 nm. (b) Dependence on the depth of the hole using a diameter of 65 nm. The case with $d = 65$ nm and $h = 55$ nm is highlighted in both figures. The upper and lower bands are plotted for points where the calculated density of photonic states has a local maximum for the energy in question.

While the gap width increases for deeper holes, a maximum etch depth of 87 nm is used in fabrication to avoid damage to the quantum wells. The period can be used to adjust the energy of both bands simultaneously, as seen in Fig. 2b of the main article. The optimal parameters were those that gave the largest TE-like band gap with frequency centered at the exciton resonance frequency. A range of parameters around this point was chosen for fabrication.

[1] P. Bienstman and R. Baets, "Optical modelling of photonic crystals and VCSELs using eigenmode expansion and perfectly matched layers," Optical and Quantum Electronics **33**, 327–341 (2001).

[2] S. Gehrsitz, F. K. Reinhart, C. Gourgon, N. Herres, A. Vonlanthen, and H. Sigg, "The refractive index of $Al_xGa_{1-x}As$ below the band gap: Accurate determination and empirical modeling," Journal of Applied Physics **87**, 7825–7837 (2000).

[3] A. W. Snyder and J. D. Love, *Optical Waveguide Theory* (Springer, Boston, MA, 1983).

[4] S. G. Johnson, S. Fan, P. R. Villeneuve, J. D. Joannopoulos, and L. A. Kolodziejski, "Guided modes in photonic crystal slabs," Physical Review B **60**, 5751–5758 (1999).

[5] P. Y. Shapochkin, M. S. Lozhkin, I. A. Solovev, O. A. Lozhkina, Y. P. Efimov, S. A. Eliseev, V. A. Lovcjus, G. G. Kozlov, A. A. Pervishko, D. N. Krizhanovskii, P. M. Walker, I. A. Shelykh, M. S. Skolnick, and Y. V. Kapitonov, "Polarization-resolved strong light–matter coupling in planar GaAs/AlGaAs waveguides," Optics Letters **43**, 4526 (2018).

Chapter 4

Observation of Zitterbewegung in photonic microcavities

4.1 Introduction

Recent trends in condensed matter physics have been centred around the study of analogues to high energy phenomena. A prime example of such an analogue is the Zitterbewegung effect, a somewhat counter intuitive motion perpendicular to the ballistic trajectory of a particle[134]. Microcavities allow the direct imaging of the internal spinor wavefunction (via PL measurements) making them key candidates for the study of fundamental but so far elusive spin-orbit effects such as Zitterbewegung. The spin-orbit coupling in such microcavities manifests as TE-TM splitting and in some cases they also have a birefringent polarisation splitting; an anisotropy in polariton state distribution dependant on propagation direction within the cavity. These features have allowed observation of a range of important physical effects such as the optical spin-Hall effect[90], the emergence of monopoles[135] and the onset of the non-Abelian gauge fields[136, 137]. Whilst the hybrid nature of polaritons have provided a range of fascinating effects such as optical condensates with macroscopically large coherence length [138] and the formation of acoustic black holes with the hawking effect[8], this work concerns effects derived from the photonic element of polaritons. More specifically, highly photonic polaritons ($> 98\%$) are used to demonstrate fundamental principles first predicted by Schrödinger for the motion of free electrons governed by the Dirac equation[139]. Furthermore, this work also combines the highly topical engineering of microcavity polariton bandstructures in the form of lattice potentials with Zitterbewegung, in part due to the high tunability of the band structure to aid in the experiments performed.

Zitterbewegung consists of an oscillatory motion of a propagating wave packet perpendicular to its ballistic trajectory, despite the absence any forces in the perpendicular direction i.e. for a polariton propagating in the y-direction, Zitterbewegung will manifest solely in the $x(z)$-direction [134]. It appears due to interference between positive and negative energy states of a split two component system, enabled by the coupling of the spin and momentum degrees of freedom.

Qualitatively, these oscillations arise as a consequence of the OSHE for polaritons propagating with some ballistic trajectory. As the pseudospins of the polaritons precess around the in plane magnetic field (arising due to the TE-TM splitting) along their propagation path, they experience a pulling force perpendicular to their trajectory, the same force that creates polarisation quadrants in the typical OSHE. The direction of this pulling force is then dependant on the orientation of the newly precessed pseudospin (either σ^+ or σ^-). Since the direction of the magnetic field experienced by the polaritons varies with changes to their in-plane momentum, the pseudospins then precess again thus pulling the polaritons back in the opposite direction, overall leading to an oscillatory trajectory in the direction perpendicular to their ballistic trajectory.

In addition to the case predicted by Schrödinger for free relativistic electrons, the effect has been predicted for electrons in crystals with Rashba and Dresselhaus SOC [140–142]. The predicted high frequency and low amplitude of the oscillations for the vacuum case, and the difficulty in observing single electrons in the crystals make experimental observation very challenging[134]. So far, several Zitterbewegung observations in analogous systems have been made, but these often involve indirect measurements, for example experiments performed by Gerrtisma et al.[143]. These experiments involved the quantum simulation of the Dirac equation using a single trapped ion with oscillations in transverse positions observed. High frequency oscillating currents were also observed in the motion of spin-polarised electrons in a doped semiconductor device[144].

In optics the Zitterbewegung effect was observed in an array of coupled waveguides[145]. In this case the energy splitting used to induce Zitterbewegung was a fixed value determined by the geometry of the waveguides. This fixed splitting meant tunability of the Zitterbewegung period and amplitude was not possible using a single lattice. The Zitterbewegung also had to be detected indirectly using fluorescence measurements. This further highlights the benefits of using microcavities in the study of Zitterbewegung since they allow direct imaging of the internal wavefunction along with allowing relative ease of access to areas of different energy spitting on the dispersion. This becomes obvious when considering the fact the TE-TM splitting between branches increases as the in-plane wavevector of the polariton states increases, thus to excite different regions on said dispersion only the energy and angle of incidence of the laser needs to be changed. It was also recently reported that transverse oscillations of a condensate in an etched ring trap were observed. [146]. However, in this case, no direct observation of Zitterbewegung was possible. In general, oscillations in structures with transverse trapping potentials are hard to attribute to Zitterbewegung since there are alternative explanations such as interference between multiple transverse modes[72].

So far Zitterbewegung has not been directly observed in a polariton microcavity structure such as those in this chapter. The motivation for this work arose due to recent theoretical predictions of Zitterbewegung in planar microcavities[5] and also the suggestion for its presence in honeycomb lattices near the Dirac point[147].

This chapter presents observations of Zitterbewegung with varying periods and amplitudes in a planar microcavity, achieved by exciting TE-TM split modes in the LPB, whilst also taking into account the effects of birefringence in the microcavity. It is shown that the Zitterbewegung only arises when two branches are equally excited using two different approaches. The period and amplitude of the Zitterbewegung oscillations are then varied by exciting the TE-TM modes in regions of larger and smaller energy splitting, highlighting the predicted inverse dependency of the period of oscillations on the value of energy splitting. A similar dependency is also observed for the amplitude but is not quite as clear. The results for the planar case are in good agreement with numerical simulations especially when considering the calculated error in the measurements. The work also shows the presence of Zitterbewegung for polaritons in states close to the Dirac point of a etched micropillar honeycomb lattice. In this case it is shown that the ability to engineer the bandstructure allows observation of Zitterbewegung with a smaller period whilst retaining an observable amplitude by again by taking advantage of the TE-TM split branches. These results are also in good agreement with numerical simulations. It is hoped that these analogue demonstrations will help lead to a deeper understanding of fundamental effects in relativistic systems whilst also helping to expand on well-established pseudospin related phenomena such as the OSHE in the field of polariton physics.

The work presented in the following chapter was undertaken by myself with support from Dr Charles Whittaker and Dr Paul Walker. The work pertaining to the honeycomb lattice was done by both myself and Dr Charles Whittaker. Dr Paul Walker assisted with the work pertaining to planar cavities whilst also developing the energy splitting description and calculation the uncertainties.

4.2 Experimental parameters and design

4.2.1 Sample description

In the case of the planar microcavity, the structure has a two wavelength thick cavity layer enclosed between two Bragg mirrors. The cavity in this sample is made from GaAs whilst the mirrors are alternating layers of GaAs and $Al_{0.85}Ga_{0.15}As$ all grown via MBE. Three $In_{0.04}Ga_{0.96}As$ QWs are embedded in the cavity layer to provide the excitonic component of the polaritons. Since the work involves highly photonic polaritons, a microcavity with a very large detuning is required, the sample selected has a detuning of at least -20 meV.

For the case of the honeycomb lattice, the devices exist on the same sample very close to region for which planar measurements are made. The devices themselves are deep etched micropillar arrays forming a hexagonal or honeycomb shape, alternatively known as photonic graphene. Each pillar had a width of 3μm and are overlapped such that the centre to centre distance between neighbouring pillars is $d = 2.8\mu m$ giving a lattice periodicity $a = d\sqrt{3}$.

4.2.2 Energy splitting description

The energy splitting observable in the dispersion is fundamental to the observation Zitterbewegung. Due to the slight optical birefringence[148–150] present in this sample there is a complicated splitting between the linear polarization states, more so than for a sample with just contributions from TE-TM splitting. For small values of k the components of the Hamiltonian in the basis of circular polarised states is as follows[150]

$$\hat{H} = \begin{pmatrix} \frac{\hbar^2 k^2}{2m} & \frac{\Omega}{2} - \beta(k'_x - ik'_y)^2 \\ \frac{\Omega}{2} - \beta(k'_x + ik'_y)^2 & \frac{\hbar^2 k^2}{2m} \end{pmatrix}, \tag{4.1}$$

where m is the reduced mass of the polaritons, k'_x and k'_y are the in plane wavevector components of the photons in the sample reference frame where x' is the fast axis of the microcavity, $k^2 = {k'_x}^2 + {k'_y}^2$, and the parameters Ω and β describe the values of the k-independent optical birefringence and TE-TM splitting respectively. β is related to the difference between the effective masses of the TE photons, m_t, and TM photons, m_l, as[151]

$$\beta = \frac{\hbar^2}{4}(\frac{1}{m_t} - \frac{1}{m_l}). \tag{4.2}$$

Here β is defined with an opposite sign than typically seen in literature but this does not affect the physics. The energy for states in the two branches split in linear polarisations can now be given as

$$E_{\pm}\frac{\hbar^2 k^2}{2m} \pm \sqrt{\beta^2 k^4 - \beta\Omega k^2 cos2\phi + \frac{\Omega^2}{4}}, \tag{4.3}$$

where ϕ is the in-plane angle between the wavevector $\boldsymbol{k'}$ and the x'-axis of the microcavity. Using these definitions it can be seen that the TE polarised mode (electric field perpendicular to $\boldsymbol{k}'$) increases faster with k than the TM mode for positive β and that, for positive Ω, the mode polarised along x' has a higher energy at $k = 0$. The combination of birefringence and TE-TM splitting leads to the crossing of the branches for $\phi = 0°$ at $k = \sqrt{\frac{\Omega}{(2\beta)}}$. This is clearly seen when experimental characterisation of the sample is presented in the next subsection.

4.2.3 Characterisation of sample

The experiments in this chapter are performed using the transmission configuration shown in Figure 2.6 using the a continuous flow cryostat. This method allows the sample to be cooled to approximately 10K. The $E - k_y$ dispersions are measured at $k_x = 0$ using PL spectroscopy. The x and y coordinates are defined in the laboratory frame (see Figure 4.1).

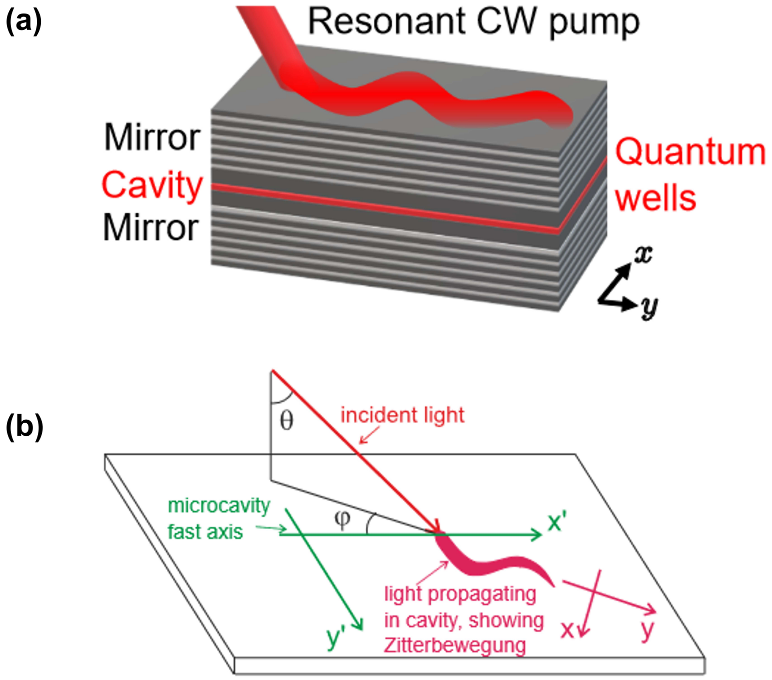

Figure 4.1: (a) Simplified schematic showing the laser incident on the sample with Zitterbewegung present in propagation path. The x and y coordinates relative to the sample in the laboratory frame are defined. (b) More detailed sketch than (a) showing the incident laser with Zitterbewegung in the propagation path. x and y coordinates are defined relative to the x' and y' coordinates. θ and ϕ are also defined.

For the planar cavity, there are two cases that must be considered. The first case is where the sample is orientated such that $\mathbf{k} = k_y\vec{y}$ is parallel to y' ($\phi = 90°$). The dispersion at $k_x = 0$ in this case shows two energy split branches. At $k_y = 0$ there is splitting due to birefringence whilst the TE-TM splitting causes the splitting to increase as k_y increases. The second case is where the sample is rotated 90° relative to the first such that $\mathbf{k} = k_y\vec{y}$ is parallel to x' ($\phi = 0°$). In this case the dispersion crossing described in subsection 4.2.2 can be seen at $\theta = 5.7°$ ($k = 0.73\mu m^{-1}$). It is important to distinguish between these two cases as the period of Zitterbewegung is expected to vary with the magnitude of energy splitting and in the two cases of sample orientation the splitting will be different even at the same point on the dispersion.

Along with Eqns.(4.2) and (4.3), the dispersions can be fitted as described in subsection 2.2.1 to give the following values of $\Omega = 43 \pm 19\mu eV$, $\beta = 33.6 \pm 3.5\mu eV\mu m^2$. The energy at $k = 0$ (averaged between the two dispersions) is 1.4531eV and $\hbar^2/(2m) = 947.5\mu eV\mu m^2$.

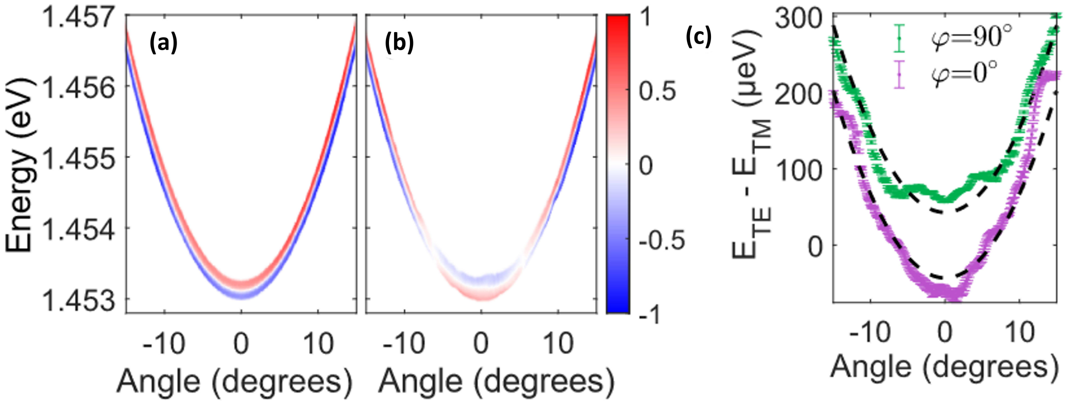

Figure 4.2: (a) Angle and polarisation resolved PL spectrum showing the dispersion relation $E(k_y)$ at a fixed $k_x = 0$ for the case where the birefringent crystal principle axis y' ($\phi = 90°$) is parallel to the y-direction along which the polaritons are resonantly injected during the experiment (see subsection 4.2.4). (b) The same as in (a) but for the case where x' is parallel to y ($\phi = 0°$). In both (a) and (b) the colour scale indicates indicated the polarisation degree $(I_x - I_y)/(I_x + I_y)$ with red indicating the x polarisation and blue indicating the y polarisation (I_x and I_y are the intensity in the x and y polarisations respectively). (c) The energy splitting between the TE and TM polarisation for the two values of ϕ. The points show the values extracted by fitting Lorentzian peaks to the data in panels (a) and (b). The dashed black curves are the fits described in this subsection and subsection 4.2.2.

4.2.4 Experimental procedure

To observe Zitterbewegung, the sample is resonantly excited with a tunable continuous wave Ti:Sapphire laser (as in Figure 4.1). The angle and energy of the laser is carefully tuned to excite different desired regions on the polariton dispersion, corresponding to regions of different energy splitting between the branches. The laser spot on the sample is circular with FWHM of 15μm , a size carefully chosen such that in reciprocal space (its Fourier transform) it is sufficiently large to excite both branches, a requirement to induce Zitterbewegung. The excitation polarisation is also set to circular for the same reason. The emission is collected using the transmission configuration described in subsection 2.1.4. The collection lenses are arranged such that in the case where $\phi = 90°$ the magnification is m=18x and the effective focal length of the k-space setup is f=4.6mm. For the case where $\phi = 0°$ the magnification is m=20.5x and the effective focal length of the k-space set-up is f=6mm. The total intensity of the collected real space emission is recorded by the CCD. An example of this is shown in Figure 4.3.

The excitation optics in the case of the honeycomb lattice are much the same as

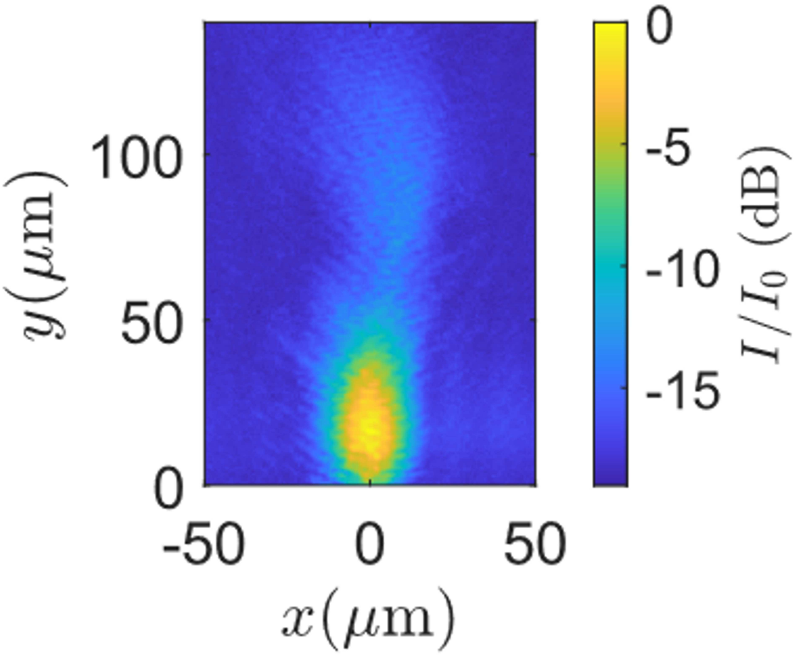

Figure 4.3: Intensity of the photon field in the cavity when excited resonantly vs. x and y . Colour scale gives the intensity I relative to the peak intensity I_0 in decibel units. The laser spot is centred around 17μm.

in the planar case. However, excitation is required close to the Dirac point and the resonant excitation cannot simply be visualised using the dispersion in-situ.

The most effective approach to calculating the angle of excitation required is to calculate the location of the Dirac points in k-space and find the corresponding angle of excitation to inject photons directly. From there, the angle of incidence and laser energy can be adjusted to excite different regions in k-space on the honeycomb dispersion close to the Dirac points, this is aided by plots of the dispersion created using a tight binding model.

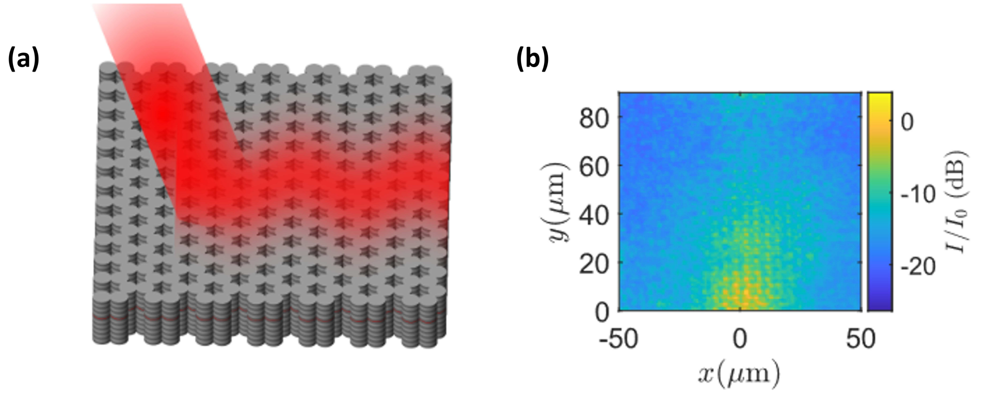

Figure 4.4: (a) Diagram showing the resonant laser incident on the etched honeycomb lattice micropillar array at some incident angle, $\boldsymbol{\theta}$. (b) Real space total intensity vs. $\boldsymbol{x}$ and $\boldsymbol{y}$ recorded for excitation close to the Dirac point in real space (see Figure 4.11). Colour scale gives the intensity I relative to the peak intensity I_0 in decibel units.

4.2.5 Result processing

The observed propagation of the polaritons in the y-direction in due to the fact the laser is incident on the sample at a finite angle in the same direction, in turn giving the polaritons a group velocity. This group velocity can be determined from the slope of the dispersion at the wavevector corresponding to the laser angle. This PL emission of the polaritons is used to analyse their distribution in the propagation path and is where Zitterbewegung oscillations are expected to manifest. To analyse this propagation path, for every value of y a slice along x is taken to find the value at which intensity is maximum. The centre of intensity can then be defined as

$$x_c(y) = \frac{\int \int_{-\infty}^{\infty} x \cdot I(x,y) \cdot dx}{\int \int_{-\infty}^{\infty} I(x,y) \cdot dx}. \tag{4.4}$$

Using Eqn.(4.4), the centre of intensity in x, x_c, can be plotted against y, this will show any oscillations in x_c for the polaritons propagating in the y-direction.

4.2.6 Determining sources and size of uncertainty in centre of intensity

Random scatter in the extracted centre of intensity data points arises due to noise in the intensity images recorded by the CCD camera. The noise mainly consists of CCD dark counts and read noise. To estimate the error bars, a model of the contribution of experimental noise to the centre of intensity is used. The intensity is recorded on the CCD camera as a number of counts, n, per pixel as a function of x and y. n can be written as the sum of two terms: signal counts n_s and random noise counts n_n. The noise counts per pixel are modelled as being independent from one another and being normally distributed with zero mean and variance, σ^2.

From Eqn.(4.4), the centre of intensity then becomes

$$x_c(y) = \frac{\sum_{i=-N}^{N} x n_s + \sum_{i=-N}^{N} x n_n}{\sum_{i=-N}^{N} n_s + \sum_{i=-N}^{N} n_n}, \tag{4.5}$$

where the index i runs over the $2N$ pixels in the x direction over which the signal is defined and the corresponding values of x run from $-x_{max}$ to x_{max}. The total number of signal counts is defined as

$$S = \sum_{i=-N}^{N} n_s. \tag{4.6}$$

The denominator of Eqn.(4.5) is normally distributed with mean S and variance $2N\sigma^2$. Provided that $S >> \sigma\sqrt{2N}$ (which is always fulfilled in experiments), the value x_c from Eqn.(4.5) is approximately normally distributed (verified numerically) with variance

$$\sigma_c^2 \approx \frac{2(N+1)(2N+1)}{6N}(\frac{\sigma x_{max}}{S})^2. \tag{4.7}$$

This formula gives the uncertainty in x_c due to the noise in the data. To plot the error bars in Figures 4.(6,7,8,12), S is estimated from the experimental data by summing the counts over all pixels (2N). The value of σ is obtained from the experimental data by taking the standard deviation of all points at large values of x including points where the signal is negligible. Using these values for S and σ the value of σ_c from Eqn.(4.7) can be used as the size of the error bars for each point in the centre of intensity data. Note that the signal reduces exponentially due to finite photon lifetime in the cavity resulting in an exponentially decreasing signal to noise ratio with increasing propagation distance hence an increase in error bar size the further from the excitation spot.

Small error contributions can also arise due to imperfections in optics, small reflections from optics along the beam path and parasitic environmental light. However, there is no evidence of this in CCD data, ruling out the fact it has anything other than potential slight modifications of the measured centre of intensity. These contributions are most likely to affect the centre of intensity where the signal is weak such as at large values of x and y.

4.3 Results

4.3.1 Planar microcavity: changing the degree of resonance

To observe Zitterbewegung, direct resonant excitation of the TE-TM branches on the LPB is performed, with the region of excitation on the dispersion chosen such that the period and amplitude will be sufficiently large for observation. The theory proposed by E.S. Sedov et. al [5], states that the larger the energy splitting the smaller the amplitude and period of Zitterbewegung oscillations. Since the splitting varies with angle, an appropriate angle is chosen where the splitting is significant but not too large. This angle is chosen to be 10°. A scan across the dispersion starting at low angle and ending at high angle is done to highlight the fact the Zitterbewegung is a result in the interference between two split branches. Circular polarisation is used to excite the polarisation branches to ensure equal excitation.

At lower angle, the excitation spot in reciprocal space has a small amount of overlap with the branches and thus Zitterbewegung is weak but still observable. This case is shown in Figure 4.5 (b). At resonance, both branches are near equally excited thus Zitterbewegung is strongest and clear oscillations are observed. This case is shown in Figure 4.5(c). Far after resonance, the reciprocal spot has no overlap with the two branches and thus Zitterbewegung disappears when analysing the propagation path. This case is shown in Figure 4.5(d). Even thought the lower and upper bounds of the scan are equal around the centre resonant point, the reasoning for the presence of Zitterbewegung being present only in the low angle and its quick disappearance as the angle increases past resonance can be explained when considering the 3-dimensional cone shape of the polariton dispersion. Photons on the inside region of the cone are able to excite polariton states of slightly lower energy due to the fact the dispersive cone at lower states curves towards the spot in reciprocal space causing small overlap whilst in the region outside the dispersive cone the allowed states curve away from the spot thus no overlap.

Another approach to highlight the fact Zitterbewegung occurs due to the interference of two branches is to fix the position of the laser in k-space and change the polarisation. By exciting with circular polarisation both branches are excited and Zitterbewegung should be present, when switching to linear polarisation, only a single branch will be excited and Zitterbewegung should disappear. The results

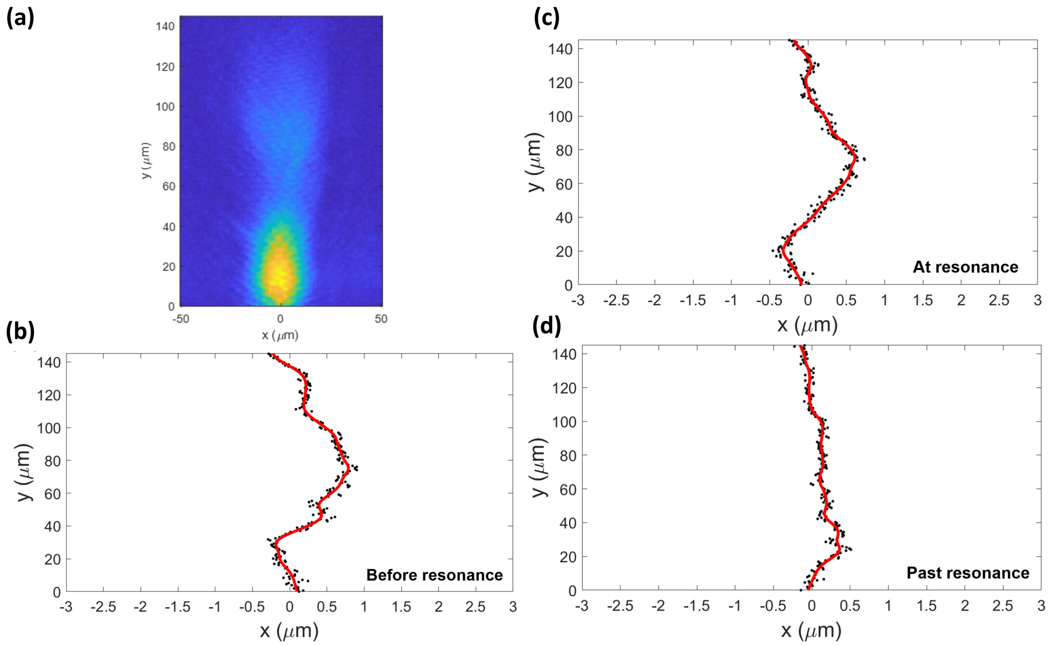

Figure 4.5: (a) Real space image showing the total intensity of emission when exciting resonantly at 10° on the dispersion for the case where $\phi = 0°$ in Figure 4.2(b). The laser is at energy of approximately 1.455 eV. (b) Analysed propagation using Eqn.(4.4) showing the centre of intensity in x vs y for the case where the laser is incident at low angle and has little overlap with the branches. (c) The same as in (b) but for the case where the laser is now resonant with both branches and excites them both equally. (d) The same as in (b) and (c) but for the case where the laser is far past resonance and high angle with no overlap with the branches. In (b), (c) and (d) the black points denote the raw experimental data points and the red line shows the smoothing of the data with a 20μm rectangular smoothing window.

of this are shown in Figure 4.6 below when exciting at an angle of 11°.

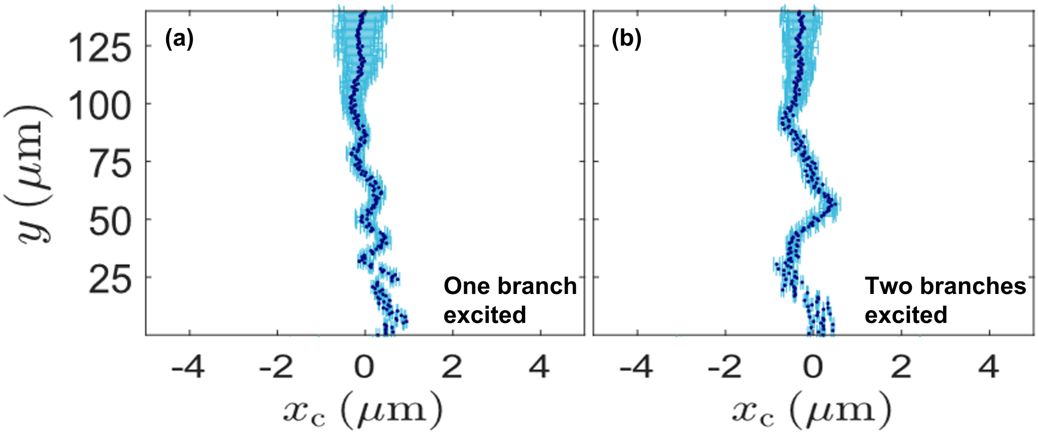

Figure 4.6: (a) Analysed propagation path for the case where the excitation polarisation in set to linear. In this case only a single branch is excited and no Zitterbewegung manifests. (b) The same as in (a) but with the excitation polarisation set to circular. In this case both polarisation branches are excited equally and Zitterbewegung is observed. In both (a) and (b) the angle of incidence of the laser is 11° and the energy of the laser is approximately 1.4545 eV for the case where $\phi = 90°$. In (b) and (d) the dark blue points denote the experimental data and the error bars are in lighter blue.

4.3.2 Planar microcavity: changing the energy splitting

As mentioned, the connection between the period and amplitude of the Zitterbewegung oscillations and the magnitude of the energy splitting is expected to be of inverse proportionality as proposed in Ref.[5]. To test this experimentally, the laser is made to be resonant with different regions on the dispersion with various values of energy splitting between the polarisation branches. The energy and incident angle of the laser is changed to achieve this. As expected, when exciting resonantly at high angles (and thus large TE-TM splitting) the period decreases. For example, for the case where $\phi = 90°$, when exciting resonantly with circular polarisation at 8.5°, the period of oscillation is significantly larger than when exciting resonantly with circular polarisation in the same spot on the sample but at 10°. There are also small changes in the amplitude however these are less clear than the changes in period. This case can be seen in Figure 4.7. For the

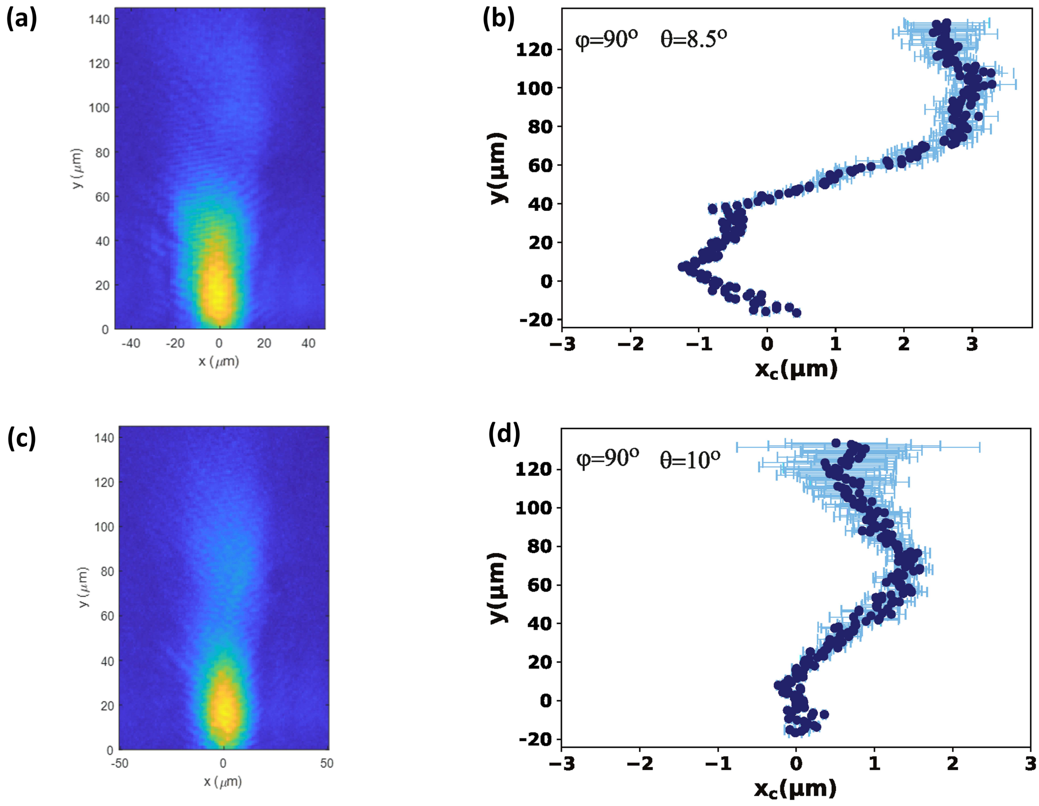

Figure 4.7: (a) Real space total intensity image showing the propagation in the y-direction when the angle is resonant with the dispersion at 8.5° for the case when $\phi = 90°$. (b) Plotted centre of intensity for the data shown in (a) with clear Zitterbewegung manifesting along the x_c axis. (c) Real space total intensity image showing the propagation in the y-direction when the angle is resonant with the dispersion at 11° for the case when $\phi = 90°$. In this case the energy splitting between the polarisation branches is less than in (a). (d) Plotted centre of intensity for the data shown in (c) with clear Zitterbewegung manifesting along the x_c axis. In (b) and (d) the dark blue points denote the experimental data and the error bars are in lighter blue.

orientation of the sample where $\phi = 0°$, the change in period of the Zitterbewegung oscillation is qualitatively the same, a significant decrease is observed when the angle (and thus energy splitting) is increased. In this case, comparison can be made between resonant excitation of 8° and 12° as shown in Figure 4.8. The variation in the period at similar angles of incidence when compared to the case where $\phi = 90°$ arises due to the difference in splitting between the polarisation branches. As described in subsection 4.2.2, this variation in splitting arises due to birefringence of the sample and a visualisation for the splitting in each orientation can be seen in Figure 4.2(c).

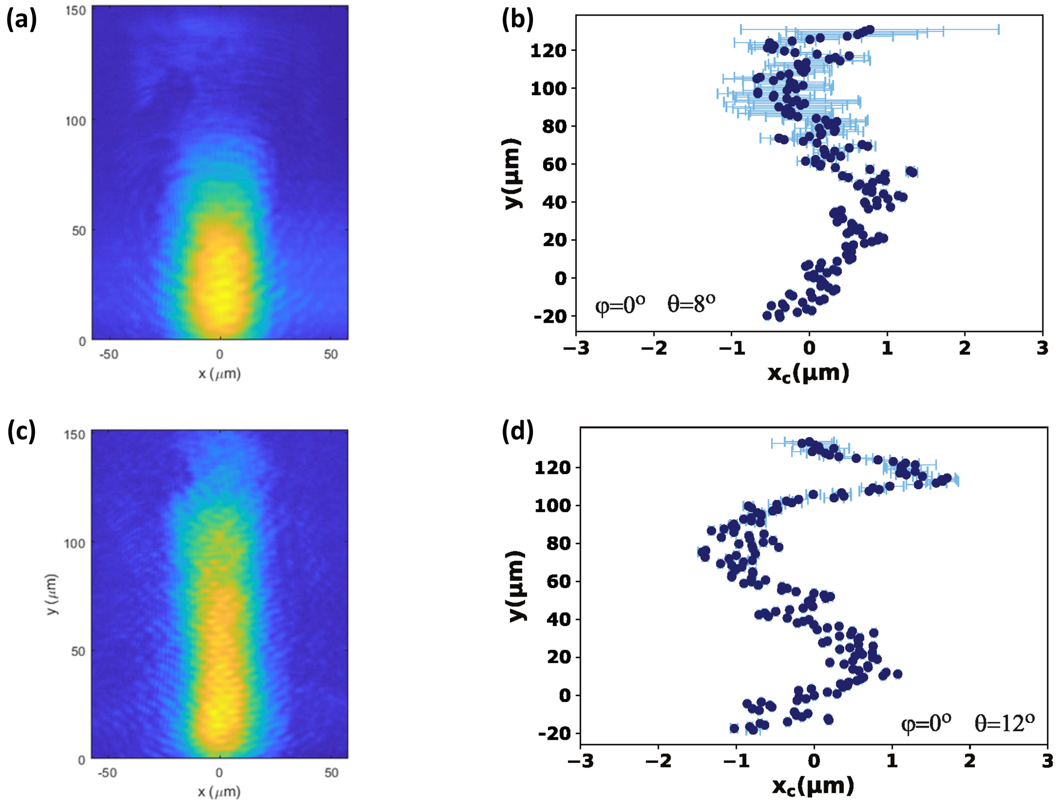

Figure 4.8: (a) Real space total intensity image showing the propagation in the y-direction when the angle is resonant with the dispersion at 8° for the case when $\phi = 0°$. (b) Plotted centre of intensity for the data shown in (a) with clear Zitterbewegung. (c) Real space total intensity image showing the propagation in the y-direction when the angle is resonant with the dispersion at 12° for the case when $\phi = 0°$. In this case the energy splitting between the polarisation branches is less than in (a). (d) Plotted centre of intensity for the data shown in (c) with clear Zitterbewegung. In (b) and (d) the dark blue points denote the experimental data and the error bars are in lighter blue.

4.3.3 The Stokes parameters

Whilst analysing the centre of intensity along the propagation path of polaritons provides an excellent method for the observation of Zitterbewegung, the effect is perhaps more dramatic when calculating and plotting the Stokes vectors for the polariton emission. In Ref. [5], so called ”interlocking fingers” are predicted to appear when observing each of the Stokes parameters. This fits with the common understanding of Zitterbewegung in microcavity polaritons being a manifestation of the OSHE effect for polaritons with ballistic trajectory. The ”interlocking fingers” correspond to the polarisation domains synonymous with the OSHE due to the effective TE-TM magnetic field. As the polaritons propagate in the y-direction, their pseudospins precess according the direction of the effective field creating polarisation patterns in the spatial distribution of the stokes vectors.

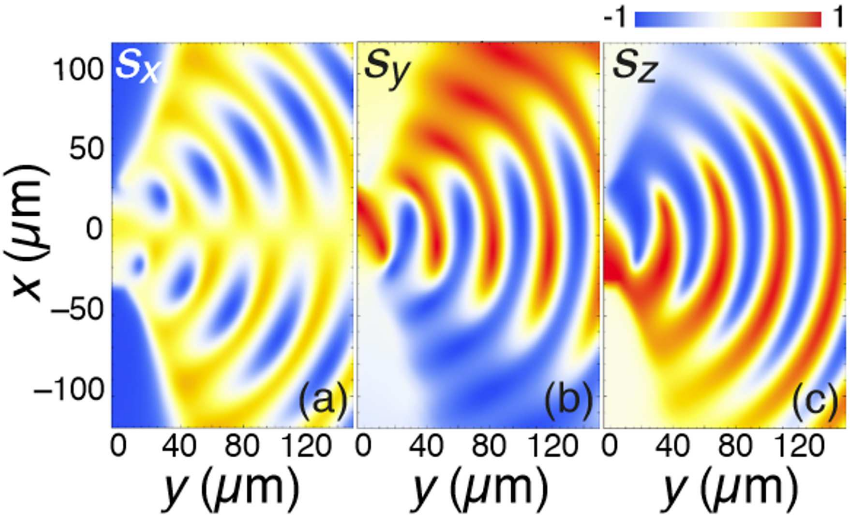

Figure 4.9: (a) S1 parameter along the propagation path in the y-direction showing the polarisation domains expected to manifest. (b) The same as in (a) but for the S2 parameter (c) The same as in (a) but for the S3 parameter. (a-c) taken from [5]**.**

The data showing Zitterbewegung in previous subsections are typically not polarisation resolved but small amounts of data are taken using polarisation optics. When calculating the Stokes parameters for this data, as seen in Figure 4.10, clear polarisation domains are present along the propagation path. This data does not fully resemble ”interlocking fingers” due to weak signal laterally away from x=0. However, the polarisation domains that are present clearly correspond to same patterns that would be seen if only considering a narrow path through the centre of the ”interlocking fingers” shown in Ref. [5].

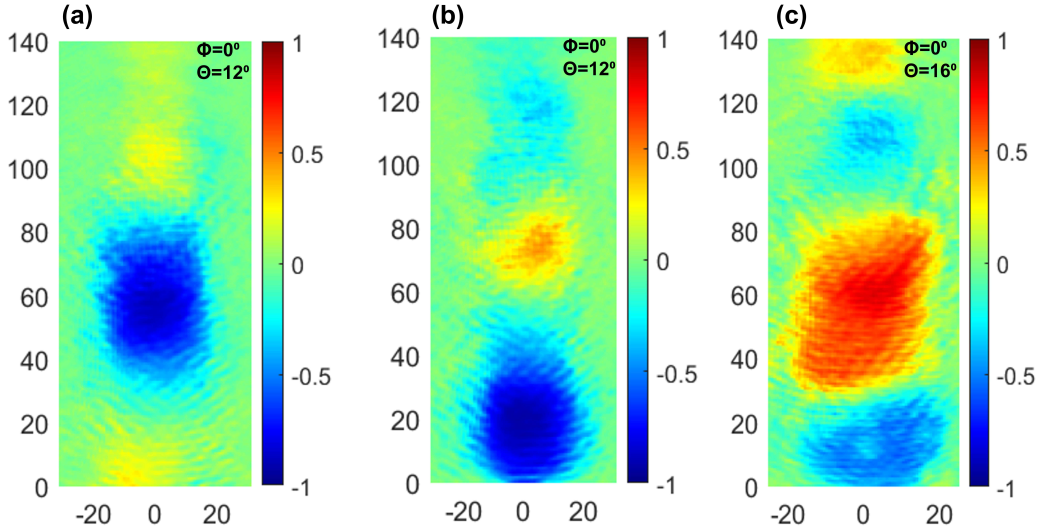

Figure 4.10: (a) S1 Stokes parameter along the propagation path in the y-direction for the case where $\phi = 0°$ and $\theta = 12°$ when exciting with σ^+ polarisation. (b) S2 Stokes parameter along the propagation path in the y-direction for the case where $\phi = 0°$ and $\theta = 12°$ when exciting with σ^+ polarisation. (c) S3 Stokes parameter along the propagation path in the y-direction for the case where $\phi = 0°$ and $\theta = 16°$ when exciting with σ^+ polarisation.

4.3.4 Zitterbewegung near the Dirac point in a honeycomb Lattice

The excitation of the samples in the honeycomb lattice case is performed in much the same way as in the planar case. The TE-TM splitting that is so crucial for Zitterbewegung in the planar case is still present in the honeycomb lattice case. However, the mechanism is slightly different since the splitting arises in micropillar lattices due to different tunnelling probabilities between pillars depending on the polarisation of the photonic mode. The end is result is the same as in the planar case, the TE-TM splitting of branches into smaller, energy-split sub-branches. For the case of the honeycomb lattice, the k-space spot is positioned near the Dirac point of the s and p bands in the complex honeycomb lattice band structure. These s and p-bands are a result of the different allowed states in the micropillars with the s-bands resembling the lowest order Hermite-Gauss modes. The p-bands are the next highest set of bands and are composed of the first order Hermite Gaussian modes of the individual pillars. For the purpose of this thesis the essential difference between the two sets of bands is that the polarisation tunnelling rates from pillar to pillar are different resulting in different a different energy splitting and group velocity close to the Dirac points. Therefore, it is expected that Zitterbewegung oscillations will have a different period and amplitude close to the Dirac point in each band.

The red and black dots in Figure 4.11(a) denote the energy and wavevector at which the bands were excited to measure Zitterbewegung. As in the planar case, both branches are excited equally. More detailed plots are given in Figure 4.11(b) and (c) for the p-bands and s-bands respectively. They were obtained from a tight binding model using parameters from Ref. [147] where the same lattice was studied extensively and the model was fit to the dispersion. The colour of the lines represents the polarisation of the branches with the blue lines representing y polarised branches and red lines representing x polarised branches. In Figure 4.11(b-c) the dots represent the detailed position of excitation relative to the Dirac point. The red dot in Figure 4.11(c) denotes the position of excitation on the s-band close to the Dirac point and the black dot in Figure 4.11(b) represents the position of excitation in the p-band close to the Dirac point. Around these excitation points the energy splitting between the polarised branches is 65μeV for the s-band and 96μeV for the p-band. The wavevector splitting, Δk_y, between the two polarised branches at the fixed laser energy is $0.49x2\pi/(3a)$ for the s-bands and $0.25x2\pi/(3a)$ for the p-bands. As in the planar

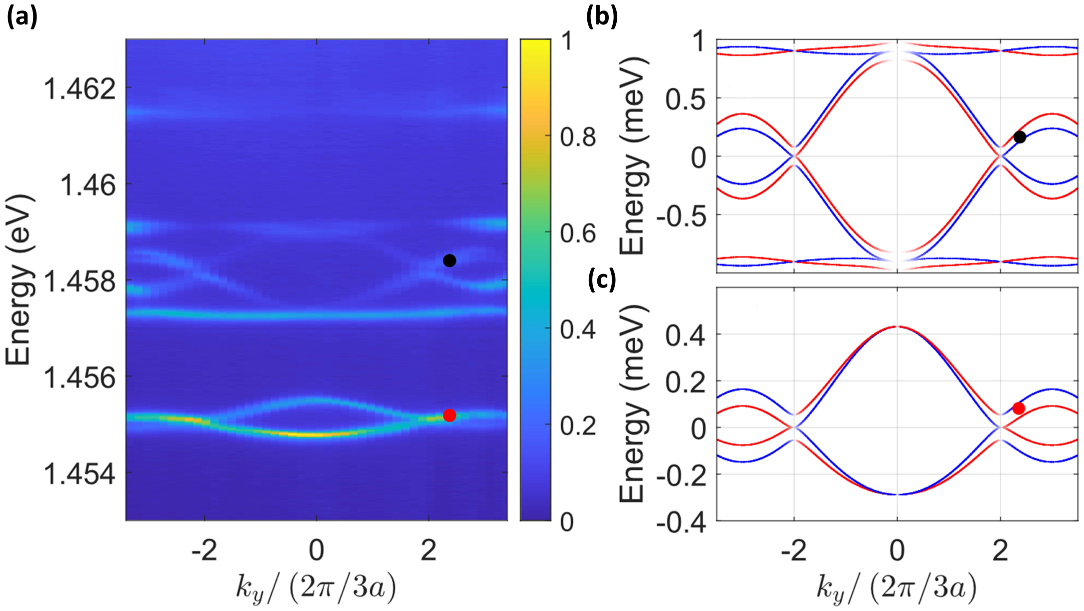

Figure 4.11: (a) Experimentally obtained PL dispersion showing the bandstructure of the LPB in the honeycomb lattice studied in this chapter. The black dot denotes the excitation location in the p-band. The red spot denotes the excitation location in the s-band. (b-c) Dispersion of the p-bands (b) and s-bands (c) calculated using a tight binding model with parameters from Ref. [147]. Red and blue branches represent states linearly polarised along x and y respectively.

case, Eqn.(4.4) can be used to extract the centre of intensity from the CCD data of the propagating polaritons. The resulting extracted trajectories can be seen in Figure 4.12. Zitterbewegung oscillation are again visible with a shorter period and smaller amplitude for the measurements taken in the s-bands. Since the period and amplitude is expected to scale inversely with the energy splitting, the shorter period for the s-band is consistent with the larger energy splitting at the excitation point in the s-band.

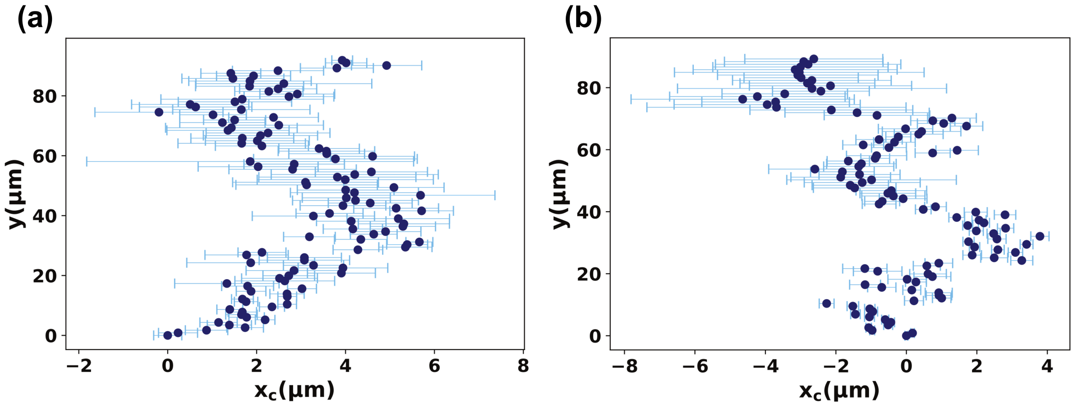

Figure 4.12: (a) Plotted centre of intensity vs propagation in y for excitation close to Dirac point in the p-band (Black circle in Figure 4.11). Blue points are the experimental data, and the lighter blue lines are error bars. (b) Same as in (a) but now for excitation close to the Dirac point in the s-band (red circle in Figure 4.11).

4.4 Comparison with theory

To compare the results with theory, numerical simulations were performed by Alexey Osipov and Alexey Yulin at ITMO University for both the planar and honeycomb lattice cases. A detailed explanation of the method involved in these numerical simulations can be found in Appendix A in the form of supplementary material created in preparation for journal submission. The parameters used in the numerical simulations were obtained experimentally and are given in subsection 4.2.3. Modelling in the planar case takes into account the birefringence of the cavity along with TE-TM splitting contributions for both cases. The results of the numerical simulation are plotted alongside the experimental data in the planar case below.

As Figure 4.13 (a) and (b) shows, the results of the numerical simulations for the period and amplitude in the case where $\phi = 0°$ are in excellent agreement with the experimental data points. Perhaps more importantly the values of β and Ω

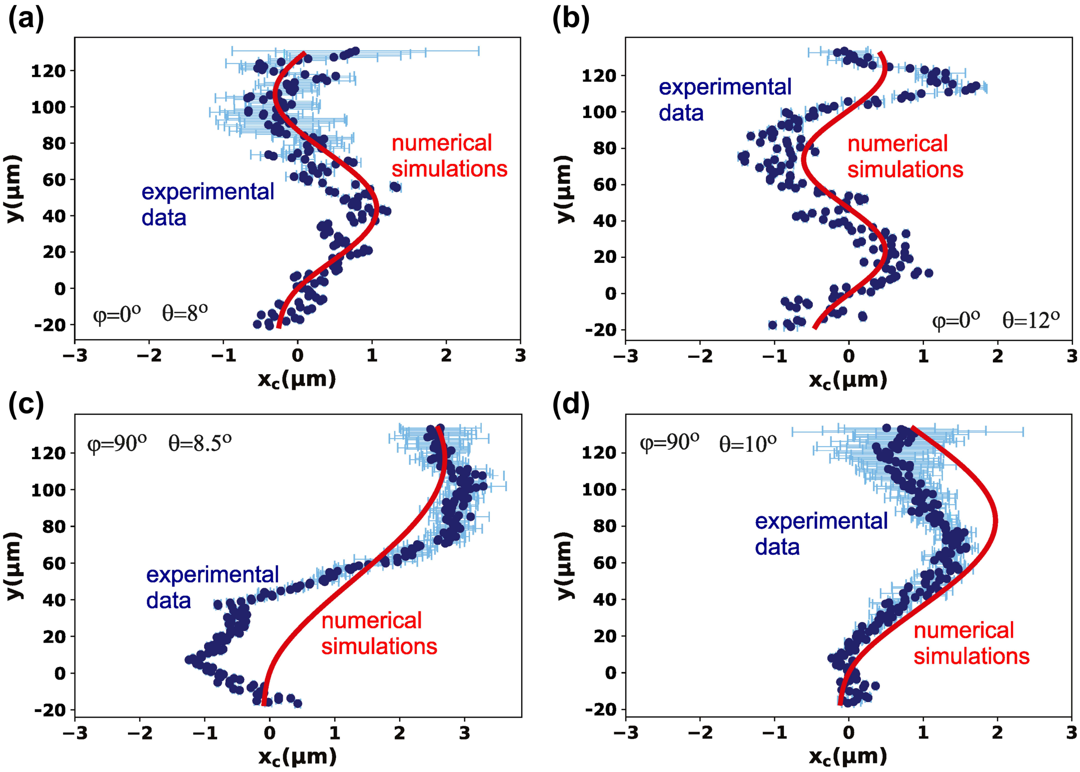

Figure 4.13: (a-b) The same experimental data as shown in Figure 4.8(b) and (d) respectively but now plotted alongside the results of numerical simulations performed using the same experimental parameters for each case. (c-d) The same experimental data as shown in Figure 4.7(b) and (c) but now plotted alongside the results of numerical simulations performed using the same experimental parameters for each case.

found from fitting the oscillations theoretically are in good agreement with the values found independently via fitting the dispersion relations (β agrees within 0.33 of the uncertainty and Ω agrees within 0.75 of the uncertainty). For the case where $\phi = 90°$, as shown in Figure 4.13 (c) and (d), the same parameters were used to simulate the trajectory. In this case a semi-quantitative agreement between the theory and experimental data is obtained. The reason for deviation in agreement in this case compared to the case where $\phi = 0°$ for both the period and the amplitude is due to the crossing of the polarisation branches as seen in

Figure 4.2(b) at 5.7°. Since the excitation spot in k-space is relatively close to this position the energy splitting becomes more complex. At the crossing point there is no splitting and close to it the oscillations become very sensitive to the exact experimental parameters.

For the honeycomb case the numerical simulations used the parameters from Ref.[147] where exactly the same lattice was studied. The results of the numerical simulations are shown along side the experimental data in Figure 4.14.

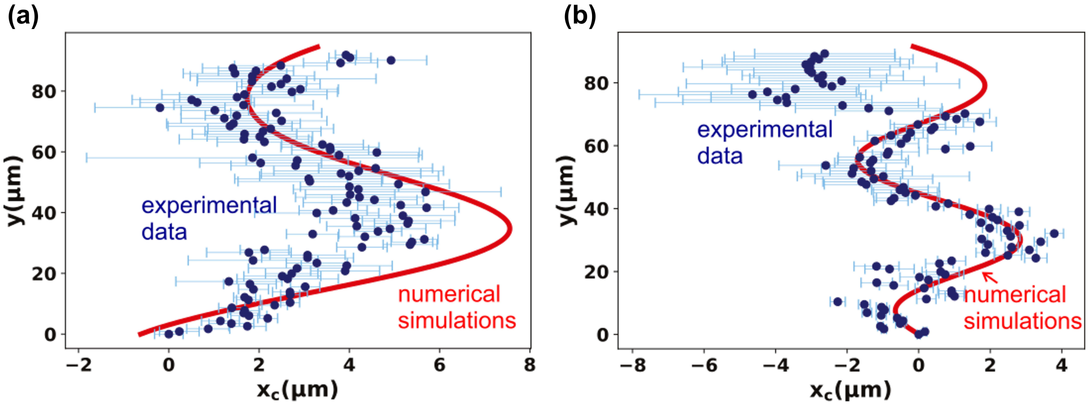

Figure 4.14: (a) The same experimental data as shown in Figure 4.12(a) but now plotted alongside the results of the numerical simulations performed using the same experimental parameters. (b) The same as in (a) but for the experimental data shown in Figure 4.12(b).

In the case for the honeycomb lattice a semi-quantitative agreement between the theory and experimental data for the period and amplitude is obtained. Whilst this agreement is good, some deviations may be in part due to the complex nature of the energy splitting of band structure close to the Dirac points and reliance of exact experimental parameters for a better agreement.

4.5 Summary and conclusion

The work presented in this chapter demonstrates the first direct observation of Zitterbewegung in a microcavity structure. It highlights how Zitterbewegung arises due to interference between two energy split states by using two different approaches to excite a single state and then both states. The first approach takes advantage of the polarised nature of the energy split states. Initially one branch is excited using a linearly polarised pump to show how Zitterbewegung is no longer present in the trajectory of the resulting propagating highly photonic polaritons. Photons are then injected with the same wavevector but now circularly polarised in order to excite both energy split states, showing the manifestation of Zitterbewegung in the trajectory. The second approach is to vary the degree of resonance with the energy split states by changing the wavevector of the injected photons at a fixed energy. The clarity of the Zitterbewegung oscillations in the trajectory is shown to increase and decrease depending on the degree of overlap between the reciprocal spot and the two states. This work then shows how the period and amplitude can be tuned by varying the energy and incident angle of the initial excitation conditions. This is done by exciting different regions along the LPB where the magnitude of the energy splitting is varied to show the inverse relationship between the period relative to the energy splitting. It also shows a similar dependency for the amplitude with less clear results. These results also take into account the effect of cavity birefringence on the value of the energy splitting between the TE-TM modes and its subsequent consequences on the amplitude and period of the Zitterbewegung. This work also shows how, by taking advantage of the tunable band structure presented by etched micropillar lattices, observation of Zitterbewegung with a smaller period but still observable amplitude is achievable.

All the work presented has at least a semi-quantitative agreement with simulated trajectories of photons injected under the same experimental parameters with excellent agreement for the simplest cases where energy splitting between the linear polarised branches is well defined. Whilst brief observations of the polarisation domains that manifest along the trajectory are presented, a more thorough study in this regard is needed to attain a full understanding of their relation to the period and amplitude of Zitterbewegung oscillations.

Chapter 5

Direct excitation of highly localised states in a 2D Lieb lattice

5.1 Introduction

With the predictions of their existence nearly 40 years ago[152], flat band energy systems have since been of great interest in the field of many-body physics and have provided a platform for the research of effects such as fractional quantum Hall phases[1], Wigner crystallization [2], negative magnetism [3] and disorder induced topological phase transitions [4]. As with many areas of solid-state physics, these flat band states can be simulated using engineered periodic potentials, with photonic flat band states observed in multiple lattices structures such as honeycomb lattices[107] and Kagome lattices[153]. However, perhaps the lattice most synonymous with flat energy bands is the Lieb lattice, a square lattice previously studied for its topological non-trivial phases inside and outside of photonics[154–157].

The non-dispersive nature of flat band energy states provides the main ingredient for the study of compact localised states (CLSs), states of very high localisation with little to no spread across the lattice sites away from the sites of initial formation. This localisation and lack of lattice spread is due to the implied infinite effective mass for particles occupying flat band states, this property consequentially quenches any kinetic energy terms and severely hinders particle mobility across the lattice.

The study of CLSs in photonic lattice systems requires a relative ease of access to the optical information of states within the lattice and whilst previous work has experimentally confirmed the presence of such CLSs in the flat band of Kagome lattice coupled waveguide arrays[153], an alternative approach to observations and study of these CLSs is also possible using etched lattice microcavity polaritons. This was experimentally confirmed for the case of a 1D Lieb lattice in 2019 by V. Golbot et al.[158], however, there is yet to be a demonstration in the 2D Lieb lattice as presented in this chapter. This candidacy is owed to the relative ease at which optical information within the lattice can be garnered via PL experiments, allowing direct measurements of properties such as effective mass and changes in spatial distribution. The inter-particle interactivity of polaritons also allows the potential study of non-linear CLSs, relying on the well-studied renormalization of the polariton dispersion under high power resonant excitation. Previous work has already shown, that by capitalising on polariton self-interaction, it is possible to facilitate the non-resonant condensation of polaritons into flat-band states on a 2D Lieb lattice[105]. This is followed by the study of lattice spin-orbit coupling and observation of pseudospin textures in the real space emission.

The work presented in this chapter concerns the direct resonant excitation of the localised flat band states in 2D Lieb lattice and then later introduces non-linearity to the formation of these CLSs. This work is inspired by proposals that flat bands such as those found in the Lieb lattice dispersion can support linear and non-linear compact localised states in Refs.[159, 160]. Whilst there is no real question of whether direct excitation of CLSs in 2D Lieb lattices for the linear regime is possible, this work experimentally confirms it whilst providing an effective and repeatable approach for their creation in similar etched micropillar lattices.

In the linear regime direct resonant excitation of a CLS is achieved using heavily patterned spots, phase matching and careful tuning of the laser energy to match the characteristic real space micropillar emission profile of the S flat bands. The work then moves on to present the attempts to create a non-linear CLS using similar approaches with clear non-linearities observed in the intensity of emission when increasing the incident power. These non-linearities are initially observed for single micropillar excitation for the P flat band states and later full a non-linear CLS is observed for the S flat band states with bistable behaviour also observed in this case. Quantification of the lattice spread is calculated using methods of comparing contrast and using the inverse participation ratio (IPR). High localisation is observed in cases when efficient direct excitation of the flat band occurs in both the linear and non-linear regime. In the linear regime the CLS is calculated to have an IPR of 0.14 compared to a maximum possible IPR of 0.25. In the non-linear regime the CLS is calculated to have an IPR of 0.19.

The realization of both directly excited linear and non-linear localised states in a 2D Lieb etched micropillar lattice helps pave the way for the use of this relatively simple to fabricate platform in the quantum simulation of many-body flat band models in an environment allowing high control and tunability of important parameters along with direct access to the polariton wavefunction.

The work experimental work presented in the following chapter was carried out by myself with support from Dr Paul Walker. I built and took all measurements and the processed the data. D Paul Walker assisted with the taking of some measurements and wrote the code for the SLM holograms.

The structure of this chapter is as follows:

Section 5.2: A description of the sample used in this chapter followed by a description of the two main experimental configurations used in the rest of the work presented in this chapter.

Section 5.3: A description of the method used to directly excite a CLS in the linear regime with two potential alternative approaches presented and a brief description of why one is unsuitable using the equipment available during the work presented in this chapter. This is then followed by the results and discussion of the second approach.

Section 5.4: A description of the methods used to directly excite a non-linear CLS using several different approaches along with the discussion and presentation of the results for each approach. First the same approach as in section 5.3 is used with a presentation and discussion of results and an explanation for its subsequent failure. Then a description of an approach to excite a single micropillar and it results are presented and discussed. Following this, the successful approach using a cigar shaped spot to create a full non-linear CLS is described and its results presented and discussed.

Section 5.5: Two different methods to quantify the lattice spread are described with the results presented.

Section 5.6: Conclusions for the work presented in this chapter are drawn.

5.2 The 2D Lieb lattice

5.2.1 Lattice structure and flat band formation

The 2D Lieb lattice is a square lattice array that consists of three square sublattices, designated A, B, and C, with each sublattice contributing one atom to the unit cell. In a micropillar lattice, these sublattices are represented by individual but overlapping micropillars, which allow for hopping of the photonic modes.
The band structure of the Lieb lattice's dispersion contains two prominent flat bands at different energies, which can be determined through the Bloch theorem using the periodic potential imposed by the Lieb configuration, as discussed in subsection 1.6.3. The lowest in energy of these is the S flat band which located within the S dispersive bands. These dispersive bands correspond the lowest discrete energy states within the micropillars. The second flat band is named the P flat band located in the P dispersive bands corresponding to the second lowest discrete energy states within the micropillars. The S and P bands are separated by a forbidden energy region, the size of which depends on depth of etching to create the micropillars.

5.2.2 Compact localised states in the Lieb lattice

The lack of curvature in the flat bands on the dispersion implies an infinite effective mass for polaritons occupying these states which manifests as a quenched

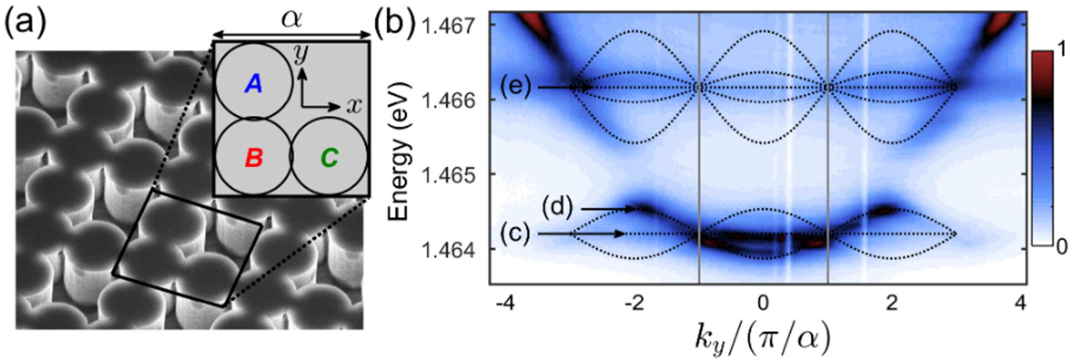

Figure 5.1: (a) Scanning electron microscope image showing a section of the 2D Lieb lattice. The enlarged image shows a diagram of one unit cell and the three sublattices labelled A, B and C. (b) Lieb lattice dispersion measured under low-power non-resonant excitation. The white dotted lines indicate the bandstructure as calculated using a tight binding model. Sub-labels (c) and (e) on this image denote the *S* and *P* flat bands respectively. This dispersion is taken on the same sample but for a slightly different device to that which is used for the work in this chapter. Sub-label (d) has no relevance to this thesis and may be ignored. Taken from [161].

kinetic energy term and thus a vanishing group velocity. Consequentially, wave transport is completely suppressed and thus at flat band energies there is the emergence of strongly localised states. When considering real space emission, these localised eigenstates only span a few lattice sites and form a CLS. A condition for the formation of a CLS in a lattice is the destructive interference at particular sites, something that holds true for the Lieb lattice. For such a lattice topology, where sites in different sublattices have different connectivity, localised states may reside on the flat bands[162] which is manifested as emission from the A and C sites in each unit cell only. For the Lieb lattice, and in the framework of the tight binding model and the consideration of nearest neighbour hopping, the characteristic destructive interference occurs at site B from modes hopping from the A and C sites. Thus, polaritons that initially occupy sites A and C at an energy matching that of the flatbands remain localised and non-dispersive. It is important to note the π phase difference between the states in the A and C sites for a CLS, a condition for destructive interference between hopping modes on site B.

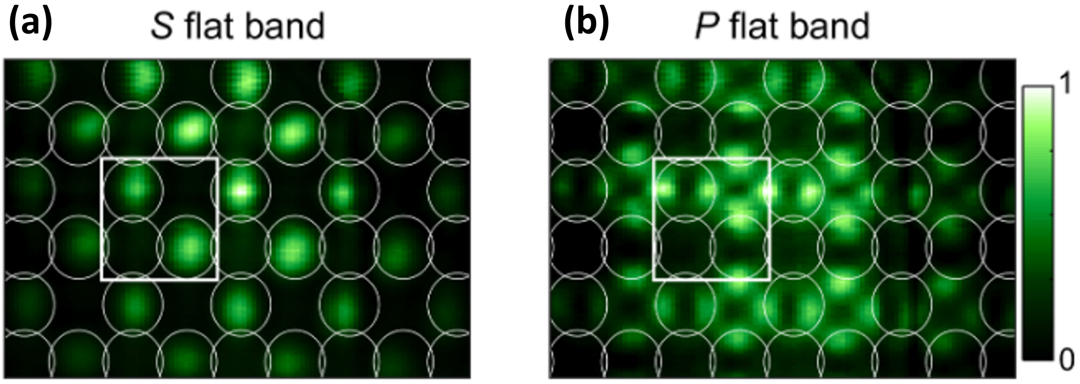

Figure 5.2: (a) Emission profile in real space at the energy of the *S* flat band in a Lieb lattice.(b) Emission profile in real space at the energy of the *P* flat band in a Lieb lattice. Taken from [161].

Research on the emission characteristics of CLS states in the 2D Lieb lattice has revealed distinct polarisation patterns, with increased vertically polarised modes detected at the A sites and increased horizontally polarised modes at the C sites (relative to the sample reference frame)[105]. This polarisation disparity can be attributed to the polarisation dependence of tunnelling rates with respect to the hopping direction. Specifically, modes that are polarised perpendicular to the hopping direction exhibit significantly lower probabilities of tunnelling, $\tau_{\perp}$, than those that are parallel, $\tau_{||}$. Such that

$$\tau_{||} > \tau_{\perp}. \tag{5.1}$$

As an example, a horizontally polarised mode at an A site is less likely to tunnel to the B site compared to a horizontally polarised mode at the same site and vice verse for the C sites. A visualisation of this can be seen in Figure 5.3 below.

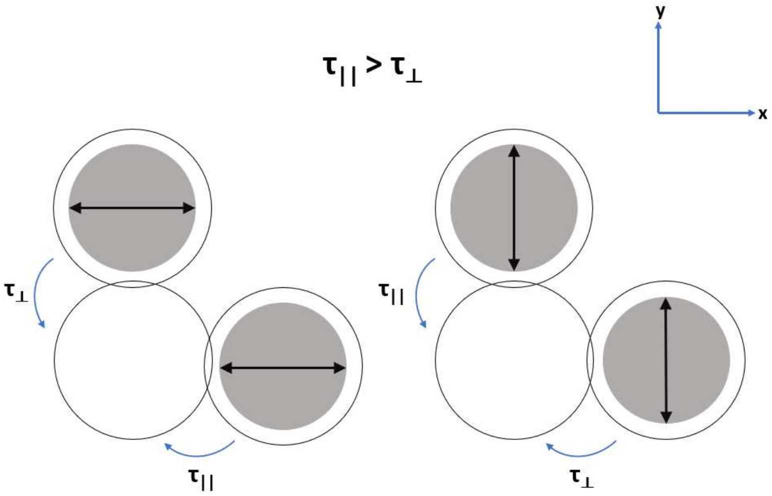

Figure 5.3: A visualisation showing the probability of different polarised modes hopping to the B sites from their respective site.

Since only like-polarised modes will destructively interfere at the B sites, the population of vertically polarised modes increases to compensate for the difference in tunnelling probability. The situation is similar but inverted for the C sites, resulting in a greater population of polaritons at each site for polarisations that are perpendicular to the hopping direction to the B sites.

As Figure 5.2 shows the spatial distribution of emission in real space differs for S flat band CLS formation compared to the P flat band. For the S flat band, a single emission lobe from the full pillar is observed whereas in the case of the P flat band the emission from a single pillar is separated into two lobes. The emission from the A sites is dominated by the emission from the P_y orbitals whereas the emission from the C sites is dominated by emission from the P_x orbitals (subscript represent axis for which the lobes lie parallel). Whilst such orthogonal modes will not destructively interfere at the B site, the lower populations of orbitals parallel to the hopping direction to site B is offset by the aforementioned difference in tunnelling probabilities.

5.3 Experimental parameters and configuration

5.3.1 Sample description

The Lieb lattice sample used in this work consists of AlGaAs/GaAs micropillars of 3μm diameter and separation of 2.85μm. The lattice periodicity is a=5.7μm. The resulting dispersion at k_x=1.7 um^{-1} for this device can be seen in Figure 5.4. The centres of the non-dispersive S and P flat bands are located at around 1.469 eV and 1.4718 eV respectively, whilst the S and P dispersive bands surrounding them are present but barely visible in the image (due to their dependence on k_x. These dispersive bands are more visible at dispersions for different values of k_x. The S and P flat bands are separated by an energy of approximately 2 meV whilst the forbidden energy region between the bottom of the P dispersive bands and the top of the S dispersive bands is approximately 0.7meV. The linewidth, γ, of both flat bands is $\gamma \approx 280\mu$eV.

5.3.2 Spatial light modulator configuration

This chapter uses the transmission configuration, explained in subsection 2.1.4, as a base configuration, with the laser incident on the non-etched side of the sample. To achieve a Laguerre-Gaussian shaped spot and to directly match the emission profile of the S flat band CLS directly, a spatial light modulator (SLM) is utilized, as described in subsection 2.3.2. A waveplate is first introduced to align the incident polarisation with the optical axis of the SLM, followed by a beam expander to improve the resolution of the patterned laser spot. The close proximity of individual micropillars makes this step especially critical in the case of directly matching the emission profile. After the SLM, another waveplate is used to create circularly polarised light followed by a spherical lens in order to increase the angular separation between the zero and first order diffraction beams.

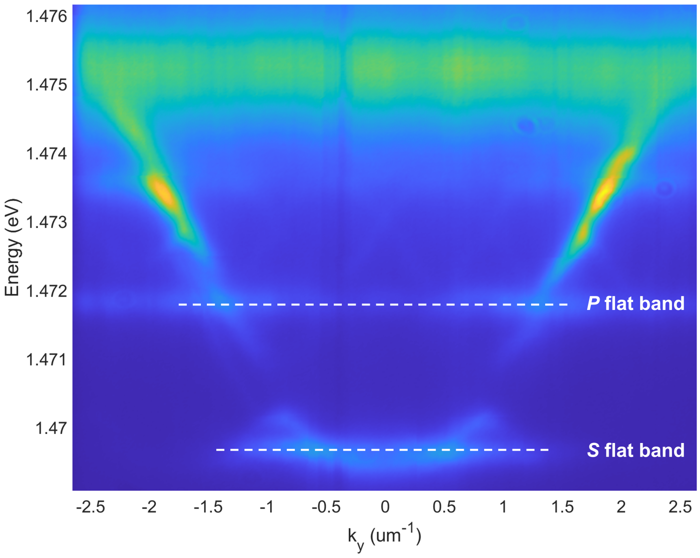

Figure 5.4: PL dispersion experimentally obtained using angle resolved spectroscopy for the same lattice used for the work in this chapter at k_x=1.7 um^{-1}. The S and P flat bands are labelled.

The position of the SLM is such that the first order diffraction beam is aligned along the optical path. Past the focal point of the lens an iris is used to spatially filter out everything but the first order diffraction beam. The beam is then recollimated by a different lens and directed to the excitation objective and focused onto the sample with circular polarisation.

Holograms can be applied to the SLM display using Matlab and an HDMI connector to the SLM driver, and the control over the spatial patterning and phase distribution of the spot lies in the Matlab code used to generate the hologram. It is essential to use steep angle incidence for light on the SLM to avoid deformation of the patterned spot at shallower angles.

5.3.3 Cylindrical lens configuration

For the work involving the non-linear excitation of full CLSs at the S flat band energy, limitations in the required incident laser power are created by the use of the SLM. To remedy this, cylindrical lenses replace the SLM to create a so called 'cigar shaped spot' in order to allow excitation of two C sites only. These lenses act to expand the spot in the y-direction whilst compressing it slightly in the x-direction at a ratio of 4:1. With the SLM removed, the collimated beam is passed through two cylindrical lenses placed orthogonal to each other in the sample plane (in order to act on the x and y components of the beam independently). Due to the differing focal lengths of these lenses, they are placed such that they have a shared focal point. Confocal to the shared focal point, another spherical lens is used to recollimate the now elliptical beam. The beam is then guided to the excitation objective and focused onto the sample in the form of a cigar shape. Further details of this excitation configuration on the lattice are described in subsection 5.6.3.

5.4 Direct resonant excitation of a *S* flat band linear CLS

5.4.1 Description of SLM patterned approach for the *S* flat band in the linear regime

In order to directly and efficiently excite a S flat band CLS in the Lieb lattice, the incident laser spot must excite the pillars corresponding to the emission profile seen in Figure 5.2 for a small collection of unit cells. The most obvious choice for these pillars is a square shape consisting of four unit cells, this means the excitation of four pillars in total (two A sites and two C sites with phase difference of π) and destructive interference at two B sites. Recent proposals suggest using a Laguerre Gaussian shaped spot to achieve this[163]. Whilst the inherent phase winding of this spot makes it highly suitable, attempts to create this shape for the work in this thesis results in poor uneven intensity distributions across the spot, this is in part due to the difficultly in aligning the spot with the SLM however even with precise alignment this effect could not be mitigated. The hologram and resulting spot on the sample in this case are shown in Figure 5.5.

An alternative approach to exciting the desired micropillars is to directly pattern the spot to match the emission profile from the two A and C sites. Such patterning can again be achieved by the SLM with fine control over the power, phase and position of the individual spots. This approach is similar to those used in previous studies for CLSs and simply involves matching the phase and position of each individual spot with that of the specific site in the emission profile. In

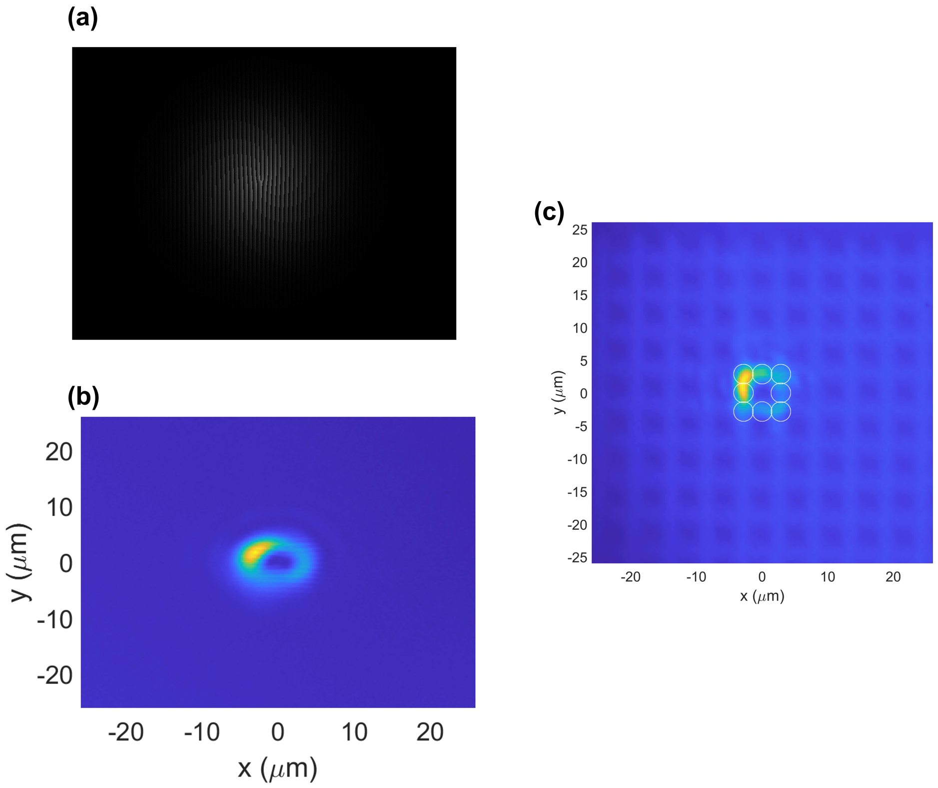

Figure 5.5: (a) Hologram displayed on the SLM to pattern the incident beam with a Laguerre–Gaussian profile. This image is cropped for the purpose of this figure. (b) Resulting Laguerre–Gaussian shaped spot focussed on the planar region of the sample. (c) Laguerre–Gaussian now focussed on the Lieb lattice on the sample. The white circle denote the approximate locations of the pillars for the four unit cells concerned.

this configuration, the individual spots are aligned with the sites through the substrate of the cavity and coupled into the micropillars. The resulting emission can then be guided to the CCD from the etched side of the sample. The hologram and spot pattern in free space using this approach can be seen in Figure 2.13 (c-d) respectively. It is important that the energy of the pump laser is carefully tuned to be resonant with the S flat band energy and with sufficiently low power (less than 50mW) to avoid any sample heating effects. If performed successfully, this will allow efficient injection of photons in the flat band polariton states with the formation of a CLS in the real space emission profile.

5.4.2 Results and discussion of SLM patterned approach for the S flat band in the linear regime

The four spots are aligned with the corresponding pillars whilst the energy is tuned to the energy of S flat band at 1.469 eV. The resulting emission from the pillars is guided to the CCD and with results of this shown in Figure 5.6.

As can be seen, the emission is highly localised with no emission from the B sites indicating the signature destructive interference. The spreading emission seen around the CLS can be explained by slight mismatch between the pillars and spot alignment leading to some coupling into different unit cells. This may also be caused by small scattering by optics in the excitation path leading to photons incident elsewhere on the sample. Another explanation lies the proximity of the flat band to the dispersive bands in the dispersion of the Lieb lattice which may lead to some small excitation of the latter allowing weak spreading across the lattice. This is made even more likely by the relatively broad line width of the flat band in this sample.

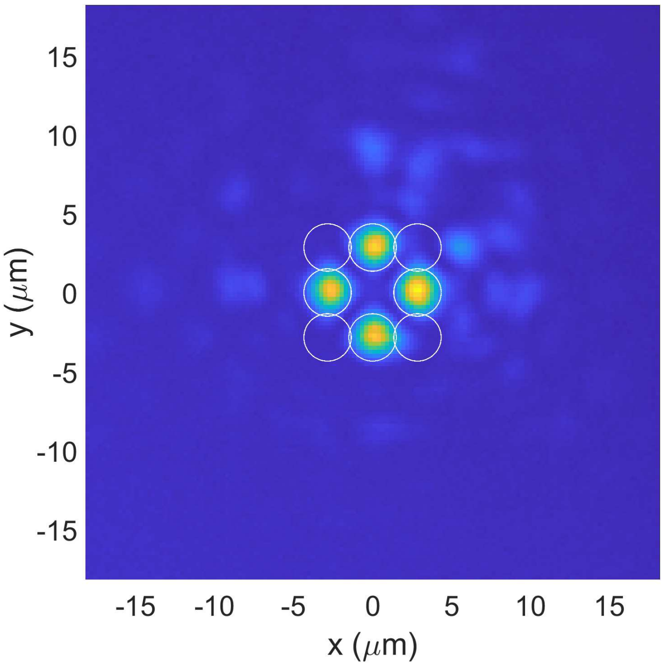

Figure 5.6: Linear CLS on the 2D Lieb lattice using the emission matching approach described in subsection 5.5.1. The white circles denote the approximate positions of the micropillars in the four unit cells concerned.

5.5 Direct resonant excitation of a non-linear S flat band CLS and renormalization of P flat band

5.5.1 Description of SLM patterned attempt for the S flat band in the non-linear regime

After demonstrating linear excitation of a CLS in the S flat band in section 5.4, the next step is to introduce non-linearity to the CLS. This relies on the renormalization (blueshift) of the polariton dispersion observed at high polariton densities. The first attempts at introducing this non-linearity involve repeating the experiments performed in section 5.4 but now detuning the laser above the top of the flat band energy with a value of $\Delta E \approx 1/2\gamma$ and gradually increasing the incident laser power. If performed correctly, when the laser power reaches some threshold, the dispersion (and thus flat band) will blue shift towards the laser and efficient excitation of the flat band will occur. In real space this will look like a sharp non-linear increase in emission intensity across the threshold from the A and C sites along with a decrease in intensity from the B sites. Initially, when detuned above the flat band at low power there is excitation of the dispersive bands meaning that that the states will not be highly localised. As the power increases renormalization will occur, and the excited states will once again have a vanishing group velocity and further spreading will cease.

5.5.2 Results and discussion of SLM patterned approach for the *S* flat band in the non-linear regime

First this method is attempted using the emission profile matching approach as in the case of for the S flat band. This time measurements are taken at intervals of ΔE relative to the S flat band and at each interval power dependencies are performed. Figure 5.7 shows the result of these attempts for the S flat band.

The increase in intensity from the right hand pillar when increasing power remains linear. The same is true for all of the pillars at all the values of ΔE from the S flat band that are measured (for the apparent non-linearity in top pillar see end of this subsection). This implies that renormalization of the S flat band has not occurred. The emission still has a very similar profile to the linearly excited CLS, this is in part due to the small value of detuning from the flat band energy, since there is still considerable excitation of the flat band states. At larger detunings the emission profile changes somewhat to include emission from B sites due to excitation of the dispersive bands and less efficient (if any) excitation of the flat band.

The linear increase in emission intensity from the micropillars can be explained

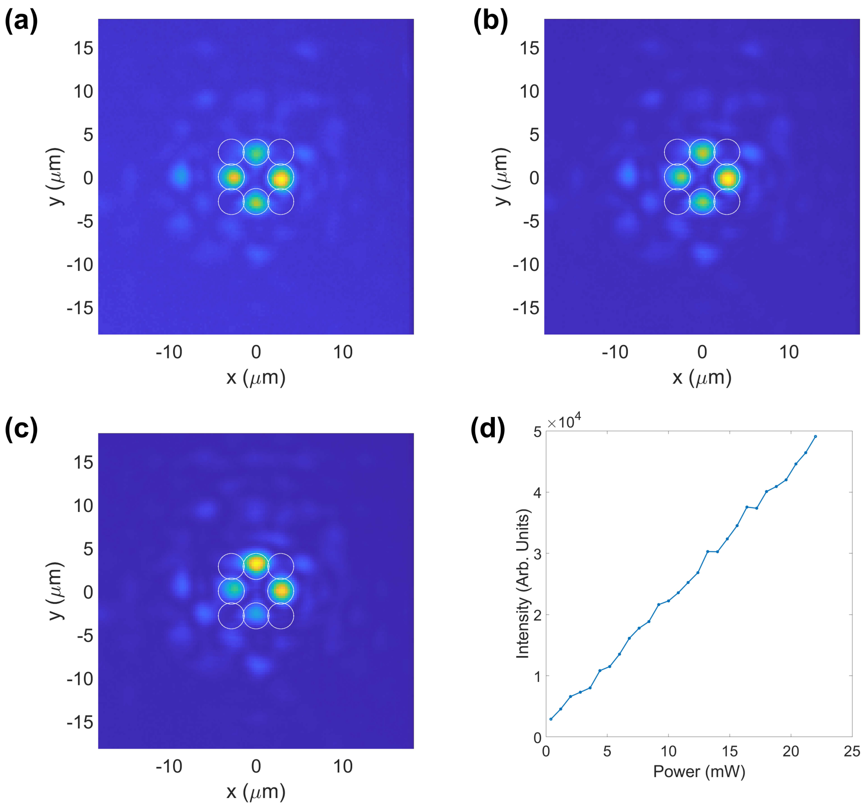

Figure 5.7: (a-c) Emission profile when laser is detuned $\Delta E \approx 1/2\gamma$ above the S flat band energy with a laser power of 6 mW, 14 mW and 22 mW respectively. (d) Full power dependency including the measurements in (a-c) for the right hand micropillar.

when considering the power per spot in the pattern along with the effects of sample heating. In order for the renormalization of the polariton states to occur in each micropillar, the polariton density must reach a specific threshold. For the S flat band emission profile, the total laser power must be divided by four to calculate the power per spot. Without sample heating the power from the laser should more than suffice. However, when local heating occurs on a sample, the dispersion will redshift away from the laser energy countering any blueshifting that may occur. Since the power density increases quadratically as the spot diameter decreases, the very small spots (≈ 3 μm) incident on each micropillar impart a significant power density and thus cause a large amount of local heating.

The result of this is a larger redshift the higher the polariton density preventing any renormalization of the S flat bands. A remedial approach to these effects are discussed in the next subsection.

At almost maximum power, the emission intensity of the top pillar shows a potential non-linearity. However, since higher power cannot be achieved with this approach, this cannot be explored further. The non-linear threshold for this pillar starts at approximately 0.5 mW below the maximum achievable power. The reason for this behaviour occurring only in a single pillar may be due to variations in the individual spot positions on each pillar, with the spot incident on the top pillar coupling slightly more efficiently than the others. In fact, it is well established that non-linearity occurs more readily when the incident laser is slightly offset from the centre of the pillar in some cases[101].

5.5.3 Description of excitation of single micropillar approach for the *P* flat band

To counter the redshift of the flat bands due to the sample heating several adaptations to the previous approach are made. Firstly, an electro-optic modulator (EOM) is included in the excitation path. The details of this device are discussed in subsection 2.3.1. Secondly, the SLM is no longer used to allow for excitation of a single micropillar. This will allow for a greater laser power incident on the micropillar since the total power is no longer shared between multiple spots. Even though the power density per pillar is now increased, the extra sample heating can be offset by the EOM. Lastly, the focus of the measurements will now concern the P flat band. Due to the more excitonic nature of these polariton states, a stronger inter-particle interaction strength is present and thus the threshold for non-linearity will be lower. These adaptations will reduce sample heating and the non-linearity threshold along with allowing greater laser power to be incident on the pillar, all of which should facilitate observation of any non-linearity due to the renormalization of the flat band states.

To increase the coupling efficiency into the micropillar, the P state emission profile is matched by introducing a phase mask in the excitation path. This will pattern the spot slightly to create two individual lobes with a π phase difference as observed in the P flat band emission (See Figure 5.2). Since this approach involves the excitation of a single micropillar, formation of a full CLS is not expected, rather this approach is used to confirm renormalization at the flat band energies and to determine the parameters for non-linearity such as required power and values of ΔE

.

5.5.4 Results and discussion of the excitation of a single micropillar approach for the P flat band

The real space emission from a single micropillar (A site) for different powers when the laser is detuned $\approx 1/2\gamma$ above the top of the P flat band are shown in Figure 5.8 using the approach described in the previous subsection.

The intensity from the micropillar shown in Figure 5.8 is plotted against the increasing power as shown in Figure 5.9.

A clear non-linear increase in emission intensity is observed when exciting the pillar with a laser incident power between 20-25 mW and energy detuning of $\Delta E \approx 1/2\gamma$ above the top of the P flat band. Whilst this single micropillar flat band state is not a full non-linear CLS, it provides a significant step in showing such flat bands can support these states.

A typical behaviour observed in non-linear polariton states is that of bistability. The signature of this effect is the hysteresis curve that is observed when approaching the non-linear threshold from above and below in incident power. The non-linear P flat band state observed in this subsection also exhibits this behaviour with the hysteresis curve shown in Figure 5.10.

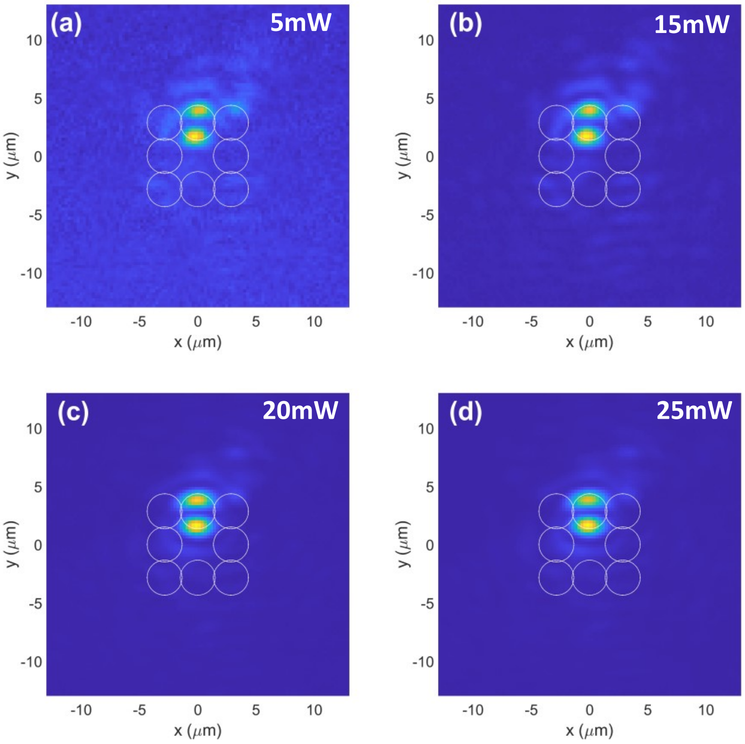

Figure 5.8: (a-d) Real space emission profile when laser is detuned at a value of $\Delta E \approx 1/2\gamma$ above the top of the P flat band energy with a laser power of 5 mW, 15 mW, 20 mW and 25 mW respectively.

5.5.5 Description of the cigar shaped spot approach for the S flat band

Whilst non-linearity has now been observed for a P flat band state, the case for the S flat band states is yet to be observed along with observation of a full non-linear CLS. The former is due to the higher non-linear threshold that is expected for polaritons states in the S flat band. Since the excitonic content is lower for these polariton states the inter-particle interaction strength is reduced for similar polariton densities when compared to the P flat band states. Also, the single micropillar approach used in the previous section will induce too much sample

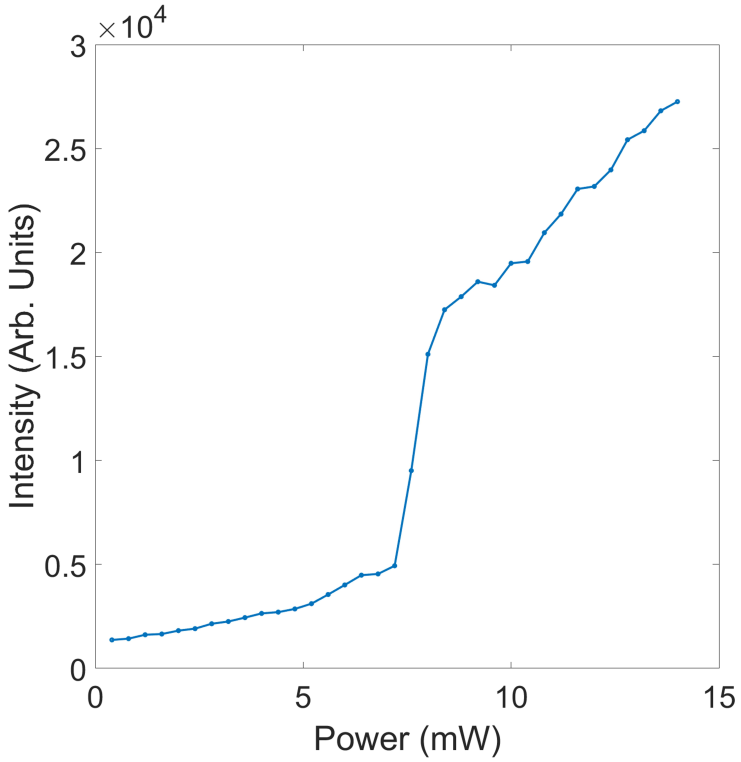

Figure 5.9: Emission intensity vs incident laser power for the micropillar shown in Figure 5.8. Non-linearity is observed beginning around 20 mW and ending around 23 mW.

heating in the case of the S flat band, more so than can be offset by the EOM. To counter this and also to allow creation of a full non-linear CLS, the spot is shaped using two cylindrical lenses to produce a so called ”cigar shaped” spot i.e. the spot is given a high degree of ellipticity. This approach reduces the power density compared to the small Gaussian spot used in the previous section and also allows excitation of two micropillars at the same time, namely the two C sites across two neighbouring unit cells in the y-direction. A schematic for this excitation approach is shown in Figure 5.11

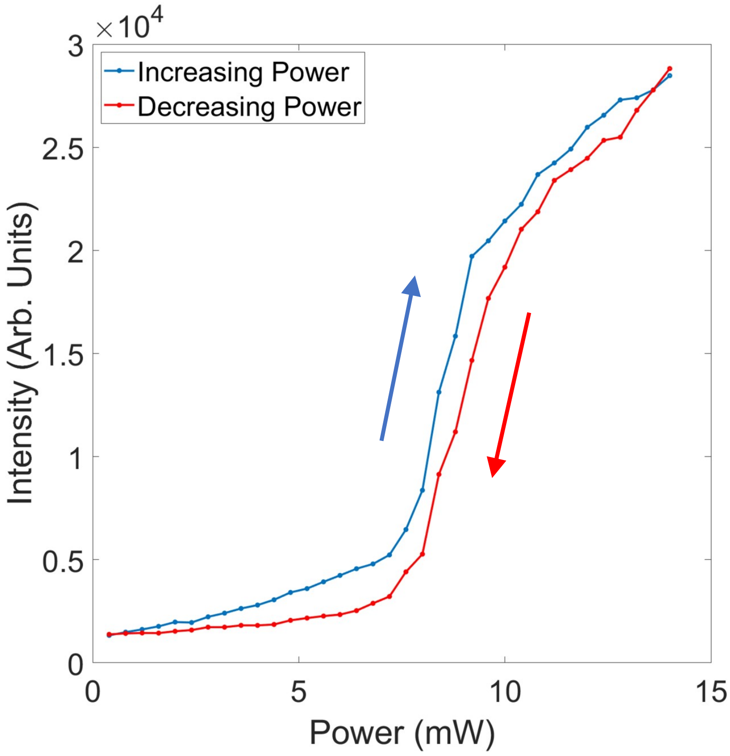

Figure 5.10: Bistable non-linear behaviour observed when plotting emission intensity vs incident laser power for the single micropillar shown in Figure 5.8. The blue line denotes the relationship when increasing power (approaching threshold from below) whilst the red line denotes the relationship when decreasing power (approaching the threshold from above).

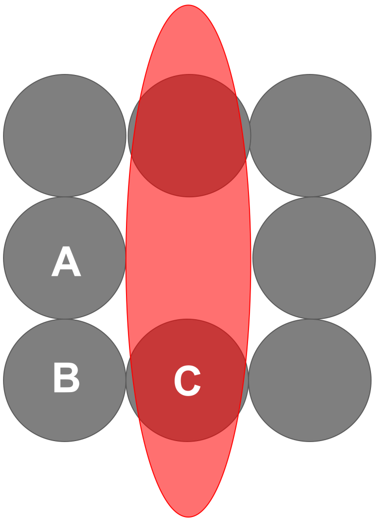

Figure 5.11: Simplified schematic showing the excitation configuration using the cigar shaped spot to excite the two C sites. The red ellipse represents the laser spot incident on the sample in transmission configuration (non-etched side of the sample).

5.5.6 Results and discussion of the cigar shaped spot approach for the S flat band

Using the cigar shaped spot configuration, power dependencies are performed at various detuning levels above the S flat band energy with a vertically polarised excitation laser. As with all other approaches the real space emission profile is recorded by the CCD at each power interval.

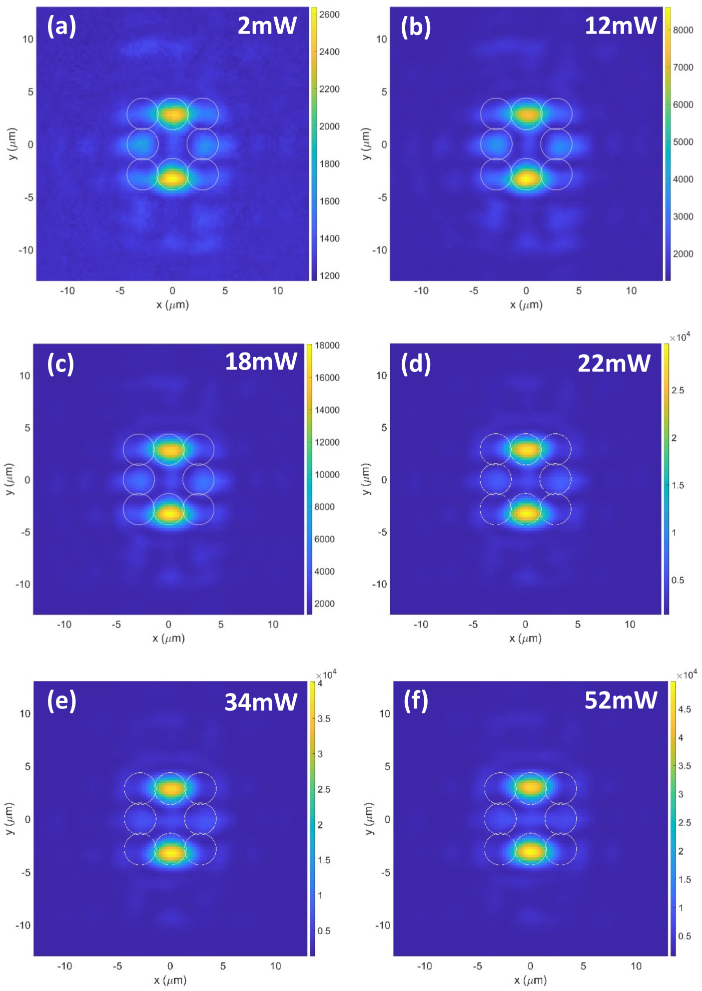

Figure 5.12: (a-f) Real space emission profile for different powers when exciting the C sites of 2 unit cells using cigar shaped laser spot in transmission configuration with an value of $\Delta E \approx 1/2\gamma$ above the centre of the S flat band energy . The respective incident powers are labelled on each image.

As before, the emission intensity from the centre of the pillars is plotted against the respective powers as shown in Figure 5.13.

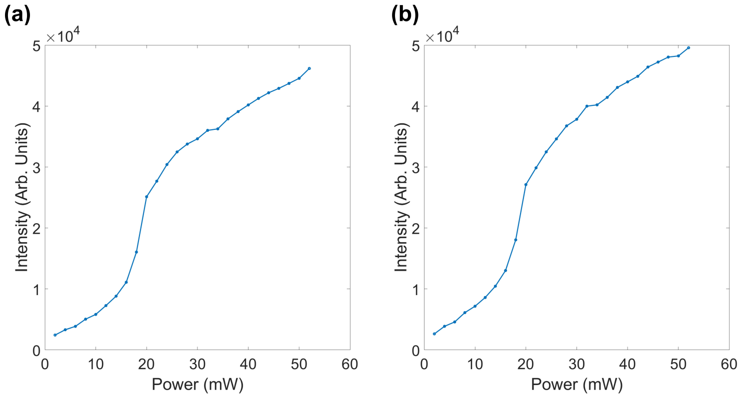

Figure 5.13: (a) Emission intensity vs incident laser power for top pillar shown in Figure 5.12. Non-linearity is observed beginning around 16 mW and ending around 20 mW. (b) The same as in (a) but for the bottom pillar shown in Figure 5.12.

Clear non-linearity is observed in both C site micropillars when increasing the incident laser power, with the threshold located between 16 mW and 22 mW in both cases. After the threshold the intensity clearly increases linearly once more, indicating the S flat band states are now being efficiently excited after renormalization.

The real space emission shown in Figure 5.12 shows the characteristic emission profile of CLS at powers above the threshold with the lack of emission from the B sites. As the power increases further above the threshold, the maximum efficient excitation of the flat band is approached and the emission from the B sites remains very low along with a clear reduction in spread across the lattice, indicating destructive inference is occurring for photons that hop to the B sites. At low powers before the threshold, the emission profile can be described as flat-band like, with a mixture of emission from the inefficiently excited flat band states along with emission from the dispersive band states. At higher powers, above threshold, the flat band emission profile clearly manifests. At all powers, emission is seen from the A sites, even though there is no incident laser on these sites. This emission is due to the hopping of injected photons from the C sites via the B sites. The differing emission intensities between the A and C sites indicates a differing polariton population, explained by the fact the laser has a vertical polarisation and a lower tunnelling probability from A sites to B sites for vertically polarised modes. The emission seen in the centre of the unit cells is the leakage and consequential hopping of photons through the air-GaAs interface of the micropillars into the opposite A or C site.

Whilst it is shown experimentally that the 2D Lieb lattice can in fact support linear and non-linear CLSs, it is useful to quantify the spread of the states to give an idea of the degree of localisation in each case. This acts to further support the fact that a CLS has been created in each case.

5.5.7 Quantification of the lattice spread and estimation of tunnelling ratios

Whilst Figure 5.12 shows a decrease in spreading relative to the CLS across the surrounding unit cells as the S flat band renormalizes, this can be quantified by selecting surrounding micropillars and using the equation for peak to peak contrast to compare how localised the states become above and below threshold. The initial excited micropillar can be used as a reference point to define the location of a different micropillar. For the case where the top C site micropillar in Figure 5.12 is given the coordinates $x = 0$ and $y = 0$ such that its intensity is denoted $I_{x0,y0}$, the emission from a different micropillar in a neighbouring unit cell can be given intensity $I_{x1,y1}$. The normalized contrast, C, then becomes

$$C = \frac{I_{x0,y0} - I_{x1,y1}}{I_{x0,y0} + I_{x1,y1}}. \tag{5.2}$$

The contrast is then calculated for two different micropillars in the surrounding unit cells relative to the top micropillar in Figure 5.12. These new micropillars are denoted by a red circles in Figure 5.14 along with the change in contrast over the power sweep.

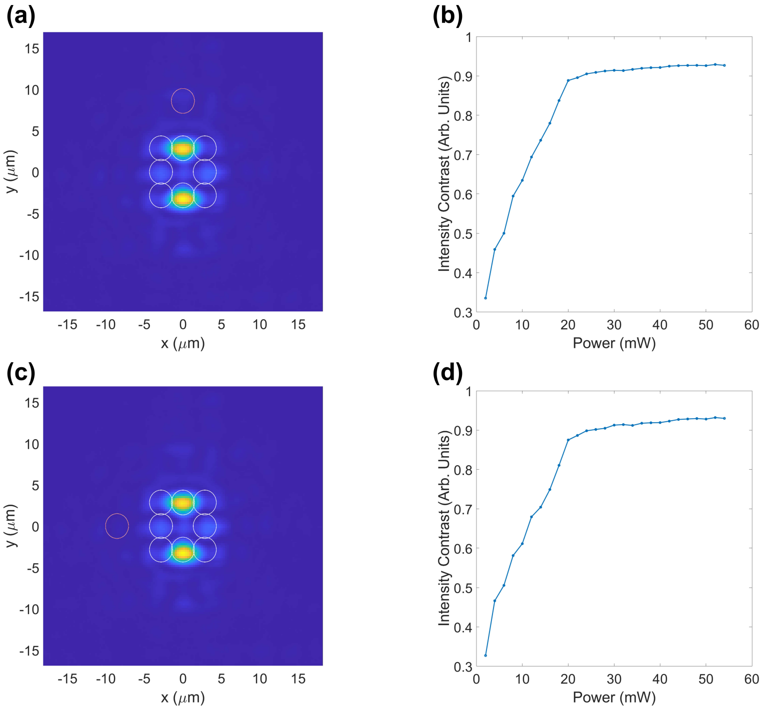

Figure 5.14: (a) The same as in Figure 5.12 (f) but now with a red circle denoting the position of the micropillar for which the contrast is being calculated against. (b) The corresponding contrast between the top micropillar and the micropillar denoted by the red circle in (a) at each power interval for the scan shown in Figure 5.12. (c) The same as in (a) but the red circle now denotes the location of a different micropillar. (d) The same as in (b) but corresponding the top pillar and the pillar denoted by the red circle in (c).

The same can be done when using the bottom micropillar in Figure 5.12 and now labelling its emission intensity as $I_{x0,y0}$, returning very similar results as those for the top micropillar. These results show a sharp plateau in the contrast after the non-linear threshold is reached, indicating that once renormalization occurs, spreading across the lattice stops decreasing. This increase then sudden plateau can be explained when considering the following; as the threshold is approached, the flat band blueshifts closer to laser allowing more excitation of the flat band states and the real space emission become more CLS like, thus increasing the localisation (and by extension the contrast). After the threshold, the flat band has fully renormalized with the laser and a CLS is formed meaning maximum localisation is attained. It is worth noting that, Figure 5.14 (b and d) does show a small gradual increase in contrast after the threshold, an explanation for the same effect seen when calculating the inverse participation ratio below is given later in this subsection.

Whilst directly comparing the contrasts between CLS and non-CLS micropillars provides an insight into spread across the lattice, it does not present a full picture and only represents the spread to specific micropillars. The spread across the lattice may have a degree of spatial anisotropy potentially due to slight deviations from normal incidence of the laser or due to polarisation dependant tunnelling rates. A more encompassing measure of quantification of the lattice spread is the inverse participation ratio (IPR). Originating from quantum mechanics to account for the uncertainty in state occupation for particles, in the context of microcavity lattice spread the IPR gives a measure of localisation of a state when considering a given number of sites, L, and is given as

$$IPR = \frac{\sum_n |\psi|^4}{(\sum_n |\psi|^2)^2}, \tag{5.3}$$

where n is the nth site being considered and ψ is the amplitude of the field inside the micropillar. Since amplitude of the field corresponds to the square root of the emitted intensity from the pillar, I, Eqn.(5.3) can be rewritten as

$$IPR = \frac{\sum_n |I|^2}{(\sum_n |I|)^2}. \tag{5.4}$$

The calculation of the IPR will return a value representing the degree of localisation for a CLS over L states, with an IPR equal to 1 indicating a fully localised state on a single micropillar and a fully delocalised state returning an IPR tending to 1/L.

Using Eqn.(5.4) to calculate the IPR for the case where the S flat band is excited linearly as in Figure 5.6 and considering 16 lattice sites including those expected in the S flat band emission profile, a value for the IPR is found to be IPR=0.14.

A visualisation of the 16 sites considered in this calculation can be seen in Figure 5.15. For a fully localised state in the case of four expected emission sites of equal intensity the IPR value will be 0.25. The difference of 0.11 indicates that full localisation is not completely attained. Several factors can be used to explain this non-perfect localisation. Firstly the measurements presented still contain some background noise such as CCD noise and laser scatter off optical components resulting in additional counts that will act to skew the measurements of localisation. Secondly, the fact that even at efficient excitation of the flat band, there is some undesirable excitation of the dispersive bands due to the relatively broad linewidth of the flat bands. This allows a small occupation of sites away from the CLS thus lowering the IPR value. Under ideal conditions a value very close to 0.25 for the IPR is achievable but would require a flat band of very narrow linewidth. For comparison calculation of the IPR for the case where the laser is detuned by $\Delta E = 3/4\gamma$ from the top of S flat band using the same experimental procedure and the same excitation power returned an IPR value of IPR=0.07.

The same method of lattice spread quantification can be used in the case of the non-linear CLS formation using the cigar shaped spot as in subsections 5.5.(5-6). In this case the IPR can be calculated for each power interval and plotted against the power to show how the degree of localisation changes over the non-linear threshold. It is expected that before threshold the localisation will be low and after renormalization, the IPR will be high and converge towards a value of high localisation when maximum efficient excitation of the flat band occurs. The results of this are shown in Figure 5.16.

The degree of localisation increase as the S flat band blue shifts towards the laser energy. After the non-linear threshold, when renormalization of the flat band with the laser has taken place the IPR plateaus indicating efficient excitation of the flat band states and true CLS formation with no further significant localisation taking place. The small increase in the IPR in this post-threshold region indicates maximum efficient excitation is not quite achieved yet. This is most likely due to the flat band constantly balancing between increasing blue

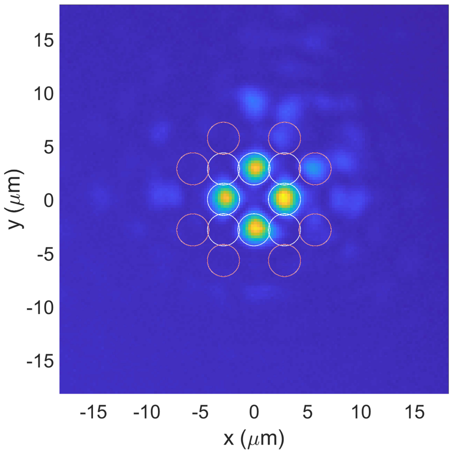

Figure 5.15: (a) The same CLS as shown in Figure 5.6 used the calculation of the IPR value. The white circles denote the unit cells being excited whilst the red circles denotes the 16 other pillars considered in the calculation of the IPR (L=16).

shift and red shifts (due to heating) with increasing power. An optimal power will likely exist where the balance between the two is optimised after which the red shift due to heating begins to overcome the blue shift and the IPR decreases again. At the highest powers the IPR is close to 0.2 indicating a very high degree of localisation. At the lowest powers the IPR is 0.065, comparable to the 1/16 value expected for a fully delocalised state. It is also worth highlighting that when comparing this value of 0.065 with the maximum IPR value of 0.196 the degree of localisation is seen to increase 3 fold.

As Figure 5.16 shows, the intensity at the A and C sites differs, in fact it is observed that the intensities of the A sites and C sites increases at a different rates with power. This change in contrast between the two A sites and two C sites in the CLS is plotted against power in Figure 5.17.

This changing in contrast between the A and C sites can once again be explained by the polarisation dependant tunnelling rates and the requirements of destructive interference at the B sites. As the IPR tends towards full localisation the

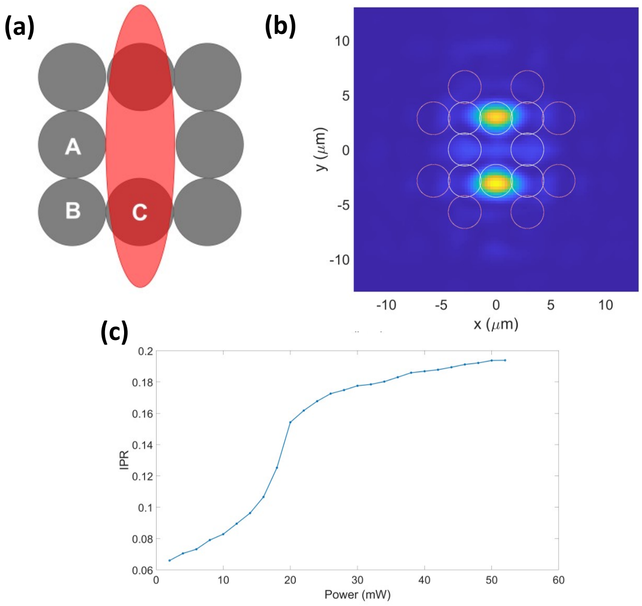

Figure 5.16: (a) The cigar shaped excitation profile used for the CLS in (b). (b) The same CLS as shown in Figure 5.12 (f). The white circles denote the unit cells where CLS emission profile is expected (including the zero emission B sites) whilst the red circles denotes the 16 other pillars considered in the calculation of the IPR (L=16). (b) The IPR values plotted against the power showing the change in localisation over the non-linear threshold.

populations at the A and C sites tend towards those expected for a fully localised state, more specifically they tend towards the ratio of the tunnelling probabilities for horizontally and vertically polarised states. For a fully localised state in a Lieb lattice that ratio has been estimated to be 6:1[105] meaning that the populations of states with a polarisation perpendicular to the hopping direction is 6 times larger than that of states with a polarisation parallel to the hopping direction at either the A or C sites. In the case of the measurements described and shown in subsections 5.5.(5-6), the excitation polarisation is vertical in the lab frame (and sample frame), thus emission is also expected to be vertically polarised meaning, for a fully localised state, the intensity of emission from the A sites is expected to

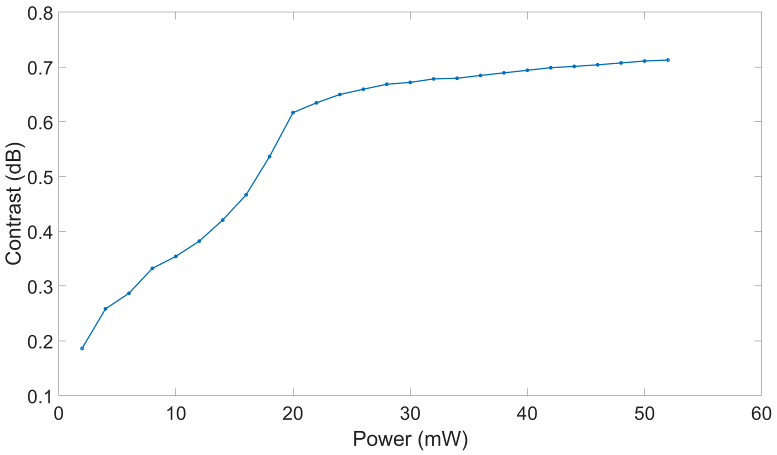

Figure 5.17: The normalized contrast between the A and C sites showing a profile similar to that of the increase in IPR and tending towards a value of approximately C=0.71.

be 6 times larger than that from the C sites. In fact, Figure 5.17 shows the normalized contrast between the two tending towards a value of around 0.71, which suggests the simple ratio between the two intensities (and thus populations) is tending towards a ratio of 5.9:1, something certainly comparable to the previous 6:1 estimates, further strengthening the fact that a full non-linear CLS is present. The ratio of 5.9:1 also allows calculation the maximum value of IPR for such a state, with a returned value of 0.37. Comparing this to the maximum IPR of 0.196 indicates again that full localisation is not achieved. This explanation for this is the same as in the linear case; background noise along with undesirable excitation of the dispersive bands owing to a relatively broad flat band linewidth.

5.6 Conclusion

The work presented in this chapter shows the first demonstration of the direct resonant excitation of linear and non-linear CLSs in a 2D micropillar Lieb lattice microcavity. In the former case it shows that by using an intuitive SLM patterned spot to match the characteristic real space emission profile of the S flat band through the substrate layer of the microcavity sample, a CLS can be created in the linear regime. An IPR value of 0.14 is calculated for such a state, a value 0.11 away from the IPR value of 0.25 for a fully localised state in the case of four separate sites of equal emission. This work also shows that whilst a Laguerre Gaussian spot my be a viable option for the direct excitation of a linear CLS, it suffers focusing issues and may need careful consideration in the optical set-up to be used successfully.

For the case of CLSs at the P flat band energy, this work shows that non-linearity in the emission can be achieved when exciting a single micropillar by carefully matching the phase requirements of each lobe along with considering their orientation relative to the position of the site with respect to the B site. Full CLS formation is achievable for the P flat band energies if a method is developed to allow matching of the lobes across multiple A and C sites. Attempts to do so in this process of this work using an SLM was hindered by undesirable interference effects between the lobes in the laser spot. A proposed approach is to repeat the cigar shaped spot method used in this work for the S flat band energies but with a phase masked in the excitation path to split the spot along the long axis. If successful the threshold of non-linearity in this case is expected to significantly lower due to higher excitonic fraction of the P flat band states. A lower threshold will decrease sample heating and potentially allow a CLS with a IPR value even closer to that of a fully localised state than already observed.

Finally, the work presented in this chapter goes on to show that the previously used SLM approach to excite a full CLS at the S flat band energy is hindered by sample heating and the consequential red shift when attempting to excite a non-linear CLS. It provides alternative approach to remedy this including the use of an EOM and elliptical modulation of the spot to lessen the sample heating resulting in the successful direct resonant excitation of a non-linear CLS at the S flat band energy. It reasons this non-linearity is due to the renormalization of the flat band with the positively detuned laser energy by showing that as polariton density is increased, the emission profile becomes more CLS-like with a decrease in emission from the B sites. The spread across the lattice for the non-linear CLS is quantified to give a maximum IPR value of 0.196 indicating a high level of localisation across the four expected emission pillars. An explanation for non-total localisation is given as being due to background counts and some excitation of the dispersive bands leaving opportunities to optimise the degree of localisation using a sample with a narrower flat band linewidth. This work also estimates the ratio of the tunnelling rates from the A sites to the B sites and the C sites to the B sites. This is done by considering incident polarisation and polarisation dependant tunnelling probabilities by taking into account the change in contrast between the A and C sites across the non-linear threshold.

The work presented in this chapter is part of a larger work in progress and provides the groundwork for further systematic measurements at a later date in preparation for journal submission. However, this work already opens the door to future studies of non-linear CLS states in other 2D flat band energy systems and the potential for using the 2D Lieb lattice etched micropillar platform for the simulation of other non-photonic flat band systems in many-body physics.

Chapter 6

Summary and Outlook

6.1 Summary

In this thesis, PhC waveguides, planar microcavities and etched lattice microcavities have all been investigated. The effects studied have considered both the linear and non-linear regimes along with spin-orbit coupling, cavity birefringence and polariton magnetic responses.

In Chapter 3 waveguide polaritons were demonstrated in 2D PhC's, created by etching into the top GaAs layer of the device. Grating couplers were used to collect the resulting emission and bad gaps were observed in the polaritons dispersion. The band gaps were explored for their suitability in the support of topologically protected edge states. The size and position of the band gaps on the polariton dispersion were explored and shown to vary in size depending on the crystal lattice spacing and the excitonic fraction. It was also shown that higher levels of attenuation from within the gaps could be achieved by increasing the PhC length. The magnetic response of the band gaps were also explored and a Zeeman splitting induced in the exciton resonance. It was shown that, by causing a diamagnetic blue shift in the exciton resonance, the size of the band gap increased due to a decrease in the excitonic fraction. A Zeeman splitting of 0.5 meV was achieved along with band gaps of varying sizes up to 5.4 meV. Whilst these are the basic ingredients required to support topologically protected states, a Zeeman splitting larger than the band gap must first be achieved.

In Chapter 4 the first observations of Zitterbewegung for highly photonic microcavity polaritons were presented. It was shown that this effect arises due to the interference between two energy split branches on the LPB using two approaches. The first approach excited only a single branch using a linearly polarised pump laser, showing no Zitterbewegung in the trajectory of the highly photonic polaritons. Then a circularly polarised pump laser was used to excite both branches and showed that Zitterbewegung oscillations were now present. The second approach showed that by varying the degree of overlap between the reciprocal spot and the two TE-TM modes, Zitterbewegung became clearer the higher the degree of resonance with both branches. This work also showed that the period of the Zitterbewegung oscillations had an inverse relationship with the magnitude of the energy splitting. This was shown by exciting at different regions of the LPB where the energy splitting between the TE-TM modes varied. It also took in to account the birefringence of the cavity on this energy splitting. A similar but less clear relationship for the amplitude was also observed. Finally, this work showed the presence of Zitterbewegung in the trajectory of propagating highly photonic polaritons with wavevectors close to the Dirac point in an etched micropillar lattice. It showed that the difference in group velocities between the s and p bands lead to a different energy splitting at the same wavevectors which in turn lead to different periods and amplitudes of Zitterbewegung. Using the honeycomb lattice allowed observations of Zitterbewegung with a smaller period but a still observable amplitude.

In Chapter 5 the work concerned the direct excitation of compact localized states in a 2D Lieb etched micropillar lattice. It showed that these states arose due to the non-dispersive flat band nature of energy states in the Lieb Lattice dispersion. First a localized state was briefly studied in the linear regime by resonantly exciting the S flat band with a spot patterned to match the characteristic real space emission profile of these states. This work then went on to explain why a similar approach wouldn't work for the non-linear regime and presented an effective approach to observe non-linearity in the emission intensity for a single micropillar excited resonantly at the P flat band energy. Finally, this work presented the full resonant excitation of a non-linear compact localized state using an elliptical spot to excite two C site micropillars. It was shown using power dependencies that a sharp non-linear increase in the emission could be observed with a threshold of approximately 20 mW. Finally the lattice spread was quantified in both the linear and non-linear regimes with a high degree of localisation in both cases. In the linear regime an IPR value of 0.14 was calculated. In the non-linear regime an IPR of 0.19 was calculated. In both cases, the IPR calculations considered 16 lattice sites in total.

6.2 Outlook

6.2.1 Zitterbewegung for polaritons with a larger excitonic fraction

In Chapter 4, the use of highly photonic polaritons offers the benefit of a longer propagation path, which crucial for observing the large periods present in Zitterbewegung, however, the shortfall of this is the loss of the non-linear properties synonymous with polaritons. The use of a cavities with a reduced energy detuning between the exciton and photon resonance would increase the exciton content of the polaritons and thus allow studies on the effects of inter-particle interactions and sensitivity to magnetic fields. The latter has been proposed theoretically by E. S. Sedov et. al, whereby the Zitterbewegung effect is amplified along with an ability to control the period and amplitude with relative ease[164].

A proposed system to test this magnetic response involves highly excitonic polaritons, however, since this would decrease propagation distance of the polari-

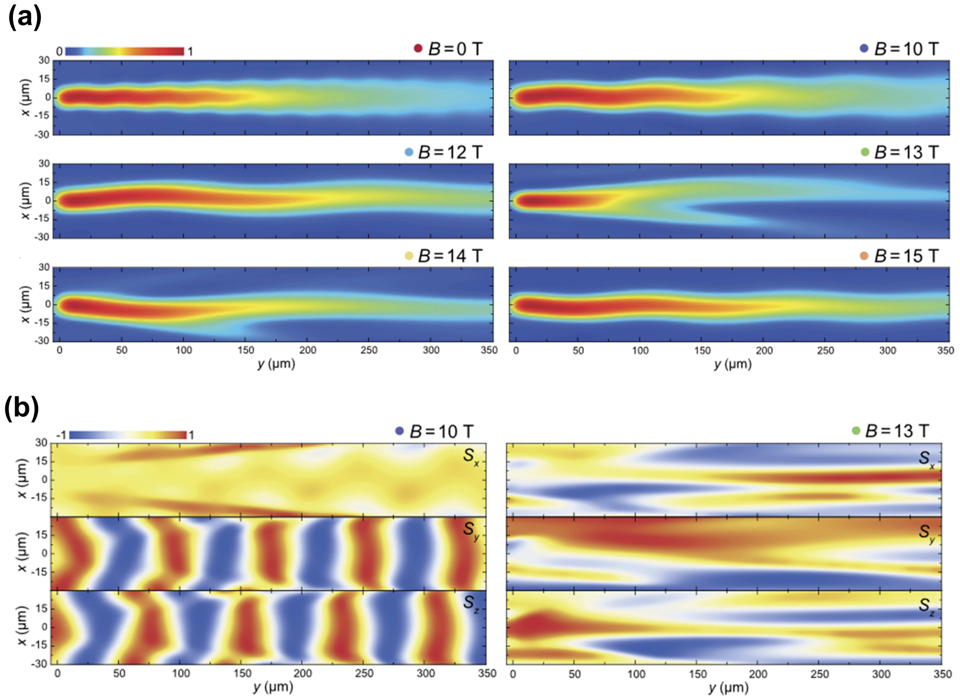

Figure 6.1: (a) The predicted effects of different magnitudes of an applied magnetic field (0-15T) on the period and amplitude of the Zitterbewegung oscillation for exciton polaritons. The magnitudes of the magnetic field are indicated next to each panel. (b) The predicted effects of high magnitude magnetic fields on the spatial distribution of the three Stokes vectors for exciton-polaritons with Zitterbewegung oscillations in their trajectory. The magnitudes of the magnetic field are indicated next to both panels. Taken from [164].

tons, it may be unviable to observe large period Zitterbewegung oscillations for the TE-TM splitting values present at lower wavevectors on the dispersion. The integration of an applied magnetic field could be achieved by placing the sample in a superconducting magnet bath cryostat, similar to the one used in Chapter 3. The higher angles of excitation required to observe smaller Zitterbewegung periods could be achieved by adding a tilt to the mounted sample relative to the incident laser angle. By varying the current applied to the superconducting magnetic, the magnitude of the applied magnetic field could be varied and its effect on the Zitterbewegung measured. A further expansion of this method could incorporate the polarisation textures observed in the trajectory of the propagating polaritons by resolving the PL emission in various polarisations and calculating the Stokes vectors. The spatial distribution of these textures should also vary with the applied magnetic field strength. With the introduction of a magnetic field along with strong interparticle interactions, a wider class of photonic analogues of relativistic systems can be studied with particle interactions, time-reversal symmetry breaking and dissipative effects.

6.2.2 Expansion of Lieb lattice CLS studies and the time resolved evolution of compact localised states

Whilst the work in Chapter 5 shows the successful direct excitation of linear and non-linear CLSs in a 2D Lieb lattice, there is still space for improvements in the method and expansion of the results. One such proposed expansion on this study includes measurements in the linear regime for large energy detunings above the top of the S flat band energy. This will highlight how the destructive interference at the B sites and the IPR value significantly decreases when less efficient excitation of the flat band occurs. This work also gives an explanation for differing polariton population at A and C sites; however this explanation could be confirmed by repeating the experiments but with a horizontally polarised laser with an opposite contrast between the A and C sites expected. A circularly polarised laser could then be used to show equal occupation of both A and C sites. Resolving the emission with polarisation optics could also be done to highlight the previously studied spin textures for non-resonantly pumped CLSs in 2D Lieb lattice[105].

There has been a recent proposal to study the time resolved dynamics of CLSs in flat band lattices such as the 2D Lieb lattice used in this thesis[163].

Such work could involve the use of a streak camera and a pulsed laser to study the evolution of the localised states at finite time intervals after initial excitation. These proposals suggest that the evolution of a compact localised state at low polariton density would exhibit fast Rabi oscillations between the excitonic and photonic components along with slow beating in the Rabi amplitude. At high densities it is expected that these oscillations and beatings will be suppressed by self-interaction effects and distributed losses. It is also suggested that a background incoherent pump could be used to increase the lifetimes and stability of the CLS, such an approach could also be applied to the methods described in Chapter 5 of this thesis for more stable CLS formation.

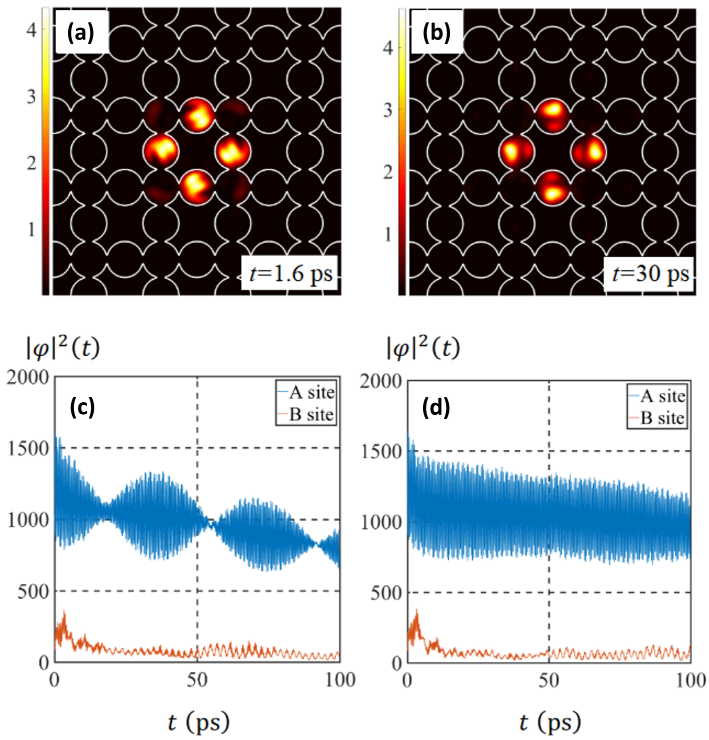

Figure 6.2: (a-b) Snapshots of the CLS polariton density at two different times, showing the evolution of the state.(c-d) Rabi oscillation for the photonic component for CLS of low (c) and high (d) density. Taken from [163].

Chapter 7

Appendix

7.1 Appendix A

Supplementary Materials for Observation of *Zitterbewegung* in photonic microcavities

Seth Lovett,[1] Paul M. Walker,[1,*] Alexey Osipov,[2] Alexey Yulin,[2] Pooja Uday Naik,[1] Charles E. Whittaker,[1] Ivan A. Shelykh,[3,2] Maurice S. Skolnick,[1] and Dmitry N. Krizhanovskii[1]
[1] *Department of Physics and Astronomy, University of Sheffield, S3 7RH, Sheffield, UK*
[2] *Department of Physics and Technology, ITMO University, St. Petersburg, 197101, Russia*
[3] *Science Institute, University of Iceland, Dunhagi 3, IS-107, Reykjavik, Iceland*

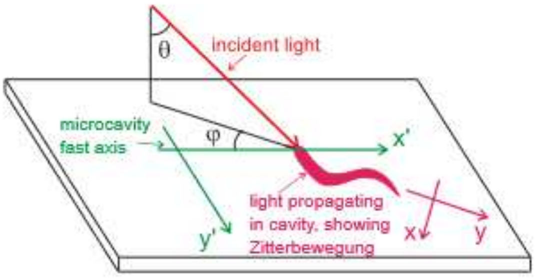

FIG. 1. The sketch of the system showing the direction of the incident light wave vector (red arrow), its projection on the waveguide plane, the orientation of the principal axes of the waveguide (green). Propagation of the guided waves is illustrated schematically by magenta color. The laboratory frame axes x and y, shown by magenta lines, are oriented along (y) and orthogonal (x) to the light incidence plane. The angle of incidence is denoted as θ and the angle between y and the principal axis x' is φ.

I. MODELLING OF *ZITTERBEWEGUNG* IN PLANAR MICROCAVITY

In this section we shed the light on the technical details of the numerical simulation of the *Zitterbewegung*. We start with the case of the cavity formed by two Bragg mirrors separated by a dielectric layer. The mirrors have finite transparency and thus can be excited by a light beam at some incidence angle θ, see Fig. 1 showing schematically the experimental setup. To reproduce the experimental data we need to take into account that the the phase of the complex reflection coefficient of the mirrors depend on the polarization, i.e. there is TE-TM splitting of the guided waves.

The dielectric layers in the experiment are birefrigent and we account for this in our numerical simulations. Because of the anisotropy we need to characterize the orientation of the light incidence plane with respect to the principal axes of the structure. For this we introduce the angle φ as the angle between the light incidence plane (the $y-z$ plane) and one of the principal axes (the fast axis) denoted as x', see Fig. 1.

The cavity is thin (having thickness of only two wavelengths) and so only the two longitudinal modes lowest in frequency (one for each of two orthogonal polarisations) have to be taken into account. Then to describe the evolution of the field in the cavity it is convenient to use the slow varying amplitude approach and characterize the electromagentic field by complex amplitudes of two modes having different polarizations. In the basis of circular polarizations the equations for the amplitudes read

$$\begin{gathered} i\hbar\partial_t\psi_\pm + \frac{\hbar^2}{2m}\nabla^2\psi_\pm + i\gamma\psi_\pm + \frac{\Omega}{2}\psi_\mp \\ +\beta(\partial_{x'} + i\partial_{y'})^2\psi_\mp = P_\pm f(r)e^{-i\Delta t + i(\boldsymbol{k'}\cdot\boldsymbol{r'})} \end{gathered} \tag{1}$$

where $\psi_\pm$ are the slow varying amplitudes of the clock- and counter-clockwise circular polarizations, γ is the losses, Ω is the splitting at $k=0$ caused by birefrigence, β is the TE-TM splitting strength, $P_\pm$ are the pump produced by two polarizations of the incident beam, $f(r)$ is the function describing the spatial aperture of the incident field, Δ is the detuning of the incident light frequency from the minimum energy of the cavity dispersion (see Fig. 1b and 1c in the main text) and $\boldsymbol{k'}$ is the projection of the wave vector of the incident beam on the cavity plane. Experimentally, the transmitted field corresponds exactly to $\psi_\pm$ and in the main text we plot the total intensity $|\psi_+|^2 + |\psi_-|^2$ in Fig. 1a in the main text.

To find the parameters of our mathematical model (Eqn. 1) we fit the experimental oscillations in Figs. 2(a) and 2(b) in the main text. The parameters we obtain, and which are used in the simulations below, are $\Omega = 28.8$ µeV·µm^2 and $\beta = 32.45$ µeV·µm^2. We took the parameters $m = 950$ µeV·µm^2 and $\gamma = 34$µeV from the fitting of the experimental dispersion curves discussed in the main text. The incident light beam had a Gaussian profile $f(r) = e^{-\frac{r^2}{L^2}}$ with the half-width $L = 15\,\mu m$. The incident wavevector in the sample coordinate frame is given by $\boldsymbol{k'} = [\frac{2\pi}{\lambda}\sin(\theta)\cos(\varphi), \frac{2\pi}{\lambda}\sin(\theta)\sin(\varphi)]$.

The stationary solutions of (1) were calculated by the expansion of the field over the plane wave modes, finding the mode amplitudes and then summing the modes to get the total field. Then, knowing the spatial distribution of the field for fixed frequencies Δ it is easy to calculate the intensity distribution of the total field or in the polarization of interest. To calculate the trajectory $x_c(y)$ we calculate the first moment (expectation) defined in a common way as $x_c(y) = \int Ixdx / \int Idx$ where I is the field intensity.

To observe the *Zitterbewegung* we did the simulations for the circularly polarized pump with the wavevector

---

[*] p.m.walker@sheffield.ac.uk

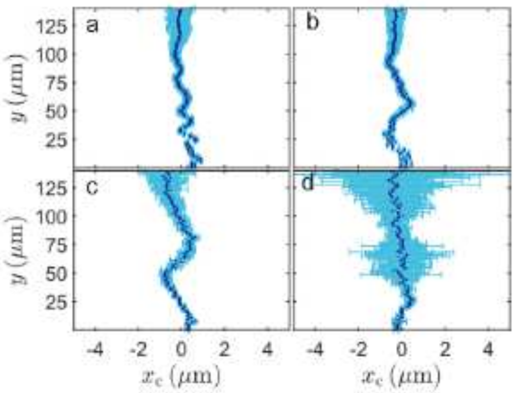

FIG. 2. Center of intensity x_c vs y. (a) Resonant excitation of one branch only using linear polarisation. (b) Resonant excitation of both branches using circular polarisation. For both (a) and (b) the incidence angle was 11 degrees and the laser energy was 1.90 meV above the bottom of the dispersion, equally resonant with both branches. (c) Resonant excitation at 10 degrees and energy 1.57 meV above the bottom of the dispersion and with circular polarisation. (d) Off-resonant excitation at the same energy and polarisation as in (c) but at 11 degrees. Black points are raw experimental data.

$k = \sqrt{\frac{2m\Delta}{\hbar^2}}$ equally detuned from the wave vectors of the eigenmodes of different polarizations. This ensures the nearly equal excitation efficiency for both of the modes. The comparison of the results of the numerical simulations with the experimental data are shown in Fig. 2 in the main text of the paper, for the incident beam directed along the first and the second principle axes of the sample. There is good agreement between the simulated curves and the experimental points for the parameters given above. The values of Ω and β given above, which were extracted by fitting our model of *Zitterbewegung* to the experimental the oscillations, are in good agreement with the values independently extracted by fitting the dispersion curves as discussed in the main text. This agreement verifies that the observed oscillations are consistent with the *Zitterbewegung* effect.

II. OFF RESONANCE EXCITATION OF THE CAVITY

Zitterbewegung occurs due to an interference between two polarisation components. The characteristic oscillation of the center of mass x_c of the total intensity distribution is only expected to be observed when both polarisation branches are equally excited. Figures 2(a) and (b) show x_c vs. y for the cases where only one branch was excited and both branches were excited, respectively. This was achieved by setting the polarisation state of the incident laser to either linear or circular respectively. Figure 2(a) shows a small drift of $x_c(y)$ with low amplitude and short period ($\sim$ 20 μm) approximate oscillations resulting from a low intensity parasitic signal.The very short period means we can be confident that these are not related to Zitterbewegung. By contrast, Figure 2(b) shows much larger amplitude and longer period oscillations consistent with the *Zitterbewegung* effect. We also studied the case where one branch was more strongly excited than the other because we detuned the laser incidence angle away from the midpoint of the two branches. In this case the excitation polarisation was always circular. The angular half width at half maximum of the Fourier transform of the laser spot is 0.7 degrees, and we tuned $\sim$ 1 degree either side of the resonance (e.g. the point where both branches are excited equally) in steps of 0.3 degrees. The position of equal excitation of both branches was estimated by maximising the total transmitted intensity. Figure 2(c) shows the case where both branches are equally excited (10 degrees incidence angle), while Fig. 2(d) shows the case where the excitation laser spot in momentum space overlaps one branch more strongly than the other (11 degrees incidence angle). In both cases the laser energy is the same, 1.57 meV above the bottom of the dispersion. As expected, the oscillations disappear when only branch is strongly excited such that the contribution from interference between the branches is weak.

III. MODELLING OF *ZITTERBEWEGUNG* IN HONEYCOMB LATTICE

The simulations of the *Zitterbewegung* in honeycomb lattices is done using the model introduced in[?, ?]. The model describes the dynamics of the modes with the wavevectors lying in the vicinity of the K-points of the lattice dispersion relation, where the dispersion has the shape of a Dirac cone. In such lattices the polarisation splitting is dominated by the difference in the tunnelling rate for photons with polarisation aligned along or orthogonal to the vector between two pillars[7] . Since the tunnelling vector depends on the photon wavevector this splitting is similar to a TE-TM splitting, though not exactly the same as that in planar structures. The model accounts for this splitting , which lifts the polarisation degeneracy of the cone, while it neglects the anisotropy (birefringence) of the dielectric layers. This approach is justified as it was showing in Ref.[7] that the polarisation properties of this sample could be fully described using only the tunnelling-based polarisation splitting. The model is applicable for s and p-states but the parameters have to be fitted separately for each of the cases.

Within the model the equations are written for four field components $\Psi = [\psi_A^+, \psi_B^+, \psi_A^-, \psi_B^-]$, where ± denotes the polarization and A, B marks the sublattice degree of freedom (different symmetry of the wavefunction over the two sites contained in the elementary cell of the periodic

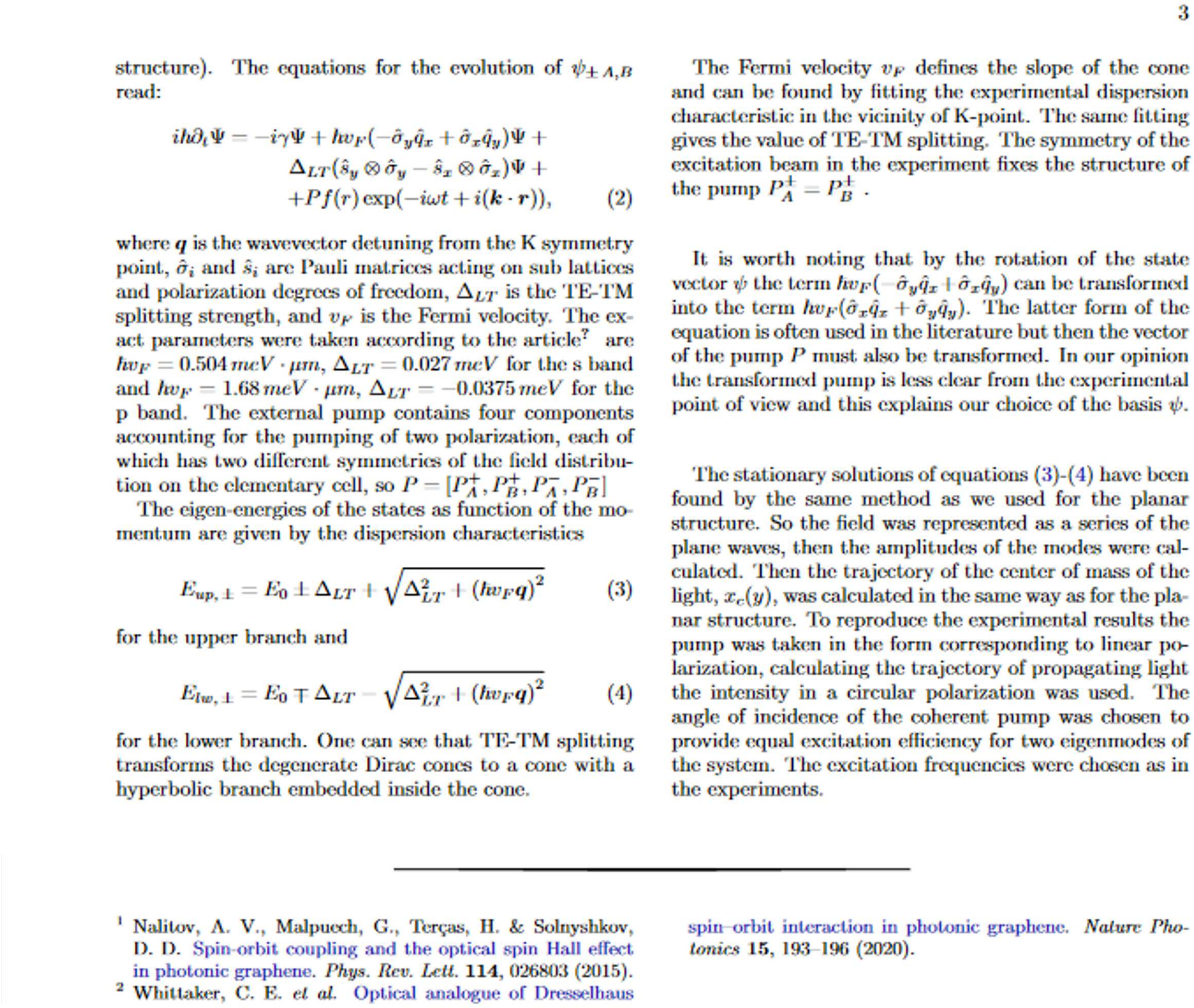

structure). The equations for the evolution of $\psi_{\pm A,B}$ read:

$$\begin{aligned} i\hbar\partial_t\Psi = -i\gamma\Psi + \hbar v_F(-\hat{\sigma}_y\hat{q}_x + \hat{\sigma}_x\hat{q}_y)\Psi + \\ \Delta_{LT}(\hat{s}_y \otimes \hat{\sigma}_y - \hat{s}_x \otimes \hat{\sigma}_x)\Psi + \\ +Pf(r)\exp(-i\omega t + i(\boldsymbol{k}\cdot\boldsymbol{r})), \end{aligned} \tag{2}$$

where $\boldsymbol{q}$ is the wavevector detuning from the K symmetry point, $\hat{\sigma}_i$ and $\hat{s}_i$ are Pauli matrices acting on sub lattices and polarization degrees of freedom, Δ_{LT} is the TE-TM splitting strength, and v_F is the Fermi velocity. The exact parameters were taken according to the article? are $\hbar v_F = 0.504\,meV\cdot\mu m$, $\Delta_{LT} = 0.027\,meV$ for the s band and $\hbar v_F = 1.68\,meV\cdot\mu m$, $\Delta_{LT} = -0.0375\,meV$ for the p band. The external pump contains four components accounting for the pumping of two polarization, each of which has two different symmetries of the field distribution on the elementary cell, so $P = [P_A^+, P_B^+, P_A^-, P_B^-]$

The eigen-energies of the states as function of the momentum are given by the dispersion characteristics

$$E_{up,\pm} = E_0 \pm \Delta_{LT} + \sqrt{\Delta_{LT}^2 + (\hbar v_F \boldsymbol{q})^2} \tag{3}$$

for the upper branch and

$$E_{lw,\pm} = E_0 \mp \Delta_{LT} - \sqrt{\Delta_{LT}^2 + (\hbar v_F \boldsymbol{q})^2} \tag{4}$$

for the lower branch. One can see that TE-TM splitting transforms the degenerate Dirac cones to a cone with a hyperbolic branch embedded inside the cone.

The Fermi velocity v_F defines the slope of the cone and can be found by fitting the experimental dispersion characteristic in the vicinity of K-point. The same fitting gives the value of TE-TM splitting. The symmetry of the excitation beam in the experiment fixes the structure of the pump $P_A^+ = P_B^+$.

It is worth noting that by the rotation of the state vector ψ the term $\hbar v_F(-\hat{\sigma}_y\hat{q}_x + \hat{\sigma}_x\hat{q}_y)$ can be transformed into the term $\hbar v_F(\hat{\sigma}_x\hat{q}_x + \hat{\sigma}_y\hat{q}_y)$. The latter form of the equation is often used in the literature but then the vector of the pump P must also be transformed. In our opinion the transformed pump is less clear from the experimental point of view and this explains our choice of the basis ψ.

The stationary solutions of equations (3)-(4) have been found by the same method as we used for the planar structure. So the field was represented as a series of the plane waves, then the amplitudes of the modes were calculated. Then the trajectory of the center of mass of the light, $x_c(y)$, was calculated in the same way as for the planar structure. To reproduce the experimental results the pump was taken in the form corresponding to linear polarization, calculating the trajectory of propagating light the intensity in a circular polarization was used. The angle of incidence of the coherent pump was chosen to provide equal excitation efficiency for two eigenmodes of the system. The excitation frequencies were chosen as in the experiments.

---

[1] Nalitov, A. V., Malpuech, G., Terças, H. & Solnyshkov, D. D. Spin-orbit coupling and the optical spin Hall effect in photonic graphene. *Phys. Rev. Lett.* **114**, 026803 (2015).

[2] Whittaker, C. E. *et al.* Optical analogue of Dresselhaus spin–orbit interaction in photonic graphene. *Nature Photonics* **15**, 193–196 (2020).

Bibliography

1. Wang, Y.-F., Gu, Z.-C., Gong, C.-D. & Sheng, D. Fractional quantum Hall effect of hard-core bosons in topological flat bands. *Physical review letters* **107,** 146803 (2011).
2. Wu, C., Bergman, D., Balents, L. & Sarma, S. D. Flat bands and Wigner crystallization in the honeycomb optical lattice. *Physical review letters* **99,** 070401 (2007).
3. Yin, J.-X. *et al.* Negative flat band magnetism in a spin–orbit-coupled correlated kagome magnet. *Nature Physics* **15,** 443–448 (2019).
4. Chen, R., Xu, D.-H. & Zhou, B. Disorder-induced topological phase transitions on Lieb lattices. *Physical Review B* **96,** 205304 (2017).
5. Sedov, E., Rubo, Y. & Kavokin, A. Zitterbewegung of exciton-polaritons. *Physical Review B* **97,** 245312 (2018).
6. Lovett, S. *et al.* Observation of Zitterbewegung in photonic microcavities. *Light: Science & Applications* **12,** 126 (2023).
7. Nguyen, H. S. *et al.* Acoustic black hole in a stationary hydrodynamic flow of microcavity polaritons. *Physical review letters* **114,** 036402 (2015).
8. Jacquet, M. *et al.* Polariton fluids for analogue gravity physics. *Philosophical Transactions of the Royal Society A* **378,** 20190225 (2020).
9. Deng, H., Weihs, G., Santori, C., Bloch, J. & Yamamoto, Y. Condensation of semiconductor microcavity exciton polaritons. *Science* **298,** 199–202 (2002).

10. Kasprzak, J. *et al.* Bose–Einstein condensation of exciton polaritons. *Nature* **443,** 409–414 (2006).
11. Kasap, S. O. & Capper, P. *Springer handbook of electronic and photonic materials* (Springer).
12. Weisbuch, C., Nishioka, M., Ishikawa, A. & Arakawa, Y. Observation of the coupled exciton-photon mode splitting in a semiconductor quantum microcavity. *Physical Review Letters* **69,** 3314 (1992).
13. Weisbuch, C., Nishioka, M., Ishikawa, A. & Arakawa, Y. Observation of the coupled exciton-photon mode splitting in a semiconductor quantum microcavity. *Phys. Rev. Lett.* **69,** 3314–3317 (23 Dec. 1992).
14. André, R., Heger, D., Dang, L. S. & d'Aubigné, Y. M. Spectroscopy of polaritons in CdTe-based microcavities. *Journal of crystal growth* **184,** 758–762 (1998).
15. Malpuech, G. *et al.* Room-temperature polariton lasers based on GaN microcavities. *Applied physics letters* **81,** 412–414 (2002).
16. Christopoulos, S. *et al.* Room-temperature polariton lasing in semiconductor microcavities. *Physical review letters* **98,** 126405 (2007).
17. Gross, E. & Karryjew, I. The optical spectrum of the exciton. **84,** 471–474 (1952).
18. Gross, E. Optical spectrum of excitons in the crystal lattice. *Il Nuovo Cimento (1955-1965)* **3,** 672–701 (1956).
19. Frenkel, J. On the transformation of light into heat in solids. I. *Physical Review* **37,** 17 (1931).
20. Frenkel, J. On the transformation of light into heat in solids. II. *Physical Review* **37,** 1276 (1931).
21. Wannier, G. H. The structure of electronic excitation levels in insulating crystals. *Physical Review* **52,** 191 (1937).

22. Lee, D., Johnson, A., Zucker, J., Feldman, R. & Austin, R. *Room Temperature Excitonic Absorption in CdZnTe/ZnTe Multiple Quantum Wells* in *International Quantum Electronics Conference* (1990), QPDP18.
23. Tsintzos, S., Savvidis, P., Deligeorgis, G., Hatzopoulos, Z. & Pelekanos, N. Room temperature GaAs exciton-polariton light emitting diode. *Applied Physics Letters* **94,** 071109 (2009).
24. Hall, R. N., Fenner, G. E., Kingsley, J., Soltys, T. & Carlson, R. Coherent light emission from GaAs junctions. *Physical Review Letters* **9,** 366 (1962).
25. Nathan, M. I., Dumke, W. P., Burns, G., Dill Jr, F. H. & Lasher, G. Stimulated emission of radiation from GaAs p-n junctions. *Applied Physics Letters* **1,** 62–64 (1962).
26. Huang, Y.-z. *et al. Microcavity Semiconductor Lasers: Principles, Design, and Applications* (John Wiley & Sons, 2021).
27. He, L., Özdemir, Ş. K. & Yang, L. Whispering gallery microcavity lasers. *Laser & Photonics Reviews* **7,** 60–82 (2013).
28. Coleman, J. J. The development of the semiconductor laser diode after the first demonstration in 1962. *Semiconductor Science and Technology* **27,** 090207 (2012).
29. Tinkler, L. *et al.* Design and characterization of high optical quality InGaAs/GaAs/AlGaAs-based polariton microcavities. *Applied Physics Letters* **106,** 021109 (2015).
30. Mizutani, M., Teramae, F., Kobayashi, O., Naritsuka, S. & Maruyama, T. Precise control of growth of DBR by MBE using in-situ reflectance monitoring system. *physica status solidi c* **3,** 659–662 (2006).
31. Schneider, C., Gold, P., Reitzenstein, S., Hoefling, S. & Kamp, M. Quantum dot micropillar cavities with quality factors exceeding 250,000. *Applied Physics B* **122,** 1–6 (2016).
32. Armani, D., Kippenberg, T., Spillane, S. & Vahala, K. Ultra-high-Q toroid microcavity on a chip. *Nature* **421,** 925–928 (2003).

33. Kroemer, H. A proposed class of hetero-junction injection lasers. *Proceedings of the IEEE* **51,** 1782–1783 (1963).

34. Chernov, A. & Abyzov, A. Authors' certificates. *Refractories* **14,** 530–531 (1973).

35. Kawai, H., Kaneko, K. & Watanabe, N. Photoluminescence of AlGaAs/GaAs quantum wells grown by metalorganic chemical vapor deposition. *Journal of applied physics* **56,** 463–467 (1984).

36. Byrnes, T., Kim, N. Y. & Yamamoto, Y. Exciton–polariton condensates. *Nature Physics* **10,** 803–813 (2014).

37. Hopfield, J. Theory of the contribution of excitons to the complex dielectric constant of crystals. *Physical Review* **112,** 1555 (1958).

38. Lundt, N. *Strong light-matter coupling with 2D materials* PhD thesis (Jan. 2019).

39. Renucci, P. *et al.* Microcavity polariton spin quantum beats without a magnetic field: A manifestation of Coulomb exchange in dense and polarized polariton systems. *Physical Review B* **72,** 075317 (2005).

40. Tartakovskii, A. *et al.* Nonlinearities in emission from the lower polariton branch of semiconductor microcavities. *Physical Review B* **60,** R11293 (1999).

41. Vladimirova, M. *et al.* Polariton-polariton interaction constants in microcavities. *Physical Review B* **82,** 075301 (2010).

42. Sun, Y. *et al.* Direct measurement of polariton–polariton interaction strength. *Nature Physics* **13,** 870–875 (2017).

43. Estrecho, E. *et al.* Direct measurement of polariton-polariton interaction strength in the Thomas-Fermi regime of exciton-polariton condensation. *Physical Review B* **100,** 035306 (2019).

44. Stevenson, R. *et al.* Continuous wave observation of massive polariton redistribution by stimulated scattering in semiconductor microcavities. *Physical Review Letters* **85,** 3680 (2000).

45. Tartakovskii, A., Krizhanovskii, D. & Kulakovskii, V. Polariton-polariton scattering in semiconductor microcavities: Distinctive features and similarities to the three-dimensional case. *Physical Review B* **62,** R13298 (2000).

46. Krizhanovskii, D. *et al.* Dominant effect of polariton-polariton interactions on the coherence of the microcavity optical parametric oscillator. *Physical review letters* **97,** 097402 (2006).

47. Sanvitto, D. *et al.* Persistent currents and quantized vortices in a polariton superfluid. *Nature Physics* **6,** 527–533 (2010).

48. Imamog, A., Ram, R., Pau, S., Yamamoto, Y., *et al.* Nonequilibrium condensates and lasers without inversion: Exciton-polariton lasers. *Physical Review A* **53,** 4250 (1996).

49. Kasprzak, J., Solnyshkov, D., André, R., Dang, L. S. & Malpuech, G. Formation of an exciton polariton condensate: thermodynamic versus kinetic regimes. *Physical review letters* **101,** 146404 (2008).

50. Spano, R. *et al.* Corrigendum: Coherence properties of exciton polariton OPO condensates in one and two dimensions (2012 New J. Phys. 14 075018). *New Journal of Physics* **16,** 069501 (2014).

51. Deng, H. *et al.* Quantum degenerate exciton-polaritons in thermal equilibrium. *Physical review letters* **97,** 146402 (2006).

52. Wertz, E. *et al.* Spontaneous formation of a polariton condensate in a planar GaAs microcavity. *Applied Physics Letters* **95,** 051108 (2009).

53. Waldherr, M. *et al.* Observation of bosonic condensation in a hybrid monolayer MoSe2-GaAs microcavity. *Nature communications* **9,** 3286 (2018).

54. Anton-Solanas, C. *et al.* Bosonic condensation of exciton–polaritons in an atomically thin crystal. *Nature materials* **20,** 1233–1239 (2021).

55. St-Jean, P. *et al.* Lasing in topological edge states of a one-dimensional lattice. *Nature Photonics* **11,** 651–656 (2017).

56. Kapitza, P. Viscosity of liquid helium below the λ-point. *Nature* **141,** 74–74 (1938).

57. Allen, J. F. & Misener, A. Flow phenomena in liquid helium II. *Nature* **142,** 643–644 (1938).

58. London, F. The λ-phenomenon of liquid helium and the Bose-Einstein degeneracy. *Nature* **141,** 643–644 (1938).

59. London, F. On the bose-einstein condensation. *Physical Review* **54,** 947 (1938).

60. Amo, A. *et al.* Superfluidity of polaritons in semiconductor microcavities. *Nature Physics* **5,** 805–810 (2009).

61. Lerario, G. *et al.* Room-temperature superfluidity in a polariton condensate. *Nature Physics* **13,** 837–841 (2017).

62. Lagoudakis, K. G. *et al.* Quantized vortices in an exciton–polariton condensate. *Nature physics* **4,** 706–710 (2008).

63. Dagvadorj, G. *et al.* Nonequilibrium phase transition in a two-dimensional driven open quantum system. *Physical Review X* **5,** 041028 (2015).

64. Nardin, G. *et al.* Hydrodynamic nucleation of quantized vortex pairs in a polariton quantum fluid. *Nature Physics* **7,** 635–641 (2011).

65. Gerace, D. & Carusotto, I. Analog Hawking radiation from an acoustic black hole in a flowing polariton superfluid. *Physical Review B* **86,** 144505 (2012).

66. Jacquet, M. *et al.* Analogue quantum simulation of the Hawking effect in a polariton superfluid. *The European Physical Journal D* **76,** 152 (2022).

67. Solnyshkov, D., Leblanc, C., Koniakhin, S., Bleu, O. & Malpuech, G. Quantum analogue of a Kerr black hole and the Penrose effect in a Bose-Einstein condensate. *Physical Review B* **99,** 214511 (2019).

68. Amo, A. *et al.* Polariton superfluids reveal quantum hydrodynamic solitons. *Science* **332,** 1167–1170 (2011).

69. Sich, M. *et al.* Observation of bright polariton solitons in a semiconductor microcavity. *Nature photonics* **6,** 50–55 (2012).

70. Yulin, A., Egorov, O., Lederer, F. & Skryabin, D. Dark polariton solitons in semiconductor microcavities. *Physical Review A* **78,** 061801 (2008).

71. Gulevich, D. R., Yudin, D., Skryabin, D. V., Iorsh, I. V. & Shelykh, I. A. Exploring nonlinear topological states of matter with exciton-polaritons: Edge solitons in kagome lattice. *Scientific reports* **7,** 1780 (2017).

72. Sich, M. *et al.* Transition from propagating polariton solitons to a standing wave condensate induced by interactions. *Physical review letters* **120,** 167402 (2018).

73. Skryabin, D. *et al.* Backward Cherenkov radiation emitted by polariton solitons in a microcavity wire. *Nature communications* **8,** 1554 (2017).

74. Cancellieri, E. *et al.* Logic gates with bright dissipative polariton solitons in Bragg cavity systems. *Physical Review B* **92,** 174528 (2015).

75. Meier, F. & Zakharchenya, B. P. *Optical orientation* (Elsevier, 2012).

76. Lampel, G. Nuclear dynamic polarization by optical electronic saturation and optical pumping in semiconductors. *Physical Review Letters* **20,** 491 (1968).

77. Sek, G. *et al.* Study of the nature of light hole excitonic transitions in InGaAs/GaAs quantum well. *Vacuum* **50,** 199–201 (1998).

78. Silver, M., Batty, W., Ghiti, A. & O'Reilly, E. Strain-induced valence-subband splitting in III-V semiconductors. *Physical Review B* **46,** 6781 (1992).

79. Braunstein, R. & Kane, E. The valence band structure of the III–V compounds. *Journal of Physics and Chemistry of Solids* **23,** 1423–1431 (1962).

80. Richard, S., Aniel, F. & Fishman, G. Energy-band structure of Ge, Si, and GaAs: A thirty-band k. p method. *Physical Review B* **70,** 235204 (2004).

81. Shelykh, I. A., Kavokin, A. V. & Malpuech, G. Spin dynamics of exciton polaritons in microcavities. *physica status solidi (b)* **242,** 2271–2289 (2005).

82. Kavokin, A. V., Baumberg, J. J., Malpuech, G. & Laussy, F. P. *Microcavities* (Oxford university press, 2017).

83. Pidgeon, C. & Smith, S. Resolving power of multilayer filters in nonparallel light. *JOSA* **54,** 1459–1466 (1964).

84. Panzarini, G. *et al.* Cavity-polariton dispersion and polarization splitting in single and coupled semiconductor microcavities. *Physics of the Solid State* **41,** 1223–1238 (1999).

85. Maialle, M., e Silva, E. d. A. & Sham, L. Exciton spin dynamics in quantum wells. *Physical Review B* **47,** 15776 (1993).

86. Shelykh, I., Malpuech, G., Kavokin, K., Kavokin, A. & Bigenwald, P. Spin dynamics of interacting exciton polaritons in microcavities. *Physical Review B* **70,** 115301 (2004).

87. Solnyshkov, D. D. *et al.* Microcavity polaritons for topological photonics. *Optical Materials Express* **11,** 1119–1142 (2021).

88. Solnyshkov, D. & Malpuech, G. Chirality in photonic systems. *Comptes Rendus Physique* **17,** 920–933 (2016).

89. Kavokin, A., Malpuech, G. & Glazov, M. Optical spin Hall effect. *Physical review letters* **95,** 136601 (2005).

90. Leyder, C. *et al.* Observation of the optical spin Hall effect. *Nature Physics* **3,** 628–631 (2007).

91. Flayac, H., Solnyshkov, D., Shelykh, I. & Malpuech, G. Transmutation of skyrmions to half-solitons driven by the nonlinear optical spin Hall effect. *Physical Review Letters* **110,** 016404 (2013).
92. Schneider, C. *et al.* Exciton-polariton trapping and potential landscape engineering. *Reports on Progress in Physics* **80,** 016503 (2016).
93. Amo, A. & Bloch, J. Exciton-polaritons in lattices: A non-linear photonic simulator. *Comptes Rendus Physique* **17,** 934–945 (2016).
94. De Lima Jr, M., van der Poel, M., Santos, P. & Hvam, J. M. Phonon-induced polariton superlattices. *Physical review letters* **97,** 045501 (2006).
95. Fraser, M., Tan, H. & Jagadish, C. Selective confinement of macroscopic long-lifetime exciton and trion populations. *Physical Review B* **84,** 245318 (2011).
96. Lai, C. *et al.* Coherent zero-state and π-state in an exciton–polariton condensate array. *Nature* **450,** 529–532 (2007).
97. Fischer, J. *et al.* Magneto-exciton-polariton condensation in a sub-wavelength high contrast grating based vertical microcavity. *Applied Physics Letters* **104,** 091117 (2014).
98. El Daif, O. *et al.* Polariton quantum boxes in semiconductor microcavities. *Applied Physics Letters* **88,** 061105 (2006).
99. Kaitouni, R. I. *et al.* Engineering the spatial confinement of exciton polaritons in semiconductors. *Physical Review B* **74,** 155311 (2006).
100. Bayer, M. *et al.* Optical modes in photonic molecules. *Physical review letters* **81,** 2582 (1998).
101. Bajoni, D. *et al.* Polariton laser using single micropillar GaAs- GaAlAs semiconductor cavities. *Physical review letters* **100,** 047401 (2008).
102. Gutbrod, T. *et al.* Weak and strong coupling of photons and excitons in photonic dots. *Physical Review B* **57,** 9950 (1998).

103. Tanese, D. *et al.* Polariton condensation in solitonic gap states in a one-dimensional periodic potential. *Nature communications* **4,** 1–9 (2013).

104. Kim, N. Y. *et al.* Dynamical d-wave condensation of exciton–polaritons in a two-dimensional square-lattice potential. *Nature Physics* **7,** 681–686 (2011).

105. Whittaker, C. *et al.* Exciton polaritons in a two-dimensional lieb lattice with spin-orbit coupling. *Physical review letters* **120,** 097401 (2018).

106. Baboux, F. *et al.* Bosonic Condensation and Disorder-Induced Localization in a Flat Band. *Phys. Rev. Lett.* **116,** 066402 (6 Feb. 2016).

107. Jacqmin, T. *et al.* Direct observation of Dirac cones and a flatband in a honeycomb lattice for polaritons. *Physical review letters* **112,** 116402 (2014).

108. Milićević, M. *et al.* Edge states in polariton honeycomb lattices. *2D Materials* **2,** 034012 (2015).

109. Papes, M. *et al.* Fiber-chip edge coupler with large mode size for silicon photonic wire waveguides. *Optics express* **24,** 5026–5038 (2016).

110. Markov, P., Valentine, J. G. & Weiss, S. M. Fiber-to-chip coupler designed using an optical transformation. *Optics Express* **20,** 14705–14713 (2012).

111. Nambiar, S., Sethi, P. & Selvaraja, S. K. Grating-assisted fiber to chip coupling for SOI photonic circuits. *Applied Sciences* **8,** 1142 (2018).

112. Beggs, D., Kaliteevski, M., Brand, S., Abram, R. & Kavokin, A. Waveguide polaritons: interaction of a quantum well exciton with an electromagnetic mode of a planar waveguide. *physica status solidi (c)* **2,** 787–790 (2005).

113. Ellenbogen, T. & Crozier, K. B. Exciton-polariton emission from organic semiconductor optical waveguides. *Physical Review B* **84,** 161304 (2011).

114. Walker, P. *et al.* Exciton polaritons in semiconductor waveguides. *Applied Physics Letters* **102,** 012109 (2013).

115. Tinkler, L. *Optical nonlinearities in semiconductor polariton waveguides* PhD thesis (University of Sheffield, 2015).

116. Jamadi, O. *et al.* Edge-emitting polariton laser and amplifier based on a ZnO waveguide. *Light: Science & Applications* **7,** 82 (2018).

117. Ciers, J. *et al.* Propagating polaritons in III-nitride slab waveguides. *Physical Review Applied* **7,** 034019 (2017).

118. Hu, F. *et al.* Imaging exciton–polariton transport in MoSe2 waveguides. *Nature Photonics* **11,** 356–360 (2017).

119. Rosenberg, I., Mazuz-Harpaz, Y., Rapaport, R., West, K. & Pfeiffer, L. Electrically controlled mutual interactions of flying waveguide dipolaritons. *Physical Review B* **93,** 195151 (2016).

120. Pirotta, S. *et al.* Strong coupling between excitons in organic semiconductors and Bloch surface waves. *Applied Physics Letters* **104,** 051111 (2014).

121. Walker, P. *et al.* Ultra-low-power hybrid light–matter solitons. *Nature communications* **6,** 8317 (2015).

122. Walker, P. *et al.* Dark solitons in high velocity waveguide polariton fluids. *Physical review letters* **119,** 097403 (2017).

123. Walker, P. M. *et al.* Spatiotemporal continuum generation in polariton waveguides. *Light: Science & Applications* **8,** 6 (2019).

124. Suárez-Forero, D. *et al.* Electrically controlled waveguide polariton laser. *Optica* **7,** 1579–1586 (2020).

125. Klitzing, K. v., Dorda, G. & Pepper, M. New method for high-accuracy determination of the fine-structure constant based on quantized Hall resistance. *Physical review letters* **45,** 494 (1980).

126. Haldane, F. D. M. & Raghu, S. Possible realization of directional optical waveguides in photonic crystals with broken time-reversal symmetry. *Physical review letters* **100,** 013904 (2008).

127. Wang, Z., Chong, Y., Joannopoulos, J. D. & Soljačić, M. Observation of unidirectional backscattering-immune topological electromagnetic states. *Nature* **461,** 772–775 (2009).

128. Rechtsman, M. C. *et al.* Photonic Floquet topological insulators. *Nature* **496,** 196–200 (2013).

129. Hafezi, M., Mittal, S., Fan, J., Migdall, A. & Taylor, J. Imaging topological edge states in silicon photonics. *Nature Photonics* **7,** 1001–1005 (2013).

130. Karzig, T., Bardyn, C.-E., Lindner, N. H. & Refael, G. Topological polaritons. *Physical Review X* **5,** 031001 (2015).

131. Nalitov, A., Solnyshkov, D. & Malpuech, G. Polariton Z topological insulator. *Physical review letters* **114,** 116401 (2015).

132. Klembt, S. *et al.* Exciton-polariton topological insulator. *Nature* **562,** 552–556 (2018).

133. Whittaker, C. *et al.* Exciton–polaritons in GaAs-based slab waveguide photonic crystals. *Applied Physics Letters* **119,** 181101 (2021).

134. Zawadzki, W. & Rusin, T. M. Zitterbewegung (trembling motion) of electrons in semiconductors: a review. *Journal of Physics: Condensed Matter* **23,** 143201 (2011).

135. Hivet, R. *et al.* Half-solitons in a polariton quantum fluid behave like magnetic monopoles. *Nature Physics* **8,** 724–728 (2012).

136. Polimeno, L. *et al.* Experimental investigation of a non-Abelian gauge field in 2D perovskite photonic platform. *Optica* **8,** 1442–1447 (2021).

137. Bieganska, D. *et al.* Collective excitations of exciton-polariton condensates in a synthetic gauge field. *Physical Review Letters* **127,** 185301 (2021).

138. Ballarini, D. *et al.* Macroscopic two-dimensional polariton condensates. *Physical Review Letters* **118,** 215301 (2017).

139. Barut, A. & Bracken, A. Zitterbewegung and the internal geometry of the electron. *Physical Review D* **23,** 2454 (1981).

140. Schliemann, J., Loss, D. & Westervelt, R. Zitterbewegung of electronic wave packets in III-V zinc-blende semiconductor quantum wells. *Physical review letters* **94,** 206801 (2005).

141. Schliemann, J., Loss, D. & Westervelt, R. Zitterbewegung of electrons and holes in III–V semiconductor quantum wells. *Physical Review B* **73,** 085323 (2006).

142. Winkler, R., Zülicke, U. & Bolte, J. Oscillatory multiband dynamics of free particles: The ubiquity of zitterbewegung effects. *Physical Review B* **75,** 205314 (2007).

143. Gerritsma, R. *et al.* Quantum simulation of the Dirac equation. *Nature* **463,** 68–71 (2010).

144. Stepanov, I. *et al.* Coherent electron zitterbewegung. *arXiv preprint arXiv:1612.06190* (2016).

145. Dreisow, F. *et al.* Classical simulation of relativistic Zitterbewegung in photonic lattices. *Physical Review Letters* **105,** 143902 (2010).

146. Yao, Q. *et al.* Ballistic transport of a polariton ring condensate with spin precession. *Physical Review B* **106,** 245309 (2022).

147. Whittaker, C. *et al.* Optical analogue of Dresselhaus spin–orbit interaction in photonic graphene. *Nature Photonics* **15,** 193–196 (2021).

148. Marti, M., Aichmayr, G., Vina, L. & André, R. Detuning dependence of polariton spin dynamics. *Semiconductor science and technology* **19,** S365 (2004).

149. Amo, A. *et al.* Angular switching of the linear polarization of the emission in InGaAs microcavities. *physica status solidi (c)* **2,** 3868–3871 (2005).

150. Terças, H., Flayac, H., Solnyshkov, D. & Malpuech, G. Non-Abelian gauge fields in photonic cavities and photonic superfluids. *Physical review letters* **112,** 066402 (2014).

151. Flayac, H., Shelykh, I., Solnyshkov, D. & Malpuech, G. Topological stability of the half-vortices in spinor exciton-polariton condensates. *Physical Review B* **81,** 045318 (2010).

152. Sutherland, B. Simple system with quasiperiodic dynamics: a spin in a magnetic field. *Physical review letters* **57,** 770 (1986).

153. Zong, Y. *et al.* Observation of localized flat-band states in Kagome photonic lattices. *Optics Express* **24,** 8877–8885 (2016).

154. Weeks, C. & Franz, M. Topological insulators on the Lieb and perovskite lattices. *Physical Review B* **82,** 085310 (2010).

155. Goldman, N., Urban, D. & Bercioux, D. Topological phases for fermionic cold atoms on the Lieb lattice. *Physical Review A* **83,** 063601 (2011).

156. Dauphin, A., Müller, M. & Martin-Delgado, M. A. Quantum simulation of a topological Mott insulator with Rydberg atoms in a Lieb lattice. *Physical Review A* **93,** 043611 (2016).

157. Wang, R., Qiao, Q., Wang, B., Ding, X.-H. & Zhang, Y.-F. The topological quantum phase transitions in Lieb lattice driven by the Rashba SOC and exchange field. *The European Physical Journal B* **89,** 1–6 (2016).

158. Goblot, V. *et al.* Nonlinear polariton fluids in a flatband reveal discrete gap solitons. *Physical Review Letters* **123,** 113901 (2019).

159. López-González, D. & Molina, M. I. Linear and nonlinear compact modes in quasi-one-dimensional flatband systems. *Physical Review A* **93,** 043847 (2016).

160. Gligorić, G., Maluckov, A., Hadžievski, L., Flach, S. & Malomed, B. A. Nonlinear localized flat-band modes with spin-orbit coupling. *Physical Review B* **94,** 144302 (2016).

161. Whittaker, C. *et al.* Exciton Polaritons in a Two-Dimensional Lieb Lattice with Spin-Orbit Coupling. *arXiv preprint arXiv:1705.03006* (2017).

162. Sutherland, B. Localization of electronic wave functions due to local topology. *Physical Review B* **34,** 5208 (1986).

163. Sun, M., Savenko, I., Flach, S. & Rubo, Y. Excitation of localized condensates in the flat band of the exciton-polariton Lieb lattice. *Physical Review B* **98,** 161204 (2018).

164. Sedov, E., Sedova, I., Arakelian, S. & Kavokin, A. Magnetic control over the zitterbewegung of exciton–polaritons. *New Journal of Physics* **22,** 083059 (2020).